ISBN 978-82-326-2982-4 (printed version)
ISBN 978-82-326-2983-1 (electronic version)
ISSN 1503-8181

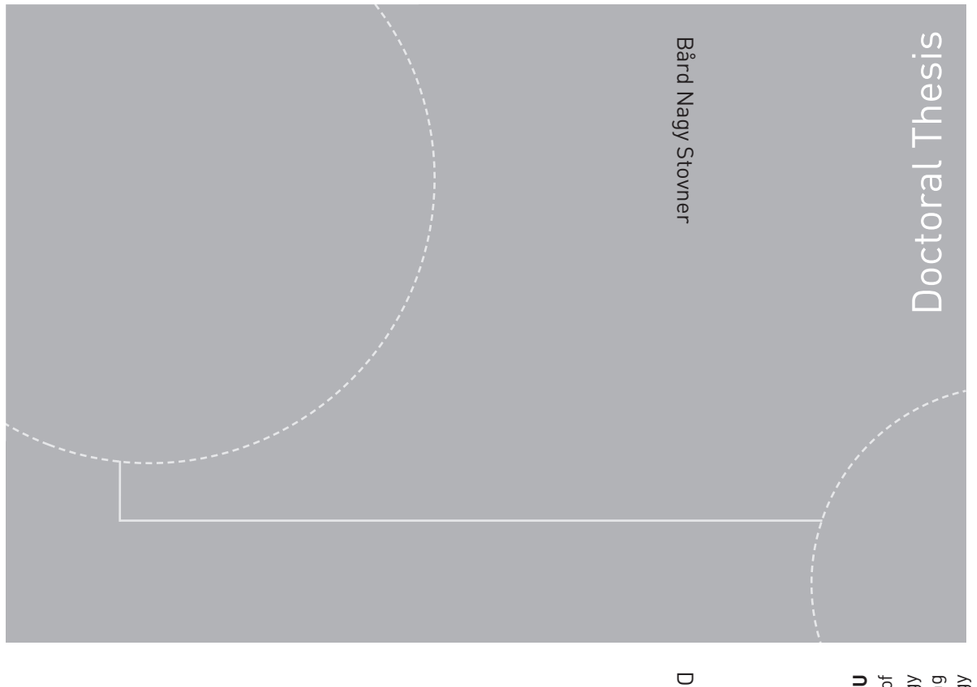

Doctoral theses at NTNU, 2018:96

Bård Nagy Stovner

Aided Inertial Navigation of Underwater Vehicles

NTNU
Norwegian University of
Science and Technology

Doctoral theses at NTNU, 2018:96

NTNU

NTNU
Norwegian University of
Science and Technology
Faculty of Engineering
Department of MarineTechnology

NTNU
Norwegian University of
Science and Technology

Bård Nagy Stovner

Aided Inertial Navigation of Underwater Vehicles

Thesis for the degree of Philosophiae Doctor

Trondheim, March 2018

Norwegian University of Science and Technology
Faculty of Engineering
Department of MarineTechnology

NTNU
Norwegian University of
Science and Technology

NTNU
Norwegian University of Science and Technology

Thesis for the degree of Philosophiae Doctor

Faculty of Engineering
Department of MarineTechnology

ISBN 978-82-326-2982-4 (printed version)
ISBN 978-82-326-2983-1 (electronic version)
ISSN 1503-8181

Doctoral theses at NTNU, 2018:96

Printed by Skipnes Kommunikasjon as

Summary

This thesis is motivated by cost reduction in subsea inspection, maintenance, and repair operations, which requires autonomy and automatic functionality in order to save time and money. Autonomy and automatic functions means taking some aspects of the intervention out of the hands of the human operator, and letting the underwater vehicle make some decisions and perform some actions independently. A prerequisite for the underwater vehicle making a decision and performing an action independently is reliable information about the current *state* of the vehicle, i.e. its position and attitude. *This thesis focuses on reliable and high performance estimation of position and attitude of an underwater vehicle using measurements from inertial measurement units and hydroacoustic sensor networks*. The high performance is ensured by using linearized Kalman filters, an industry standard for that purpose. The reliability is ensured by mathematical proofs of the guaranteed convergence of the estimates to the true value regardless of how erroneous the initial estimate is.

The main part of this thesis presents four estimation concepts, for some of which multiple estimators are developed.

The first is an attitude estimator based on inertial measurement unit and magnetometer measurements. This estimation problem has attracted significant attention in last 50 years, and a multitude of solutions has been proposed. The estimator developed in this thesis is the first Kalman filter based solution with a minimal state error representation and proven global exponential stability. The proposed estimator is compared with existing solutions both in simulations and using experimental data.

The second is position estimation based on inertial measurement unit, hydroacoustic long baseline, and pressure sensor measurements. Hydroacoustic range measurements are found by multiplying the travel time of a signal with the wave speed,

i.e. speed of sound in water. Since the wave speed vary with the water conditions and therefore is not accurately known, the proposed estimators estimate it as well.

The third estimation concept is position estimation based on measurements from an inertial measurement unit, a pressure sensor, and a hydroacoustic sensor network called *inverted short baseline*. The inverted short baseline network consist of multiple hydroacoustic sensors on the vehicle, and it is shown that only one hydroacoustic *transponder* is then needed on the sea floor. This lowers the requirement for external infrastructure, which in turn lowers deployment and maintenance costs. Several estimators are developed and analyzed, and a comparison study using both simulated and experimental data is conducted.

The fourth estimation concept uses the inverted short baseline network described above for both position and attitude estimation. The motivating scenario is that the magnetometer measurements become corrupted by the magnetic fields produced e.g. by the vehicle's motors or a subsea facility. It is shown that the inverted short baseline network along with two transponders on the sea floor can replace the need for magnetometer measurements, thereby providing redundancy.

All of the solutions to the above estimation concepts attain global exponential stability through a mathematical stability analysis and are based on the linearized Kalman filter ensuring high performance.

Preface

This thesis is submitted in partial fulfillment of the requirements for the degree of philosophiae doctor (PhD) at Norwegian University of Science and Technology (NTNU). My PhD project was affiliated with Centre for Autonomous Marine Operations and Systems (NTNU-AMOS), Department of Marine Technology, NTNU, under supervision by professors Ingrid Schjølberg and Thor Inge Fossen. It was part of the project Next Generation Inspection, Maintenance, and Repair (NextGenIMR), funded by the Norwegian Research Council, Statoil Petroleum AS, and TechnipFMC with Sintef as research partner. The PhD work was conducted from August 2014 to December 2017.

Acknowledgements

I would like to thank NextGenIMR for financing and supporting my work, and inspiring my research through our meetings. Moreover, I would like to thank Ingrid and Thor Inge for employing me, and for the interesting discussions that have challenged me to view my problems differently. The trust and autonomy you have given me have made me a more independent and a better researcher. I feel privileged to have had the opportunity to work under your supervision.

Tor Arne Johansen had conveniently developed the three-stage filter and the exogenous Kalman filter just when I was in need of it. You introduced me to them, and they became the bread and butter of my PhD. Furthermore, you have put tremendous effort into my PhD and co-authored all of my papers. I am incredibly grateful for all of your efforts.

Eirik Henriksen and Jeevith Hegde have pursued PhDs alongside me in the NextGenIMR project. Thank you for the interesting discussions and late nights in the lab in preparation for project meetings and demonstrations. Thanks are owed to Erlend Jørgensen for the both frustrating and rewarding work in developing the hydroa-

coustic system, quarreling with the Qualisys camera system, getting remotely operated vehicles (ROVs) up and running, and developing the simulator framework. I would like to thank Mikkel Cornelius Nielsen for invaluable discussions that have helped me solve my problems. I would like to thank all my colleagues who have made my work days inspiring and coffee breaks fun.

I would like to thank my family, both my original and in-law, for your continued support. Last, but not least, I would like to thank my beautiful wife and the love and coauthor of my life, Mette, for always supporting and inspiring me. You have given me a daughter, you make our house a home, you are a perfect mother and wife, and still, you are the one bringing in the big bucks. You never cease to amaze me.

Contents

List of Tables

List of Figures

List of Abbreviations

3SF three-stage filter

AEKF additive extended Kalman filter

AIN aided inertial navigation

NTNU-AMOS Centre for Autonomous Marine Operations and Systems

ARS angular rate sensor

AT algebraic transformation

AUV autonomous underwater vehicle

DOF degree-of-freedom

DVL Doppler velocity log

ECI earth-centered inertial

EKF extended Kalman filter

FOG fiber optic gyroscope

GAS global asymptotic stability

GEKF geometric extended Kalman filter

GES global exponential stability

GIB GPS intelligent buoy

GNC guidance, navigation, and control

GNSS global navigation satellite system

GPS global positioning system

IEKF invariant extended Kalman filter

IMR inspection, maintenance, and repair

IMU inertial measurement unit

INS inertial navigation system

iSBL inverted short baseline

iUSBL inverted ultrashort baseline

KF Kalman filter

LBL long baseline

LES locally exponentially stable

LTV linear time-varying

MAE mean absolute error

MCLab Marine Cybernetics Laboratory

MEKF multiplicative extended Kalman filter

MEMS micro-electromechanical system

MRP modified Rodrigues parameter

MXKF multiplicative exogenous Kalman filter

NED north-east-down

NextGenIMR Next Generation Inspection, Maintenance, and Repair

NLO nonlinear observer

NTNU Norwegian University of Science and Technology

PE persistency of exitation

PF particle filter

PVA position, velocity, and attitude

QUEST quaternion estimator

RLG ring laser gyroscope

ROV remotely operated vehicle

SBL short baseline

SKF Schmidt-Kalman filter

TDOA time-difference-of-arrival

TOA time-of-arrival

TRIAD tri-axial attitude determination

UCC uniformly completely controllable

UCO uniformly completely observable

UGES uniform global exponential stability

UKF unscented Kalman filter

USBL ultrashort baseline

UV underwater vehicle

XKF exogeonus Kalman filter

Notations

t	Time
$0_{n\times m}$	An $\mathbb{R}^{n\times m}$ matrix of zeroes
I_n	An $\mathbb{R}^{n\times n}$ matrix of zeroes with ones on the diagonal
l_n	An $\mathbb{R}^{n\times 1}$ vector of ones
$\{a, b, c\}$	A set containing exactly the elements a, b, and c
$(1, n)$	A set containing all whole numbers from 1 to n, i.e. $\{1, ..., n\}$
$\{b\}$	body-fixed coordinate frame
$\{e\}$	earth-centered inertial (ECI) coordinate frame
$\{n\}$	north-east-down (NED) coordinate frame
R_b^n	Rotation matrix representing the rotation from $\{b\}$ to $\{n\}$
Φ_b^n	Euler angles representing the rotation from $\{b\}$ to $\{n\}$
q_b^n	Unit quaternion representing the rotation from $\{b\}$ to $\{n\}$
p_{bc}^a	Position of point c relative to point b decomposed in coordinate frame $\{a\}$
v_{bc}^a	Velocity of point c relative to point b decomposed in coordinate frame $\{a\}$
a_{bc}^a	Acceleration of point c relative to point b decomposed in coordinate frame $\{a\}$
$\mathcal{Q}$	Process noise covariance matrix
$\mathcal{R}$	Measurement noise covariance matrix

Part I

Introduction and Preliminaries

Chapter 1

Introduction

This thesis considers aided inertial navigation (AIN) of underwater vehicles. Methods for estimating the position, velocity, and attitude (PVA) of underwater vehicles using hydroacoustic sensor networks and onboard sensors are developed. It includes the development and implementation of a hydroacoustic system and a range of estimators. A special emphasis is placed on the mathematical analysis of the estimators, which is also the main contribution of this thesis work.

1.1 Motivation

This work is part of the project Next Generation Inspection, Maintenance, and Repair (NextGenIMR) (grant no. 234108) with the goal of planning and developing autonomous and automatic functions and systems for subsea oil and gas facilities in order to make inspection, maintenance, and repair (IMR) operations cheaper, safer, and faster.

Current IMR operations on subsea facilities require the deployment of a support vessel to the site, submerging a remotely operated vehicle (ROV) to the facility, and manual control of the ROV and manipulator arm by a small team of operators. This process is time-consuming and expensive in itself. Schjølberg and Utne [1] reported a daily cost of a support vessel at 100 000–300 000 USD, depending on the vessel size. Furthermore, the cost increases dramatically if the cause or means of intervention halts production. In Schjølberg et al. [2], it was uncovered that a large volume of the IMR operations can be partly or fully automated, as they are simple and involve little physical intervention. These tasks include, but are not

limited to:

- Cleaning
- Inspection
- Turning valves
- Hot-stab

These functions can be performed by autonomous underwater vehicles (AUVs) and semi-autonomous ROVs and require only low-risk intervention. Therefore, they are realistically applicable to existing facilities in a short time-frame. Also, the implementation and use of AUVs and ROVs for these functions serve as a stepping stone for more complex intervention tasks in the future.

1.2 The Guidance, Navigation, and Control System

If underwater vehicles (UVs) are to operate autonomously or perform automatic functions, then a guidance, navigation, and control (GNC) system is required. The GNC system, a simplified view of which is given in Figure 1.1, is what takes the higher-level plans and measurements of the UV's state and produces control actions to carry out the plans. Below, each of the GNC subsystems is explained.

Navigation: The navigation system is responsible for estimating the vehicle's state from the available measurements. The state often consists of PVA, along with relevant systematic sensory and environmental disturbances. The systematic disturbances may be e.g. biases, scale factors, or misalignments on inertial and magnetic sensors, water current velocity, or the wave speed, i.e. the propagation speed of sound in water. It is emphasized that navigation in the control engineering sense has nothing to do with steering of the vehicle, which is the common understanding of the word.

Guidance: With the knowledge of where the vehicle is and where it is supposed to go, it is the guidance system's task to continuously produce the desired translational and rotational motions that would lead the vehicle there in an optimal way. The optimality may be with respect to fuel consumption, time, safety etc. This desired behavior is then used as a reference for the control system.

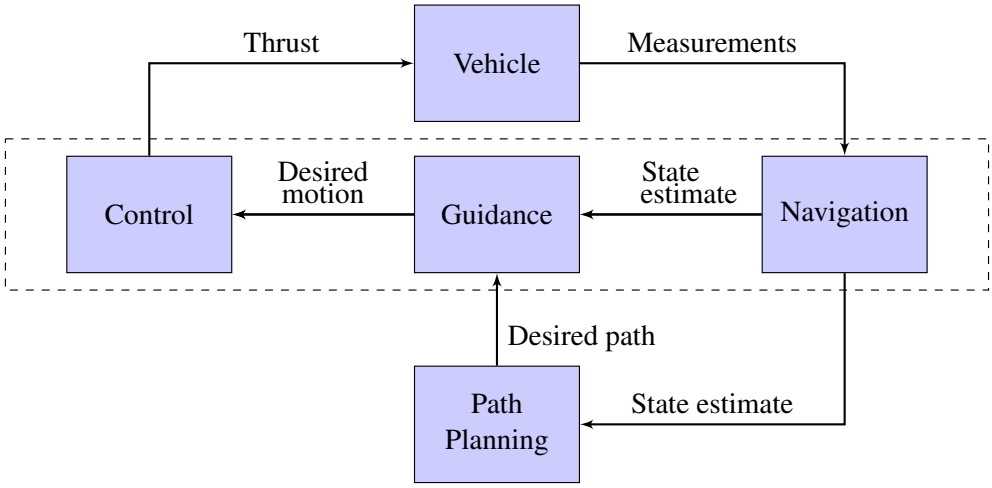

Figure 1.1: The GNC system.

Control: The control system converts the desired translational and rotational motions into desired forces and angular momentums. From this, the internal *control allocation* calculates motor thrusts that, when exerted by the motors, produce the desired behavior.

The GNC system described above works under certain assumptions. Firstly, the state must be *observable* from the measurements, meaning that the measurements must describe the state in a sufficiently rich way such that the state can be estimated. Secondly, the guidance and control systems often require a dynamic model of the vehicle, i.e. a model that predicts the behavior of the vehicle given an input. This model must be sufficiently accurate, or else the vehicle will not follow the desired trajectory. Lastly, the guidance system requires input from higher level *path planning*. The path planning can range from simple way-points provided by a human operator to a fully autonomous decision process involving safety assessments and path refinements.

We understand that the navigation system is the foundation for almost all automatic and autonomous functions conducted by a vehicle, and consequently, its performance is vital to the performance of the GNC system as a whole. The navigation system consists of one or a series of *estimators*. The performance of an estimator is often assessed by two qualities: its stability properties and how it is influenced by sensor noise. The navigation system is additionally assessed by its *robustness*,

i.e. its ability to handle sensor malfunctions like corrupted measurements and measurement drop-outs. For this, sensor redundancy and outlier rejection are needed. This thesis primarily concentrates on the development and performance of estimators, and not on the broader topic of robustness in the navigation system.

1.3 Aided Inertial Navigation

An estimator can either be developed in continuous or discrete time. For simplicity of analysis, the estimators in this thesis are developed in continuous time. All implementations, however, must be in discrete time, so the estimators' continuous time update equation must be discretized before implementation on a computer, a thorough account of which is given in Bryne et al. [3].

A discrete estimator commonly involves two steps: a prediction step and a correction step. In the prediction step, the state estimate is propagated in time by integrating the vehicle's kinematic model by using measurements from inertial sensors like the accelerometer and angular rate sensor (ARS).[1] Due to noisy and biased measurements, the prediction step causes the state estimate to drift away from the true state over time. Therefore, a correction step is needed, in which absolute measurements of the state eliminate this drifting error. Estimation based purely on the prediction step is known as *inertial navigation* or *dead reckoning*. When aided by the correction step, the estimation is known as *aided inertial navigation*.

The estimation of a vehicle's state often consists of a rotational motion estimator, estimating the vehicle's attitude, and a translational motion estimator, estimating the vehicle's position and velocity. These may depend on each other's estimates, and collaborate in either a cascade or feedback structure, seen in Figure 1.2.

1.3.1 Observers and Filters

Estimators can be categorized in two groups: *filters*, which take the stochastic nature of model and measurement errors into account and estimate the state's covariance, and *observers*, which do not. Observers only holds the state estimate. Filters are divided into two groups, i.e. *direct* and *indirect* filters. Simply put, direct filters estimate the desired state while indirect filters estimate the error between the true and estimated state. The estimated error is then used to correct a state estimate. Understandably, they are also called *full state* and *error state* filters,

[1] Alternatively, the vehicle's dynamic model can be integrated using the input to the thrusters. This would require an accurate model of the vehicle's response to thruster inputs.

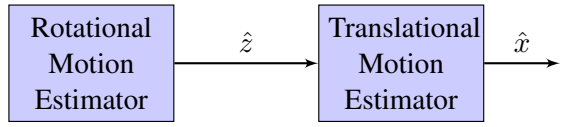

(a) Cascade structure

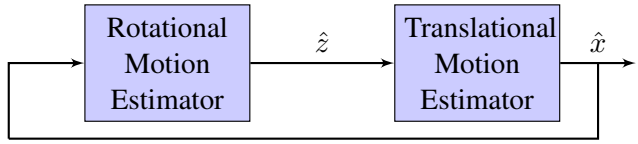

(b) Feedback structure

Figure 1.2: The cascade and feedback estimator structures where z denotes the rotational state and x denotes the translational state.

respectively. As discussed by Roumeliotis, Sukhatme, and Bekey [4], there are several advantages of using indirect filtering over direct filtering when it comes to computational complexity and robustness. In this thesis, however, direct filters are mostly used.

Consider the linear system

$$\dot{x}(t) = Ax(t) + Bu(t) + G\epsilon_x(t) \tag{1.1a}$$
$$y(t) = Cx(t) + \epsilon_y(t), \tag{1.1b}$$

where

- $x(t)$, $\dot{x}(t)$: state vector and its time derivative, respectively
- $u(t)$: input vector
- $y(t)$: measurement vector
- A: system matrix
- B: input matrix
- G: system noise matrix
- C: measurement matrix
- $\epsilon_x(t)$, $\epsilon_y(t)$: unbiased and white system and measurement noises, respectively

- $\mathcal{Q} = \mathrm{E}(\epsilon_x(t)\epsilon_x(t)^\top)$: system covariance matrix
- $\mathcal{R} = \mathrm{E}(\epsilon_y(t)\epsilon_y(t)^\top)$: measurement covariance matrix.

All vectors are assumed to be column vectors, of which the superscript $^\top$ denotes the transpose. Here, (1.1a) is called the *dynamic model* and (1.1b) is called the *measurement model* of system (1.1).

An example of a filter and an observer is given by the Kalman filter (KF) and Luenberger observer, respectively. In both, the correction of the state estimate is proportional to the *measurement error* $\tilde{y}(t) \triangleq y(t) - \hat{y}(t)$, where $\hat{y}(t) \triangleq C\hat{x}(t)$ is the estimated measurement. The Luenberger observer is given by

$$\dot{\hat{x}}_{lo}(t) = A\hat{x}_{lo}(t) + Bu(t) + K_{lo}\tilde{y}(t) \tag{1.2}$$

and the KF is given by

$$\dot{\hat{x}}_{kf}(t) = A\hat{x}_{kf}(t) + Bu(t) + K_{kf}(t)\tilde{y}(t) \tag{1.3a}$$
$$K_{kf}(t) = P(t)C^\top\mathcal{R}^{-1} \tag{1.3b}$$
$$\dot{P}(t) = AP(t) + P(t)A^\top + G\mathcal{Q}G^\top - P(t)C^\top\mathcal{R}^{-1}CP(t), \tag{1.3c}$$

where $P(t)$ is an estimate of the state covariance, and an initial estimate $P(t_0) = P_0$ must be given to the KF. K_{lo} and $K_{kf}(t)$ are called the *gain matrices* and represent the difference between these two estimators. K_{lo} is a tuning parameter, whereas K_{kf} is found by (1.3b). However, tuning is required when setting the $\mathcal{Q}$, $\mathcal{R}$, and P_0 matrices. Both estimators require initial state estimates $\hat{x}_{lo}(t_0)$ and $\hat{x}_{kf}(t_0)$. Kalman and Bucy [5] proved that the estimate $\hat{x}_{kf}(t)$ is the *minimum variance linear unbiased estimate*, meaning it is the optimal unbiased estimate w.r.t. variance of the estimation error for a linear system with white noise characteristics and a completely known model. Consequently, the Luenberger observer is *not* an optimal estimator in the general case.

1.3.2 Stability Analysis

Let $x(t)$ and $\hat{x}(t)$ be a general state and an estimate of it, respectively. Furthermore, the dynamics and measurements of $x(t)$ are given by the possibly nonlinear and time-varying functions f and h, respectively, i.e.

$$\dot{x}(t) = f(x(t), u(t), t) \tag{1.4a}$$
$$y(t) = h(x(t), t). \tag{1.4b}$$

In order to estimate this system, an estimator is defined

$$\dot{\hat{x}}(t) \triangleq \hat{f}(\hat{x}(t), u(t), t). \tag{1.5}$$

Define the estimation error $\tilde{x}(t) \triangleq x(t) - \hat{x}(t)$. Now, the *error dynamics* can be found as

$$\dot{\tilde{x}}(t) = \tilde{f}(\tilde{x}(t), t) = f(x(t), t) - \hat{f}(\hat{x}(t), t). \tag{1.6}$$

The goal of estimation is to find $\hat{f}(\hat{x}(t), t)$ that makes $\|\tilde{x}(t)\|_2 \to 0$ as $t \to \infty$, which is equivalent to $\hat{x}(t) \to x(t)$ as $t \to \infty$. Here $\|\tilde{x}(t)\|_k = (\tilde{x}_1(t)^k + \cdots + \tilde{x}_N(t)^k)^{1/k}$ is the norm operator, $\tilde{x}(t) = [\tilde{x}_1(t), \ldots, \tilde{x}_N(t)]^\top$, and $N = \dim(x)$. *Stability analysis* is the mathematical analysis of the behavior of $\tilde{x}(t)$ as time passes. We say that the *equilibrium point* $\tilde{x} = 0$ of system (1.6) is *stable* if for any initial estimation error $\|\tilde{x}(0)\|_2 < \delta$, the estimation error will be bounded $\|\tilde{x}(t)\|_2 < \epsilon$ for all time t, [6].

Stability is clearly not enough, as it does not guarantee convergence of the state estimate, i.e. $\hat{x} \to x$. Therefore, we investigate the following stability properties from Khalil [6]:

- *Rate of convergence*: With which speed can it be guaranteed that $\tilde{x} \to 0$? If it merely can be guaranteed that $\|\tilde{x}(t)\|_2 \to 0$ as $t \to \infty$ for all $\|\tilde{x}(t_0)\|_2 < c$, the equilibrium point $\tilde{x} = 0$ of (1.6) is said to be *asymptotically stable*. A stronger rate of convergence is when $\|\tilde{x}(t)\|_2$ can be bounded from above by an exponentially decaying function, i.e.

  $$\|\tilde{x}(t)\|_2 \leq k\|\tilde{x}(t_0)\|_2 e^{-\lambda(t-t_0)} \text{ for all } \|\tilde{x}(t_0)\|_2 < c, \tag{1.7}$$

  where k, λ, and c are positive constants. Then, the equilibrium point is *exponentially stable*.

- *Region of attraction*: For which initial error $\|\tilde{x}(t_0)\|_2$ can convergence of $\|\tilde{x}(t)\|_2 \to 0$ be guaranteed? If convergence only can be guaranteed for initial errors $\|\tilde{x}(t_0)\|_2 < c$, where c is a positive constant, the region of attraction is said to be *local*. However, for systems where convergence is guaranteed for any initial error $\|\tilde{x}(t_0)\|_2$, the region of attraction is *global*.

- *Uniformity*: For a time-varying system, the equilibrium point $\tilde{x} = 0$ is *uniformly stable* if it is stable independently of t_0. In order to have uniform asymptotic and exponential stability, there are additional requirements, for which it is referred to Definition 4.4 in Khalil [6].

From this, eight different stability properties can be constructed. The naming convention used in this thesis is $U/\cdot + L/G + A/E + S$, e.g. global exponential stability (GES) or uniform global exponential stability (UGES).

Example 1.3.1 (Estimation of a linear system)**.** *Consider the 1D problem of estimating the position of a cart on a straight rail. A ranging device installed both on the cart and the rail provides a distance measurement between them. Assume the rail-mounted device can determine on which side of it the cart is, which allows it to find a position measurement of the cart, denoted $y(t)$. Also, the acceleration along the rail is measured and used as input $u(t)$. Let x_1 be the position and x_2 be the velocity of the cart relative the ranging device on the rail. This scenario is depicted in Figure 1.3. The system can be written as*

$$\begin{aligned}\dot{x}_1(t) &= x_2(t)\\ \dot{x}_2(t) &= u(t) + \epsilon_x\\ y(t) &= x_1(t) + \epsilon_y,\end{aligned}$$

where ϵ_x and ϵ_y are unbiased, white noises with variance σ_x^2 and σ_y^2, respectively. The system can be written in compact form (1.1) *with $x = [x_1, x_2]^\top$ and*

$$A = \begin{bmatrix}0 & 1\\ 0 & 0\end{bmatrix}, B = \begin{bmatrix}0\\ 1\end{bmatrix}, G = \begin{bmatrix}0\\ 1\end{bmatrix}, C = \begin{bmatrix}1 & 0\end{bmatrix},$$

for which we use the Luenberger observer (1.2) *and KF* (1.3)*. The respective error dynamics in the noise-less case become*

$$\dot{\tilde{x}}_{lo} = (A - K_{lo}C)\tilde{x}_{lo} \tag{1.8}$$

$$\dot{\tilde{x}}_{kf} = (A - K_{kf}(t)C)\tilde{x}_{kf}. \tag{1.9}$$

The stability analysis of the KF error dynamics follows by employing a well-known result: Since the observability and controllability matrices

$$\mathcal{O} = \begin{bmatrix}C\\ CA\end{bmatrix} = \begin{bmatrix}1 & 0\\ 0 & 1\end{bmatrix}, \mathcal{C} = \begin{bmatrix}G & GA\end{bmatrix} = \begin{bmatrix}0 & 1\\ 1 & 0\end{bmatrix}$$

have full rank, the system (A, C) is observable and (A, G) is controllable, which Kalman [7] proved to yield GES of the equilibrium point $\tilde{x}_{kf} = 0$ of (1.9)*.*

The design choice $K_{lo} = [2, 1]^\top$ yields

$$D \triangleq A - K_{lo}C = \begin{bmatrix}-2 & 1\\ -1 & 0\end{bmatrix},$$

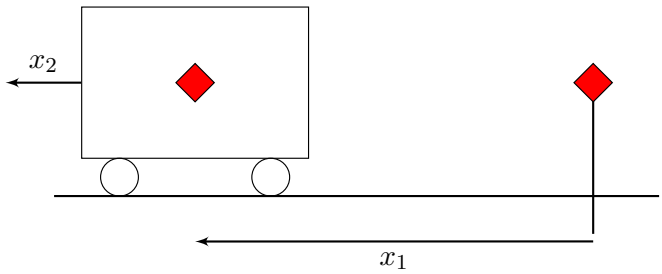

Figure 1.3: Example 1 scenario with a cart on a rail and range devices in red.

which has only negative eigenvalues, $\lambda_1 = -1$ *and* $\lambda_2 = -1$*, i.e. it is* Hurwitz*. Theorem 4.1 of Khalil [6] proves that for any Hurwitz matrix* D *and positive definite matrix* Q*, there exist a positive definite matrix* P *such that* $PD + D^\top P = -Q$*. Now, we can define the positive definite* Lyapunov function $V(t) = \tilde{x}_{lo}(t)^\top P \tilde{x}_{lo}(t)$ *and find its derivative*

$$\begin{aligned}\dot{V}(t) &= \tilde{x}_{lo}(t)^\top PD\tilde{x}_{lo}(t) + \tilde{x}_{lo}(t)^\top D^\top P\tilde{x}_{lo}(t) \\ &= \tilde{x}_{lo}(t)^\top (PD + D^\top P)\tilde{x}_{lo}(t) = -\tilde{x}_{lo}(t)^\top Q\tilde{x}_{lo}(t).\end{aligned}$$

Let $p_{\min}, p_{\max} > 0$ *denote the smallest and largest eigenvalues of* P*, respectively, and* $q_{\min} > 0$ *the smallest eigenvalue of* Q*. Now, we have the properties*

$$p_{\min}\|\tilde{x}_{lo}(t)\|_2^2 \leq V(t) \leq p_{\max}\|\tilde{x}_{lo}(t)\|_2^2 \tag{1.10a}$$

$$\dot{V}(t) \leq -q_{\min}\|\tilde{x}_{lo}(t)\|_2^2 < 0 \;\forall\; \tilde{x}_{lo} \neq 0. \tag{1.10b}$$

From (1.10b)*, we see that* $V(t)$*, and consequently* $\tilde{x}_{lo}(t)$*, can only decrease until* $\tilde{x}_{lo} = 0$*, regardless of the initial estimation error. This is global asymptotic stability (GAS). Furthermore, since we can find*

$$\|\tilde{x}_{lo}(t)\|_2^2 \leq \frac{1}{p_{\min}}V(t),\ \frac{dV(t)}{dt} \leq -\frac{q_{\min}}{p_{\min}}V(t) \Rightarrow \frac{dV(t)}{V(t)} \leq -\frac{q_{\min}}{p_{\min}}dt$$
$$V(t) \leq V(t_0)e^{-\frac{q_{\min}}{p_{\min}}(t-t_0)} \Rightarrow \|\tilde{x}_{lo}(t)\|_2^2 \leq \|\tilde{x}_{lo}(t_0)\|_2^2 e^{-\frac{q_{\min}}{p_{\min}}(t-t_0)},$$

which we from (1.7) *see that clearly qualifies as GES.*

For nonlinear systems on the general form (1.4), developing estimators with strong stability properties and high performance is generally harder. The workhorse for estimation of nonlinear systems is the extended Kalman filter (EKF), which can

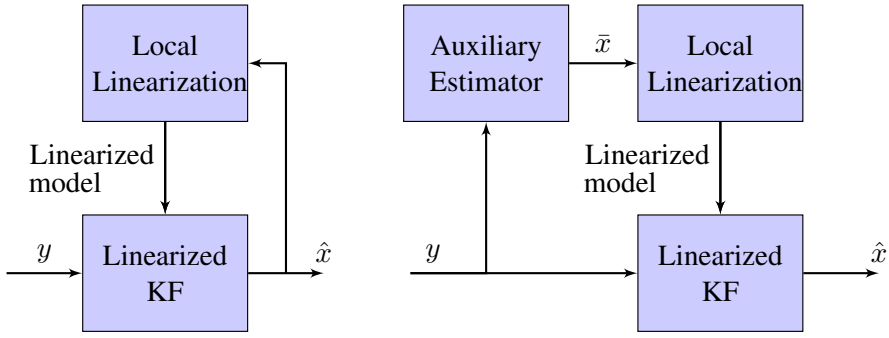

(a) EKF **(b)** XKF

Figure 1.4: The general EKF and XKF structures. $\bar{x}$ denotes the auxiliary estimator's estimate.

be applied to all differentiable systems. In the EKF, a linear approximation of the nonlinear system is achieved by linearizing it about the EKF's estimate. Then, a KF is applied to the linearized system. This makes the EKF a versatile estimator, which has found many applications in a wide range of fields. However, the EKF does not come with global stability properties in the general case, which makes it sensitive to large initial errors and corrupted measurements. The lack of global stability is due to the feedback of the EKF's estimate to the linearization; an incorrect estimate leads to an erroneous linearized model, which in turn might make the correction step increase the estimation error rather than decrease it. A recent development in nonlinear estimation is the exogeonus Kalman filter (XKF) by Johansen and Fossen [8]. The XKF is similar to the EKF, but relies on an auxiliary estimator to provide the linearization point. This difference is illustrated in Figure 1.4. Given that the linearized model is observable and controllable, and the covariance matrices P_0, $\mathcal{Q}$, and $\mathcal{R}$ are chosen positive definite, the XKF inherits the stability of the auxiliary estimator. This is an important result, because it enables simple design of high performance estimators with strong stability results.

Contrary to the linear KF, the linearized KF of the XKF and EKF cannot guarantee optimality w.r.t. variance of the estimation error since the linearization introduces an error. However, when the estimate has converged, the linear model is assumed to be a good approximation of the nonlinear one and the performance said to be *near-optimal*. Therefore, the EKF is assumed to be a near-optimal estimator of a nonlinear system. Since the XKF relies on a suboptimal linearization point, one could expect it to perform worse than the EKF. From experience, however, this has

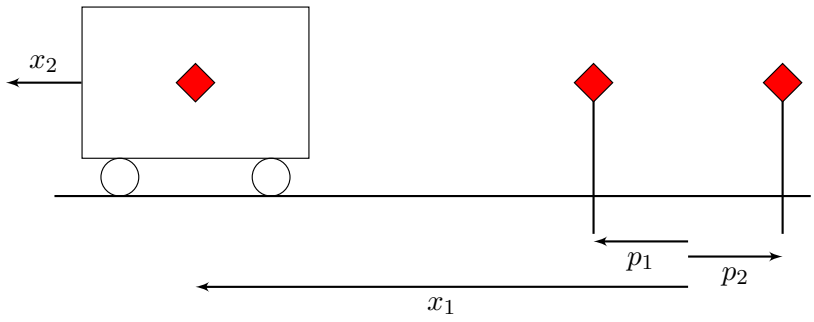

Figure 1.5: Example 2 scenario with two rail-mounted range deviced.

been seen to not hold true, i.e. they yield similar performances, even for an XKF with a considerably worse linearization point.

Example 1.3.2 (Estimation of a nonlinear system)**.** *Consider Example 1.3.1. Instead of a position measurement $y(t) = x_1(t) + \epsilon_y(t)$, two (non-directional) range measurements are available*

$$y_i(t) = h_i(x(t), t) \triangleq \|x_1(t) - p_i(t)\|_2 + \epsilon_{y,i}(t), \ i \in \{1, 2\},$$

where p_i is the position of ranging device i on the rail and $\epsilon_{y,i}(t)$ is an unbiased white noise with variance $\sigma^2_{y,i}$. This set-up is illustrated in Figure 1.5.

Denote by $\hat{x}_{ekf}$ and $\hat{x}_{xkf}$ the EKF and XKF estimates, respectively, and let $\check{x} = [\check{x}_1, \check{x}_2]^\top$ denote the linearization point. Linearization is now done by the Taylor expansion of $h = [h_1, h_2]^\top$

$$h(x(t), t) = h(\check{x}(t), t) + H(\check{x}(t), t)(x(t) - \check{x}(t)) + \varphi(x_1(t) - \check{x}_1(t), t), \quad (1.11)$$

where φ is the sum of higher order terms and represents the linearization error*. Furthermore, $\varphi(0, t) = 0$, and H is the linearized measurement matrix*

$$H(\check{x}(t), t) = \left.\frac{dh(x(t), t)}{dx}\right|_{x=\check{x}} = \begin{bmatrix} \frac{\check{x}_1 - p_1}{\|\check{x}_1 - p_1\|_2} & 0 \\ \frac{\check{x}_1 - p_2}{\|\check{x}_1 - p_2\|_2} & 0 \end{bmatrix}.$$

An EKF is implemented by inserting $C = H(\hat{x}_{ekf}(t), t)$, $\hat{y}(t) = h(\hat{x}_{ekf}(t), t)$, and

$$\mathcal{R} = \mathcal{R}_{ekf} = \begin{bmatrix} \sigma^2_{y,1} & 0 \\ 0 & \sigma^2_{y,2} \end{bmatrix}$$

into (1.3)*. Assuming the linearized system* $(A, H(\hat{x}_{ekf}(t), t))$ *is observable, the equilibrium point* $x - \hat{x}_{ekf} = 0$ *is locally exponentially stable (LES), see Theorem 4.13 of Khalil [6].*

For the XKF, an auxiliary estimator is required. By calculating

$$\begin{aligned} Y(t) \triangleq y_1(t)^2 - y_2(t)^2 - p_1^2 + p_2^2 = &- 2(p_1 - p_2)x_1(t) + 2(x_1(t) - p_1)\epsilon_{y,1}(t) \\ &- 2(x_1(t) - p_2)\epsilon_{y,2}(t), \end{aligned}$$

we have achieved a linear model. We denote by $\bar{x}_{xkf}(t)$ *the auxiliary estimator's state, and implement the KF* (1.3) *using* $C = \bar{C}_{xkf} \triangleq [-2(p_1 - p_2), 0]$, $\tilde{y} = Y - \bar{C}\bar{x}_{xkf}$*, and measurement variance* $\bar{R}_{xkf}(t) = 4(x_1 - p_1)^2\sigma_1^2 + 4(x_1 - p_2)^2\sigma_2^2$*. The stability of the auxiliary estimator is proven to be GES by the KF proof in Example 1.3.1 with the added assumption* $p_1 \neq p_2$*.*

Finally, we develop the XKF by inserting the exogenous state $\bar{x}_{xkf}(t)$ *into the measurement model* (1.11) *and defining the estimated measurement*

$$\hat{y}_{xkf}(t) \triangleq h(\bar{x}_{xkf}(t), t) + H(\bar{x}_{xkf}(t), t)(\hat{x}_{xkf}(t) - \bar{x}_{xkf}(t)).$$

Now, the XKF can be implemented by inserting $C = H(\bar{x}_{xkf}(t), t)$, $\hat{y}(t) = \hat{y}_{xkf}(\bar{x}_{xkf}(t))$*, and* $\mathcal{R} = \mathcal{R}_{xkf} = \mathcal{R}_{ekf}$ *into* (1.3)*.*

Finding the measurement error

$$\tilde{y}_{xkf} \triangleq y - \hat{y}_{xkf} = H(\bar{x}_{xkf}(t), t)(x(t) - \hat{x}_{xkf}(t)) - \varphi(x(t) - \bar{x}_{xkf}(t), t),$$

where $\tilde{x}_{xkf} \triangleq x - \hat{x}_{xkf}$*, yields the error dynamics*

$$\dot{\tilde{x}}_{xkf} = (A - K_{xkf}(t)H(\bar{x}_{xkf}(t), t))\tilde{x}_{xkf} - K_{xkf}(t)\varphi(x(t) - \bar{x}_{xkf}(t), t). \tag{1.12}$$

The intuition behind the proof is that since $\|x - \bar{x}_{xkf}\|_2 \to 0$ *as* $t \to \infty$*, the linearization error* φ *disappears. Then, we are left with the error dynamics* $\dot{\tilde{x}}_{xkf} = (A - K_{xkf}(t)H(\bar{x}_{xkf}(t), t))\tilde{x}_{xkf}$*. As in the linear case in Example 1.3.1, observability of* $(A, H(\bar{x}_{xkf}(t), t))$ *is required. Assuming observability, the equilibrium point* $\tilde{x}_{xkf} = 0$ *of the error dynamics* (1.12) *inherits the stability properties of the auxiliary estimator. The formal proof of this is given in Johansen and Fossen [8].*

The estimators are used in a simulation, the results of which can be seen in Figure 1.6. Here, 100 simulations with the trajectory in Figure 1.6(a), but with different randomly generated noise, were made, and the mean absolute error (MAE) is

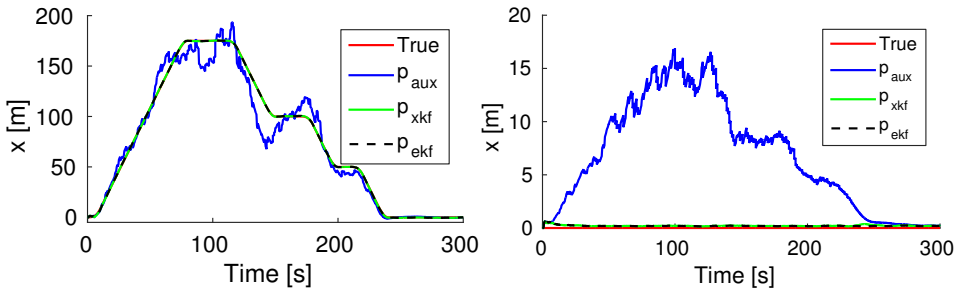

(a) Trajectory

(b) Mean absolute errors.

Figure 1.6: Trajectory and estimates in one of the 100 simulations in 1.6(a). MAE over all 100 simulations in 1.6(b).

Table 1.1: The averaged MAE values for the 100 simulations.

Estimator	Aux.	XKF	EKF
MAE [m]	6.5280	0.2114	0.2067

shown in Figure 1.6(b). The estimators were implemented in discrete time. In the simulations, the following values were used:

$$x(0) = \bar{x}_{xkf}(0) = \hat{x}_{xkf}(0) = \hat{x}_{ekf}(0) = [0, 0]^\top$$
$$\bar{P}_{xkf} = \hat{P}_{xkf} = \hat{P}_{ekf} = \begin{bmatrix} 1 & 0 \\ 0 & 1 \end{bmatrix}$$
$$p_1 = 2m,\ p_2 = -2m,\ \sigma_x = 0.05\frac{m}{s^2},\ \sigma_{y,1} = \sigma_{y,2} = 1m.$$

The measurement rate of the acceleration was $100Hz$ *and the range was* $1Hz$.

This example displays an important quality of the XKF. Even with a poor linearization point from the auxiliary estimator, the performance is close to identical, as seen from Figure 1.6(b) and the MAE values in Table 1.1.

1.4 Sensor Technology

A commonly used sensor for inertial navigation is the inertial measurement unit (IMU), consisting of an ARS and an accelerometer measuring the angular rate and *specific force*. The specific force is the acceleration relative to free-fall, meaning that when the vehicle lies still, the accelerometer measures the gravitational acceleration upwards, i.e. away from Earth's center. Since specific force is measured in

the vehicle's body-fixed frame, while the position and velocity estimates are often expressed in a global frame, the rotation from the body-fixed frame to the global frame is needed. This rotation is called the *attitude* of the vehicle. A Doppler velocity log (DVL) can also be used for inertial navigation. It measures the velocity of the vehicle relative to Earth expressed in the body-fixed frame. Again, the attitude is required for position estimation in the global frame. These examples clearly show the need for an attitude estimate in position estimation and explain why the cascaded structure in Figure 1.2(a) is often used.

The ARS provides the angular rate measurements needed for the prediction step of attitude estimation. It is often assumed to be biased, which introduces the estimation of an ARS bias as well. For the correction step in attitude estimation, *reference vectors* that are known or measured both in the global and in the body-fixed frame are used. The specific force is a commonly used measurement for low-acceleration vehicles on or near Earth, as it measures the gravitational acceleration in the body-fixed frame which also is known in the global frame. Similarly, the magnetometer measures Earth's magnetic field in the body-fixed frame, which is known in the global frame. Understandably, IMUs play a significant role in almost any navigation system. They exist in a wide range of qualities and prices, meaning they are applicable for both low-cost and high performance systems. The ARS technology ranges from the high-end and expensive ring laser gyroscope (RLG) and fiber optic gyroscope (FOG) to low-cost and low-performance micro-electromechanical system (MEMS) technology [9]. The MEMS technology also includes accelerometers and magnetometers.

For underwater position estimation, absolute measurements of the vehicle's position are required. A pressure sensor is a simple sensor that, if calibrated well, reliably and precisely measures the depth of the vehicle. This is not enough, however, as it does not provide information about its horizontal position. For this, hydroacoustic sensor networks have found widespread use. The first hydroacoustic sensor network was the long baseline (LBL), consisting of hydroacoustic *transducers* on the vehicle, often called *transceivers*, and multiple on the sea bed, often called *transponders*. The measurement retrieval strategy is typically that the transceiver sends a signal to the transponders, to which the transponders reply. Detecting the time-of-arrival (TOA) of the responses, the ranges between transceiver and transponders are found. Assuming the geometry of the *baselines*, i.e. the relative position of transponders, are appropriate, 3 range measurements are enough to estimate the position of the vehicle. This set-up is in principle the same for all hydroacoustic networks: One or more transducers in the vehicle's surroundings

provide range measurements to one or more transducers on the vehicle.

What differentiates the hydroacoustic sensor networks is the length of the baselines. Since the LBL transponders are mounted on the sea bed, only practical and geographical considerations limit the baseline lengths. Longer baselines generally yield higher estimation accuracy, but it is not the only factor. As important is the relative positions of the transponders, where increasing diversity yields higher estimation accuracy. This means e.g. that when placing a third transponder on the sea bed, it is better that the three transponders form an equilateral triangle than a line.

Geometrically similar to the LBL is the GPS intelligent buoy (GIB), where buoys positioned by the global positioning system (GPS) carry the transponders. In the short baseline (SBL) network, a small array of transducers are often mounted under a surface vessel, typically from which the UV is employed. Examples of other SBL set-ups also exist [10]. Here, the baselines are limited by the size of the surface vessel. Reducing the baseline lengths further, we find the ultrashort baseline (USBL) network, where the array of transducers are compactly fitted inside an apparatus. As with the SBL, the USBL apparatus is often mounted under a surface vessel in order to measure the UV's position relative the surface vessel. Here, time-difference-of-arrival (TDOA) must be detected with high precision in order to get usable range and bearing measurements. The above configurations rely on an external array of transducers, and consequently, significant external infrastructure. A network that only requires one transponder in the vehicle's surroundings is the inverted ultrashort baseline (iUSBL), where the USBL apparatus is mounted on the UV. Similarly, the inverted short baseline (iSBL) proposed by Stovner, Johansen, and Schjølberg [11] is a network that only requires one transponder. However, instead of confining the array to an apparatus as in the iUSBL, the array in iSBL is confined to the size of the UV. This is similar to the SBL, hence the name. For a review of hydroacoustic sensor networks, it is referred to Vickery [12].

1.5 Background on Estimation

The KF was first published by Kalman [7] for the discrete-time systems, and extended to continuous-time systems the year later by Kalman and Bucy [5]. The EKF appeared already in Smith, Schmidt, and McGee [13] for position and velocity estimation of a spacecraft with nonlinear dynamics. In 1966, the Schmidt-Kalman filter (SKF) for estimation of a nonlinear system with constant biases without state augmentation was presented by Schmidt [14]. Another early development of the KF was the square-root formulation, in which the square root of the

covariance matrix is updated. This was developed in order to lower the precision requirement in the covariance matrix updates, which in turn reduced the computational load on the computers and made it more robust w.r.t. e.g. round-off errors and models with highly accurate measurements [15]. Gustafsson [16] notes that the square-root formulation is also useful when there are large scale differences between the states.

The unscented Kalman filter (UKF), as presented by Julier, Uhlmann, and Durrant-Whyte [17], is a nonlinear filtering method without the need for linearization and the computation of the Riccati equation. Instead, an *unscented transformation* is used, in which carefully selected *sigma points* are propagated through the nonlinear system in order to estimate the mean and covariance of the state and measurements. The unscented transformation can then be used in the KF. Another nonlinear filtering method is the particle filter (PF), which contrary to the UKF uses a large number of points called *particles*. The particles are essentially guesses of the state, and each is associated with a probability that also is updated. The probabilities of all particles constitute an estimate of the state's posterior distribution. The quality of estimation is determined by the number of particles, the need of which grows rapidly with the dimension of the problem. Thus, the PF is best suited for low-dimensional problems. [16]

Lastly, a special case of the XKF called the three-stage filter (3SF) has been used for position estimation by Johansen and Fossen [18] and Johansen, Fossen, and Goodwin [19]. The linearization point of the 3SF is provided by a linear KF, which employs a linear model achieved by an algebraic transformation (AT) of the nonlinear measurement model.

Attitude Estimation

For the reasons described above, estimation of a rigid body's attitude is an essential part of most navigation systems, whether it is in marine, terrestrial, aerial, or extraterrestrial applications. Solutions typically involve comparing nonparallel vector measurements in the rigid body's body-fixed frame to the corresponding known reference vectors in the global frame. Examples of this can be found in satellites, which often navigate by tracking known stars, and in marine, terrestrial, and aerial applications, in which body-fixed measurements of Earth's gravitational and magnetic fields are commonly used. The principle behind attitude estimation from vector measurements is the relationship

$$r^i = R_b^i r^b, \tag{1.13}$$

where a unit reference vector r is known in two frames: a global and often assumed *inertial* frame denoted $\{i\}$ and a body-fixed frame denoted $\{b\}$. The two vectors only differ by the rotation between the two frames, here parametrized by the *rotation matrix* R_b^i. With at least two nonparallel and noise-free vector pairs (r_1^i, r_1^b) and (r_2^i, r_2^b), the attitude can be determined.

Closely related to the development of attitude estimators has been the research and discussions on different attitude representations. Estimating a 3×3 rotation matrix, which is maybe the most straight-forward attitude representation, means estimating nine variables for three degrees-of-freedom (DOFs) which increase the computational complexity. Also, the necessary re-orthogonalization of the rotation matrix after corruption by round-off errors and other numerical effects is computationally expensive. The limited computational power on board early satellites did not permit this, and other representations had to be used. The *Euler angles*, consisting of three rotation variables *roll*, *pitch*, and *yaw*, are the most intuitive of the attitude representations, as they describe any rotation as three subsequent rotations about three standard axes. However, the kinematic equations and the construction of the rotation matrix from Euler angles use trigonometric functions, which are computationally expensive operations. Furthermore, the Euler angle representation contains a singularity, which is the case for all three-variable representations of a rotation [20]. Using the common Euler angle definition used in e.g. Robinson [21] and Fossen [22], the singularity appears in the kinematic equations at 90° pitch angle. The lowest dimension singularity-free attitude representation is the four-variable *quaternion*. The quaternion has desirable qualities for describing rotations: it has no singularities, is has linear kinematics, and is computationally efficient. However, due to the over-parametrization of the three rotations, the elements of the quaternion are not independent; they are related by the unit norm of the quaternion. Without imposing the unit norm constraint, the quaternion is not observable, which may not yield an invertible covariance matrix in a KF implementation. In many attitude estimators, the quaternion is therefore used to hold the attitude estimate, while three-variable representations are used to represent the attitude error. These may e.g. be the Gibbs vector or the modified Rodrigues parameter (MRP), both of which can be defined using the quaternion. Furthermore, they are both *minimal representations*, i.e. they use three variables for three rotations, but are not singularity free. Their singularities, however, can be argued to be less restricting than that of the Euler angles since they appear at 180 and 360 degrees, respectively. For more on attitude representations, it is referred to Shuster [23] and Markley [24]

An early attitude determination scheme was the point-to-point determination of the attitude by Black [25], which later was named the tri-axial attitude determination (TRIAD) algorithm [26]. TRIAD finds the rotation matrix explicitly from minimum two nonparallel vector pairs. The main weakness of the TRIAD algorithm is its sensitivity to noise. Bar-Itzhack and Harman [27] improves on this by calculating a weighted average of several different TRIAD solutions, but the achieved estimate is still not optimal in the sense of minimum variance. Wahba [28] posed the problem of finding the rotation matrix R_i^b that minimizes the cost function $J = \sum_{j=1}^{N} \|r_j^b - R_i^b r_j^i\|_2^2$ for N measurements. Davenport's q-method was the first useful analytical solution to Wahba's problem. However, it requires eigenvalue decomposition, which limited the frequency with which attitude estimates could be computed on the 1979 MAGSAT spacecraft [26]. This called for the quaternion estimator (QUEST) algorithm that since has been the most used solution to Wahba's problem. Although QUEST also has an analytical solution, numerical optimization is often preferred over the analytical approach for reasons of speed, accuracy, and reliability [26]. Numerous analytical and numerical solutions have been found for Wahba's famous problem, for which we refer to Shuster and Oh [29] and Markley and Mortari [30].

Early examples where the KF is used for attitude estimation are Paulson, Jackson, and Brown [31], Kau, P. Kumar, and Granley [32], and Farrell [33], where the Euler angle representation is used. Toda, Heiss, and Schlee [34] presented the first KF implementation using the quaternion that is known to the author. The quaternion representation appeared later in Lefferts, Markley, and Shuster [35] and Bar-Itzhack and Oshman [36], in which the multiplicative extended Kalman filter (MEKF) and additive extended Kalman filter (AEKF) were presented, though not with these names. The principal difference between the two is the way in which the attitude error, and thus also the correction, is formulated. In the MEKF, the error between the quaternion estimate and the quaternion representing the true attitude is described by a quaternion multiplication, which preserves its unit norm constraint. In the additive formulation, the error is represented as a subtraction. This violates the unit norm constraint, though with the correct accommodations, the two formulations have been shown to be identical. Shuster [37] clarifies this efficiently:

> *This writer senses the feeling among some workers that the additive and multiplicative implementations of the Kalman filter update express different but equally valid and not necessarily equivalent Kalman filter approaches. This is not true, the two approaches are exactly*

> *equivalent and should yield the same result within round-off error, as was demonstrated by Ferraresi [21][2]. The differences between the "additive" and "multiplicative" approaches is really only one of frame as pointed out a decade ago in reference [2][3]. Nonetheless, the terminology "additive" and "multiplicative" have become ingrained, for which this writer bears some responsibility.*

The real problem of the additive formulation is in the case of *unconstrained* estimation of the quaternion. The same work by Shuster is quoted to conclude this matter:

> *There does not, however, seem to be any benefit to unconstrained quaternion estimation, since it is more burdensome than constrained quaternion estimation, and, when one has finished, one must still do the work of restoring the constraint, which, by itself, is at least as difficult as constrained quaternion estimation. The unconstrained AEKF is faster than the constrained AEKF only if one accepts the unconstrained quaternion estimate as a substitute for the constrained quaternion estimate. The lack of constraint for the quaternion also brings with it special ills including the occasional failure of the estimation process. To this writer it seems that unconstrained quaternion estimation brings only extra burdens and no benefits.*

In this thesis work, the terms *additive* and *multiplicative* are used about the formulations of the quaternion error and in naming the AEKF and MEKF.

Further work on the AEKF was presented in Zanetti and Bishop [40] and Zanetti et al. [41], in which the quaternion constraint is imposed. Bonnabel, Martin, and Salaun [42] presented the invariant extended Kalman filter (IEKF), which exploits the symmetry of the attitude estimation problem. This supposedly leads in practice to a larger region of attraction. The geometric extended Kalman filter (GEKF) of Andrle and Crassidis [43] rectifies the frame inconsistency in the ARS bias correction of traditional attitude KFs. They note that the true and estimated ARS biases are described in the true and estimated body-fixed frames, respectively.

Nonlinear observers (NLOs) have in recent years received increasing attention for the attitude estimation problem. They often come with global or semi-global sta-

[2] Ferraresi [38]
[3] Shuster [39]

bility properties, which generally lacks for the EKF-based methods. Salcudean [44] presented an angular velocity observer with global convergence properties. Thienel and Sanner [45] proposed a nonlinear observer with GES estimation of attitude and bias, provided constant reference vectors, under a persistency of exitation (PE) requirement. Later, this requirement has been lifted by Mahony, Hamel, and Pflimlin [46] and Batista, Silvestre, and Oliveira [47–49]. Observers for time-varying reference vectors with semi-global stability results were developed by Hua [50] and Grip et al. [51], and Grip et al. [52] improved this to global stability. Batista, Silvestre, and Oliveira [48, 49] presented an attitude observer using a single time-varying and persistently non-constant reference vector.

The assumption that the vehicle is weakly accelerated is commonly used in attitude estimation, which allows the gravity vector to be used as a reference vector for the accelerometer measurement. Hua [50] and Martin and Salaün [53] developed a velocity and attitude observer based on global navigation satellite system (GNSS) velocity measurements that implicitly estimated the acceleration of the vehicle, thereby lifting this assumption. This idea was developed further in Johansen and Fossen [18] and Grip et al. [52, 54] where an acceleration estimate from a position, velocity, and acceleration observer was used to aid an attitude observer.

In Batista, Silvestre, and Oliveira [55] and Jørgensen and Schjølberg [56], acoustic sensor networks provide measurements for attitude estimation. Here, the principle is to use the relative inertial position of two transponders or body-fixed position of two transceivers as reference vectors, and find the corresponding body-fixed or inertial counterparts, respectively, from the acoustic sensor network.

Position Estimation

The electromagnetic GNSS signals attenuate rapidly in water, and can therefore not be used in underwater applications. However, the problem of position estimation using GNSS and hydroacoustic measurements are mathematically similar, so the field of GNSS-based position estimation is of great interest.

In GNSS applications, the range measurements are often modeled as *pseudo-ranges*, i.e. range measurements corrupted by a bias. The bias is additive and stems from a time offset between the transmitter and receiver clocks that is common for all pseudo-range measurements. An AT of the pseudo-range measurement equations for explicit calculation of the position and clock bias was presented in Bancroft [57] and Chaffee and Abel [58]. The explicit calculation is a noise-sensitive process, and integration of inertial and pseudo-range measurements is

adviced. KF-based solutions can be found in e.g. Grewal, Weill, and Andrews [59] and Farrell [60]. Vik and Fossen [61] presented a GES NLO that integrates an inertial navigation system (INS) and GNSS measurements assuming that the attitude is known. Grip et al. [52, 54] presented GES NLOs integrating INS and position measurements calculated from the GNSS measurements, which Johansen and Fossen [62] extended by using pseudo-range measurements directly. The latter was achieved by linearizing the nonlinear pseudo-range measurements, which came at the cost of only local stability.

A similar AT as that of Bancroft [57] and Chaffee and Abel [58] can be used to gain a linear time-varying (LTV) measurement model from the pseudo-range measurement equations with an additive bias. The LTV measurement model can in turn be implemented in a LTV KF that can easily be shown to be GES. The AT and KF are the two first stages of the 3SF of Johansen, Fossen, and Goodwin [19], and the third stage is the linearized KF using the estimate from the LTV KF as a linearization point. Instead of an LTV KF in the second stage, Johansen and Fossen [18] develops a GES NLO. This is computationally more efficient, as the NLO is less burdensome than a KF.

Hydroacoustic sensor networks are typically based on a reply-respond strategy, for which clock bias becomes irrelevant. However, the *wave speed*, i.e. the speed of sound in the surrounding water, is not exactly known and varies with temperature and salinity. This may be modeled as pseudo-ranges with a multiplicative bias that is common for all measurements. This model was used by Batista [63], where the nonlinear estimation problem was solved by state augmentation. This yields a linear estimation problem which was shown to have GES error dynamics, but comes at the cost of higher state dimension which inceases the computational load.

Alternatively, the wave speed can be calibrated separately, either offline, implicitly assuming that the water conditions do not vary, or online with temperature and salinity measurements as inputs to a wave speed model. Underwater position estimation with global stability results using bias-free range measurements was achieved by Batista, Silvestre, and Oliveira [64] for multiple transponders on the sea bed, and for a single transponder in Batista, Silvestre, and Oliveira [64]. Morgado et al. [65] achieved the same with a USBL network and a single transponder. All of these works applied state augmentation to deal with the nonlinearities.

An interesting method for using hydroacoustic measurements for attitude estimation was presented by Batista, Silvestre, and Oliveira [55]. There, a USBL set up provided body-fixed measurements of several transponders on the sea-bed with

known north-east-down (NED) position. This allowed for the use of a new reference vector pair for attitude estimation, i.e. the known and measured relative position of two transponders in the NED and body-fixed coordinate frames, respectively.

1.6 Research Questions

Here, the research questions that this thesis attempts to answer are stated.

Research Question 1: *Can the XKF method be applied to attitude estimation to yield a filter with similar performance as the MEKF, but with global stability?*

Research Question 2: *Can the XKF method be applied to position and wave speed estimation using an LBL network in order to improve performance w.r.t. stability and transient behavior, while maintaining the high accuracy of, the EKF?*

Research Question 3: *Can the iSBL network reduce the required installed infrastructure to one transponder while yielding adequate estimation accuracy? Furthermore, can the XKF method be applied to this problem to give global stability of the solution?*

Research Question 4: *Can the iSBL network with two transponders replace the generally unreliable magnetic field measurements? Furthermore, can the XKF method be applied to this problem to give global stability of the solution?*

Overarching Research Question: *What are the theoretical and practical limitations of the XKF and which implications do these have for AIN of underwater vehicles? Under which circumstances should other methods be preferred?*

1.7 Publications

The PhD work amounting to this thesis has resulted in two journal and four conference papers, which are listed below:

Journal papers:

[66] B. N. Stovner et al. “Attitude Estimation by Multiplicative eXogenous Kalman Filter”. In: *Automatica* Provisionally Accepted (2018)

[67] B. N. Stovner, T. A. Johansen, and I. Schjølberg. “Globally Exponentially

Stable Filters for Underwater Position Estimation Using A Single Hydroacoustic Transponder". In: *Ocean Engineering* Accepted (2018)

Conference papers:

[68] Bård B Stovner et al. "Three-stage Filter for Position and Velocity Estimation from Long Baseline Measurements with Unknown Wave Speed". In: *Proc. of the American Contr. Conf.* 2016, pp. 4532–4538

[11] B. B. Stovner, T. A. Johansen, and I. Schjølberg. "Globally Exponentially Stable Aided Inertial Navigation with Hydroacoustic Measurements from One Transponder". In: *Proc. of the American Contr. Conf.* 37.1 (2017), pp. 1219–1226

[69] B. B. Stovner and T. A Johansen. "Hydroacoustically Aided Inertial Navigation for Joint Position and Attitude Estimation in Absence of Magnetic Field Measurements". In: *Proc. of the American Contr. Conf.* 37.1 (2017), pp. 1211–1218

Conference paper not included in this thesis:

[70] E. K. Jørgensen, B. B. Stovner, and I. Schjølberg. "Experimental validation of three-stage position filter based on long baseline measurements with unknown wave speed". In: *Proc. of Conference on Control Technology and Applications*. IEEE, Aug. 2017, pp. 680–686

1.8 Outline and Contribution

This thesis is divided into three parts. Part I describes why these research problems are important and gives the relevant background information for understanding the methods and tools used and developed in this thesis. Specifically, Chapter 2 explains the notation and models of kinematics and measurements used throughout this thesis, while Chapter 3 describes the laboratory set-up used to experimentally verify and test the developed estimators.

In Part II, the work constituting the contribution of this thesis is given. Part II has been organized such that the chapters 4–7 attempt to answer research questions 1–4 of Section 1.6, respectively.

In Chapter 4, the multiplicative exogenous Kalman filter (MXKF) is developed and shown to be GES. Furthermore, it is shown through a simulations study and in experiments that it has identical steady-state performance as and better transient performance than the MEKF, the industry standard. This is an important results and a significant contribution, as it is the first of its kind: a GES KF-based filter with a minimal error state representation and with the high performance of the MEKF. This chapter is fully based on the work of Stovner et al. [66].

Chapter 5 considers the AIN of a UV with an LBL network and depth measurements when the wave speed is unknown. This requires the development of an AT similar to that of Bancroft [57] and Chaffee and Abel [58], but adapted to a multiplicative bias term. Furthermore, a 3SF is developed, based on this AT, and shown to be GES. This is the contribution from Stovner et al. [68]. Due to the low vertical disparity between transponders in most LBL networks, noise has a detrimental effect on the AT described above. This is improved in a novel AT presented here, which removes the vertical component with the aid of a depth measurement. It is shown that a calculated state estimate from the novel AT is accurate enough to be used as a linearization point in a linearized KF, which constitutes the second stage of the novel 3SF. A further improvement can be gained by employing a third stage KF, which uses a linearized model about the second stage estimate. A simulation study shows that the novel 3SF is a significant improvement from that of Stovner et al. [68]. Furthermore, it is shown that the the second stage KF in the novel 3SF performs almost as well as the third stage KF, meaning the latter can be excluded to save computational cost.

Chapter 6 considers the AIN of a UV with an iSBL network and depth measurements. Here, the wave speed is assumed to be known accurately. Multiple 3SFs are developed, using states decomposed in the NED and body-fixed coordinate frames. The filters are given in Stovner, Johansen, and Schjølberg [11, 67], and are developed here and shown to be GES. A simulation study shows that the AT developed in the latter is a significant improvement over that of the former. Furthermore, NED formulation is shown to be better that the body-fixed one. Also, the best second stage filter is shown to yield nearly as good performance as the best third-stage filter. This is an important result, as the third stage filter can be excluded to lower computational complexity.

When used for attitude estimation, it is assumed that the magnetometer measures Earth's magnetic field decomposed in the body-fixed coordinate frame. However, disturbances induced by e.g. the vehicle's motors or a subsea facility may

cause large disturbances that make the magnetometer measurements unsuitable for attitude estimation. Chapter 7 replaces magnetometer measurements in attitude estimation with an iSBL network with two or more transponders on the sea floor. Specifically, the calculated and estimated positions of the vehicle relative to the transponders decomposed in the body-fixed frame are used. From these, the transponder baselines, which are known in the NED frame, can be found in the body-fixed frame, constituting a vector pair suitable for attitude estimation. A 3SF is developed and shown to be GES, which through the three steps incrementally improves attitude and body-fixed position estimates.

In chapters 5–7, the proven GES of the filters and EKF-like performance achieved of the best ones are the main contributions. The best performing filters of Chapter 5 and 7 are previously unpublished.

Part III discusses the overarching research question in Section 1.6 about the limitations and utility of the XKF method in underwater state estimation. Also, it discusses future work that should be undertaken in the further development of the proposed methods.

Chapter 2

Modeling

In this chapter, necessary notation and models of kinematics and sensors are described.

2.1 Coordinate Frames

In this section, the coordinate frames used in this thesis are explained.

A vector, e.g. a position p, is described using the following mathematical notation:

$$p_{bc}^{a} = \begin{bmatrix} p_{bc,x}^{a} \\ p_{bc,y}^{a} \\ p_{bc,z}^{a} \end{bmatrix}. \tag{2.1}$$

This translates to the position of point c relative to point b decomposed in the coordinate frame a. The coordinate frame $\{a\}$ is defined by the placement of its origin, o_a, and by its axes $\vec{a}_x$, $\vec{a}_y$, and $\vec{a}_z$. This is shown in Figure 2.1. If b or c in the above notation were coordinate frames, it would simply mean the position of o_b or o_c, respectively.

- **ECI**: the earth-centered inertial (ECI) coordinate frame $\{e\}$ lies at the center of the earth and does not rotate with it. It is shown in Figure 2.2.
- **NED**: the NED coordinate frame $\{n\}$ is locally tangential to the earth's surface with its $\vec{n}_x$, $\vec{n}_y$, and $\vec{n}_z$ axes pointing north, east, and down, respectively. Its orientation therefore depends on where on earth its origin o_n is located. This is depicted in Figure 2.2.

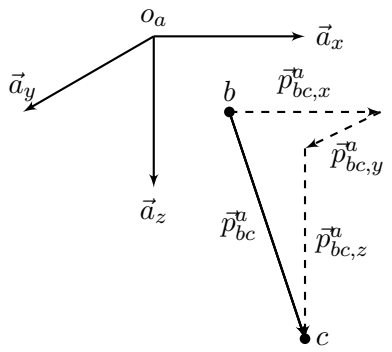

Figure 2.1: Coordinate frame $\{a\}$ defined by the axes $\vec{a}_x$, $\vec{a}_y$, and $\vec{a}_z$. The position of the point c relative to point c decomposed in the coordinate frame a is given by the vector $p^a_{bc} = [p^a_{bc,x}, p^a_{bc,y}, p^a_{bc,z}]^\top$.

- **BODY**: the body-fixed coordinate frame $\{b\}$ has axes that move with the vehicle. Its $\vec{b}_x$, $\vec{b}_y$, and $\vec{b}_z$ axes point forwards, to the right, and downwards, respectively. Its origin may be placed wherever it is suitable in the body of the vehicle. This is depicted in Figure 2.3.

2.2 Attitude Representations and Kinematics

The attitude of a rigid body is the imaginary rotation needed to align the axes of a reference frame to the axes of the rigid body's body-fixed frame. The attitude of a rigid body can be represented in a number of ways, the relevant of which will be presented here.

In the following, we let the NED coordinate frame be the reference frame.

2.2.1 Rotation Matrix

The attitude may be represented by the rotation matrix R^n_b, which is a nine-parameter representation. A vector known in one frame can be found in the other by

$$y^n = R^n_b y^b$$
$$y^b = R^{n\top}_b y_n.$$

The kinematics of the rotation matrix is given by

$$\dot{R}^n_b = R^n_b S(\omega^b_{nb}),$$

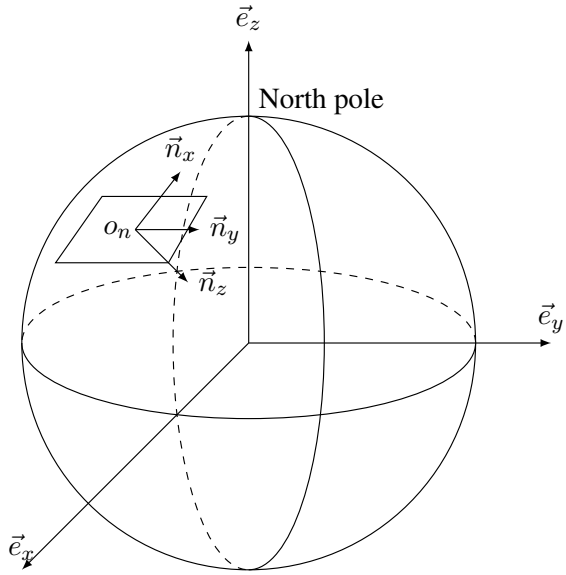

Figure 2.2: The ECI and NED coordinate frame. The locally tangential plane can be seen to intersect earth's surface at the origin of the NED frame o_n.

where ω_{nb}^b is the angular velocity and $S(\omega)$ is the skew-symmetric matrix

$$S(\omega) = \begin{bmatrix} 0 & -\omega_z & \omega_y \\ \omega_z & 0 & -\omega_x \\ -\omega_y & \omega_x & 0 \end{bmatrix}.$$

2.2.2 Euler Angles

There are many ways in which the Euler angles may be defined. Adopting the definition from Robinson [21] and Fossen [22], the Euler angles represent the attitude as the three subsequent rotations about the z-, y'-, and x"- axes called *yaw*, *pitch*, and *roll*, respectively, where y' is the resulting axis after the rotation about the z-axis and x" is the resulting axis after the rotations about the z- and the y'-axes.

The Euler angles representing the rotation from the body-fixed to NED coordinate system is given by

$$\Phi_b^n = \begin{bmatrix} \phi \\ \theta \\ \psi \end{bmatrix},$$

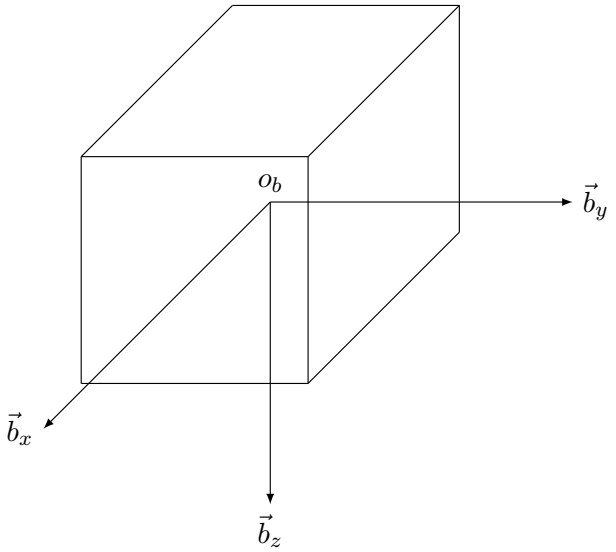

Figure 2.3: The body-fixed coordinate system.

where ϕ, θ, and ψ are the roll, pitch, and yaw angles, respectively. The rotation matrix is contructed from the Euler angles by

$$R_b^n = R(\Phi_b^n) = \begin{bmatrix} \mathrm{c}\psi\mathrm{c}\theta & -\mathrm{s}\psi\mathrm{c}\phi + \mathrm{c}\psi\mathrm{s}\theta\mathrm{s}\phi & \mathrm{s}\psi\mathrm{s}\phi + \mathrm{c}\psi\mathrm{c}\phi\mathrm{s}\theta \\ \mathrm{s}\psi\mathrm{c}\theta & \mathrm{c}\psi\mathrm{c}\phi + \mathrm{s}\phi\mathrm{s}\theta\mathrm{s}\psi & -\mathrm{c}\psi\mathrm{s}\phi + \mathrm{s}\psi\mathrm{c}\phi\mathrm{s}\theta \\ -\mathrm{s}\theta & \mathrm{c}\theta\mathrm{s}\phi & \mathrm{c}\theta\mathrm{c}\phi \end{bmatrix},$$

where $\mathrm{s}\cdot = \sin(\cdot)$, $\mathrm{c}\cdot = \cos(\cdot)$, and $\mathrm{t}\cdot = \tan(\cdot)$.

The kinematics of the Euler angles are given by

$$\begin{aligned} \dot{\Phi}_b^n &= T(\Phi_b^n)\omega_{nb}^b \\ T(\Phi_b^n) &= \begin{bmatrix} 1 & \mathrm{s}\psi\mathrm{t}\theta & \mathrm{c}\psi\mathrm{t}\theta \\ 0 & \mathrm{c}\psi & -\mathrm{s}\psi \\ 0 & \mathrm{s}\psi/\mathrm{c}\theta & \mathrm{s}\psi/\mathrm{c}\theta \end{bmatrix}. \end{aligned}$$

We see that the singularity of this Euler angle representation is at $\theta = \pi/2 + n\pi$ for all integers n.

2.2.3 Unit Quaternions

The attitude represented by the unit quaternion q_b^n is composed by a scalar rotation η about an imaginary axis $\varepsilon = [\varepsilon_x, \varepsilon_y, \varepsilon_z]^\top$ as

$$q_b^n = \begin{bmatrix} \eta \\ \varepsilon \end{bmatrix}. \tag{2.2}$$

It is a unit quaternion, meaning $\|q_b^n\|_2 = 1$.

The rotation matrix can be constructed from the quaternion by

$$R_b^n = R(q_b^n) = I_3 + 2\eta S(\varepsilon) + 2S^2(\varepsilon) = \Xi(q_b^n)^\top \Psi(q_b^n), \tag{2.3}$$

where

$$\Xi(q_b^n) = \begin{bmatrix} -\varepsilon^\top \\ \eta I_3 - S(\varepsilon) \end{bmatrix}, \qquad \Psi(q_b^n) = \begin{bmatrix} -\varepsilon^\top \\ \eta I_3 + S(\varepsilon) \end{bmatrix}. \tag{2.4}$$

From (2.3), we see that the quaternions $q_b^n = [1, 0, 0, 0]^\top$ and $q_b^n = [-1, 0, 0, 0]^\top$ both represent zero rotations. This reveals a the *quaternion ambiguity*: any rotation has two quaternion representations of opposite sign, i.e. $R(q) \equiv R(-q)$.

Let $q_{\hat{b}}^n \triangleq [\hat{\eta}, \hat{\varepsilon}]^\top$ be an estimate of q_b^n. Now, the *multiplicative error* can be found by

$$\delta q = \begin{bmatrix} \delta\eta \\ \delta\varepsilon \end{bmatrix} \triangleq q_b^{\hat{b}} = (q_{\hat{b}}^n)^{-1} \otimes q_b^n, \tag{2.5}$$

where $(q_b^n)^{-1} = [\eta, -\varepsilon]^\top / \|q_b^n\|_2$ is the quaternion inverse and $\otimes$ denotes the Hamilton product

$$q_1 \otimes q_2 = \begin{bmatrix} \eta_1 \\ \varepsilon_1 \end{bmatrix} \otimes \begin{bmatrix} \eta_2 \\ \varepsilon_2 \end{bmatrix} = \begin{bmatrix} \eta_1\eta_2 - \varepsilon_1^\top \varepsilon_2 \\ \eta_1\varepsilon_2 + \eta_2\varepsilon_1 - S(\varepsilon_1)\varepsilon_2 \end{bmatrix} = q_1\eta_2 + \Psi(q_1)\varepsilon_2. \tag{2.6}$$

The Hamilton product conserves the norm constraint on the unit quaternion. Alternatively, the error between $q_{\hat{b}}^n$ and q_b^n can be expressed by the *additive error*

$$\tilde{q} \triangleq q_b^n - q_{\hat{b}}^n. \tag{2.7}$$

The kinematics of the unit quaternion is

$$\dot{q}_b^n = \frac{1}{2}\Xi(q_b^n)\omega_{nb}^b = \frac{1}{2}\Omega(\omega_{nb}^b)q_b^n, \tag{2.8}$$

where

$$\Omega(\omega_{nb}^b) = \begin{bmatrix} 0 & -\omega_{nb}^{b\,\top} \\ \omega_{nb}^b & -S(\omega_{nb}^b) \end{bmatrix}.$$

2.2.4 Modified Rodrigues Parameter

The MRP is a three-variable representation of the attitude. Here, it is introduced as a means of mapping the four parameters of the quaternion down to three parameters. However, it can be used independently of quaternions as an attitude representation.

From the quaternion q_b^n, we find the MRP as

$$u_b^n = \frac{\varepsilon}{1+\eta} \tag{2.9}$$

which clearly contains a singularity at $\eta = -1$, i.e. a 360° rotation. A vehicle aligned with NED that starts rotating in e.g. yaw will trigger the MRP singularity when it has completed a full round. Since q_b^n and $-q_b^n$ represents the same rotation, there must exist two MRPs representing the same rotation as well. The alternative MRP for u_b^n is called its *shadow set* and can be found by

$$u_{b,ss}^n = \frac{-\varepsilon}{1-\eta}\frac{(1+\eta)^2}{(1+\eta)^2} = -\frac{u_b^n}{\frac{1-\eta^2}{(1+\eta)^2}} = -\frac{u_b^n}{u_b^{n\top} u_b^n}.$$

Therefore, the MRP singularity can be avoided by switching between shadow-set representations.

The rotation matrix can be found from the MRP by

$$R_b^n = R(u_b^n) = I_3 - \frac{4(1 - u_b^{n\top} u_b^n) S(u_b^n) + S(u_b^n)^2}{(1 + u_b^{n\top} u_b^n)^2}. \tag{2.10}$$

The dynamics of the MRP is

$$\dot{u}_b^n = \frac{1}{2}\left(\frac{1}{2}\left(1 - u_b^{n\top} u_b^n\right) I_3 + S(u_b^n) + u_b^n u_b^{n\top}\right)\omega_{nb}^b. \tag{2.11}$$

For more on the MRP, the reader is referred to Markley and Crassidis [26], Crassidis and Markley [71], and Karlgaard and Schaub [72].

2.3 Position Representations and Kinematics

2.3.1 North-East-Down Formulation

The position, velocity, and acceleration of a vehicle relative NED decomposed in NED are denoted p^n_{nb}, v^n_{nb}, and a^n_{nb}, and are linked by

$$\dot{p}^n_{nb} = v^n_{nb} \tag{2.12a}$$
$$\dot{v}^n_{nb} = a^n_{nb}. \tag{2.12b}$$

2.3.2 Body-Fixed Formulation

The position of a vehicle relative a transponder decomposed in the body-fixed coordinate frame is denoted p^b_{tb}. From

$$\begin{aligned}\dot{p}^b_{tb} &= \frac{\mathrm{d}}{\mathrm{d}t} R^{n\top}_b(-p^n_{nt} + p^n_{nb}) = -S(\omega^b_{nb}) R^{n\top}_b(-p^n_{nt} + p^n_{nb}) + R^{n\top}_b v^n_{nb} \\ &= -S(\omega^b_{nb}) p^b_{tb} + v^b_{nb},\end{aligned}$$

we see that v^b_{nb} is a reasonable choice for the body-fixed velocity state. Similarly, it can be shown that

$$\dot{v}^b_{nb} = -S(\omega^b_{nb}) v^b_{nb} + a^b_{nb}.$$

The body-fixed kinematics is summarized as

$$\dot{p}^b_{tb} = -S(\omega^b_{nb}) p^b_{tb} + v^b_{nb} \tag{2.13}$$
$$\dot{v}^b_{nb} = -S(\omega^b_{nb}) v^b_{nb} + a^b_{nb}. \tag{2.14}$$

This representation of a position arises naturally in the iSBL measurement equations since its baselines are known in the body-fixed coordinate frame.

2.4 Sensor Models

2.4.1 Inertial Measurement Unit and Magnetometer

An IMU consists of a three-axial accelerometer and an ARS. Additionally, many IMUs are equipped with a magnetometer, though it is not an inertial sensor.

Accelerometers measure the acceleration of a vehicle relative to free-fall. This means that when an accelerometer lies still relative to the ground, it measures the

acceleration of gravity pointing upwards, i.e. in the negative n_z-direction. This is called the *specific force*, and its measurement is modeled by

$$f^b_{nb,m} = a^b_{nb} - R^{n\top}_b g^n + \epsilon_{acc}, \tag{2.15}$$

where a^b_{nb} is the true acceleration of the vehicle and ϵ_{acc} is an unbiased white noise with standard deviation σ_{acc}, i.e. $\epsilon_{acc} \sim \mathcal{N}(0, \sigma^2_{acc})$. Note that this assumes that the body-fixed frame coincides with the IMU.

The ARS measurement is modeled by

$$\omega^b_{nb,m} = \omega^b_{nb} + b^b_{ars} + \epsilon_{ars}, \tag{2.16}$$

where $\epsilon_{ars} \sim \mathcal{N}(0, \sigma^2_{ars})$ and b^b_{ars} is assumed to be a slowly varying bias term modeled by a Wiener process [see e.g. 22, p.306]

$$\dot{b}^b_{ars} = \epsilon_b,$$

where $\epsilon_b \sim \mathcal{N}(0, \sigma^2_b)$.

The magnetometer measurement is modeled by

$$m^b_m = R^{n\top}_b m^n + \epsilon_{mag}, \tag{2.17}$$

where m^n is Earth's magnetic field decomposed in the NED coordinate frame and $\epsilon_{mag} \sim \mathcal{N}(0, \sigma^2_{mag})$.

2.4.2 Hydroacoustic Measurements

The acoustic measurements come in this thesis from two different hydroacoustic sensor networks: LBL and iSBL.

Long Baseline

In the LBL set-up, the vehicle carries one transceiver that measures the TOA from several transponders mounted in the vehicle's surroundings, seen in Figure 2.4. The LBL measurements are modeled by

$$y_i = \alpha \| - p^n_{nt_i} + p^n_{nb} + R^n_b p^b_{bc} \|_2 + \epsilon_{y,i}, \tag{2.18}$$

where $p^n_{nt_i}$ is the position of transponder t_i relative NED, p^b_{bc} is the position of the tranceiver c on the vehicle, and $\epsilon_{y,i} \sim \mathcal{N}(0, \sigma^2_{y,i})$. α is a *wave speed error factor* that allows us to estimate the wave speed, i.e. the speed of sound in the surrounding water.

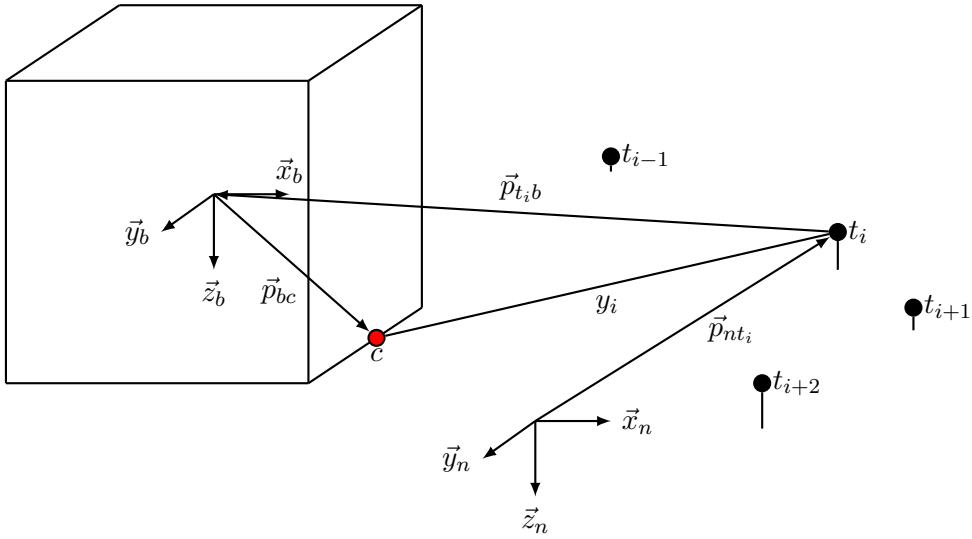

Figure 2.4: The configuration of one transceiver (red) and N LBL transponders (black) on the sea floor.

Inverted Short Baseline

In the iSBL set-up, the vehicle carries one transmitting transducer, called a *sender*, and M receiving transducers, called *receivers*. The Mth receiver is mounted near the sender, so we assume their positions coincide. In the vehicle's surroundings there are one or more transponders, denoted t or t_i respectively, that receive a signal from the sender and subsequently respond. Now, receiver c_M measures the TOA of the transponders' responses, while receivers $c_j, j = 1, ..., M-1$ measure the TDOA between c_j and c_M. The range measurement is modeled by

$$y_{iM} = \|p^n_{nb} - p^n_{nt_i} + R^n_b p^b_{bc_M}\|_2 + \epsilon_{y,iM} \tag{2.19a}$$
$$= \|p^b_{t_ib} + p^b_{bc_M}\|_2 + \epsilon_{y,iM} \tag{2.19b}$$

and the $M-1$ range difference measurements are modeled by

$$\partial y_{ij} = \|p^n_{nb} - p^n_{nt_i} + R^n_b p^b_{bc_M}\|_2 - \|p^n_{nb} - p^n_{nt_i} + R^n_b p^b_{bc_M}\|_2 + \epsilon_{\partial,ij} \tag{2.20a}$$
$$= \|p^b_{t_ib} + p^b_{bc_j}\|_2 - \|p^b_{t_ib} + p^b_{bc_m}\|_2 + \epsilon_{\partial,ij}. \tag{2.20b}$$

Notice that the iSBL measurements are not modeled with the wave speed error factor α. This assumes that the wave speed is known. The iSBL sensor network can be seen in Figure 2.5

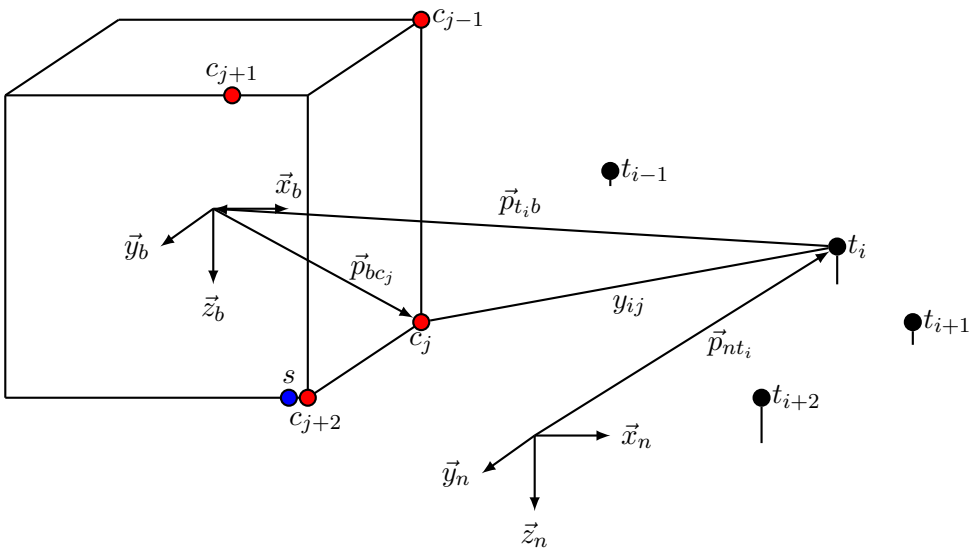

Figure 2.5: The configuration of M iSBL receivers (red), an iSBL sender (blue), and N transponders (black).

2.4.3 Pressure as Depth Measurement

Accurately calibrated pressure measurements can provide accurate measurements of the vehicle's position along the $\vec{n}_z$-axis. This is modeled as

$$d_m = p^n_{nb,z} + \epsilon_d, \tag{2.21}$$

where $\epsilon_d \sim (0, \sigma_d^2)$.

Chapter 3

Experimental Set-Up

3.1 Laboratory Facilities

The experiments in this thesis are conducted in Marine Cybernetics Laboratory (MCLab), a 40 meters long, 6.5 meters wide, and 1.5 meters deep water tank at Norwegian University of Science and Technology (NTNU). The water tank is equipped with 6 Qualisys Oqus Underwater cameras. The camera system measures the positions of reflective markers placed on a vehicle. These are used to calculate the true position and attitude of the vehicle.

3.2 Hydroacoustics

In this section, the hydroacoustic range measurement system is described. The hardware available in this thesis was bought from Water Linked AS. It consists of specialized computer hardware allowing the transmission and reception of discretized signals through transmitting and receiving hydroacoustic transducers.

All transducers, i.e. the ones on the vehicle and the ones on the pool floor, are connected to the same specialized computer with 4 channels for receiving and 4 for transmitting. Receivers and transmitters begin recording and transmitting simultaneously. Therefore, we know that the transmitted signal is present in each recording, and that the time at which it is detected is the TOA. This means that the experimental set-up is simpler than the set-up modeled in the simulations in this thesis. This was due to limitations on the available hardware.

Below, a simplified overview of the measurement retrieval strategy is given.

1. Start transmitting N_t and receiving N_r samples simultaneously
2. In the recording, detect the TOA of the transmitted signal
3. Calculate range measurement from the TOA

When a signal is transmitted, the signal must be recognized on the receiver and the TOA detected. This requires design of a signal that is easily detectable, which is discussed in Section 3.2.1. Further, signal processing must be developed to detect the transmitted signal on the receiver side. This is discussed in Section 3.2.2.

3.2.1 Signal Design

The most important quality of the signal is that the transmitted sequence of samples must be easily detectable in the recorded sequence of samples. The detection is done by correlating the transmitted sequence with the recorded sequence, which means that the correlation properties of the designed sequence are of key importance. Preferrably, the signal should have zero auto-correlation when the *lag* is nonzero. The lag is the number of samples that one of the sequences is shifted relative to the other, where zero lag means the sequences overlap perfectly. A class of sequences that hold this property in theory is Zadoff-Chu-sequences, given by

$$x(n) = \exp\left(-\frac{\pi i u n(n+1)}{N_{ZC}}\right), n \in (1, N_{ZC}), \tag{3.1}$$

where $i = \sqrt{-1}$, n is the sample index, u is the root of the sequence, and N_{ZC} is the prime length of the sequence. [73]

The transducers work best at frequencies between 50-250 kHz. Therefore, the Zadoff-Chu sequences must be designed within a desired frequency interval. This is also important when multiple transmitters are to send simultaneously. Then, the transmitted sequences are differentiable on the receiving end if they are separated in the frequency domain. Through trial and error, the choice of

$$\frac{u}{N_{CZ}} = 6.56 \cdot 10^{-6}(f_{high} - f_{low})N$$

in (3.1) was found to yield an appropriate Zadoff-Chu sequence within the frequency domain (f_{low}, f_{high}) of desired length N. This sequence is additionally band-pass filtered in the given interval. The above does not produce a sequence of length N, but a non-zero sequence of approximately N samples with tails of approximately zero values before and after it. From this, the N samples of *valuable* information in the middle can be extracted.

3.2.2 Signal Processing

Here, the signal processing algorithm is first stated, before its steps are explained in the following.

Given the transmitted sequence t and the received sequence r containing t, the signal processing can be summarized in the following steps:

1. Correlate t and r to produce the correlation sequence c_1
2. Auto-correlate t to produce the correlation sequence a_t
3. Correlate c_1 and a_t to produce c_2
4. Find the first significant peak in c_2.

Denote the correlation of t and r by c_1. Ideally, c_1 would be zero where the transmitted and received sequences did not overlap perfectly, and a clear peak when they did. Then, it would be trivial to find the lag at which the peak occurs, from which the TOA could be calculated. However, due to noise, multipath, and an imperfect sequence t, there are multiple peaks in c_1 and it can be hard to distinguish the peak representing the *direct path* from the other peaks.

The sequence t is imperfect because it does not have zero auto-correlation when the lag is non-zero, as seen in Figure 3.1. This is likely due to the way in which it is created. The sequence c_1 is expected to contain peaks before the direct path peak in a similar manner as in Figure 3.1. This information can be used constructively, namely by correlating the interval between the red lines in Figure 3.1, a sequence we denote a_t, with c_1. This means that we search for the first appearing pattern of peaks in c_1 that resemble the expected pattern a_t. The resulting sequence from the correlation of c_1 and a_t is denoted c_2. The difference between c_1 and c_2 can be seen in Figure 3.2 and 3.3.

The direct path peak is distinguishable from the multipath peaks because it always appears first. This is due to the direct path being shorter than the multipaths. In Figure 3.2, the multipath peaks is seen to be far greater than the direct path peak. This makes selecting the direct path peak from c_1 particularly difficult. For instance, it is not obvious that the peak marked in red in Figure 3.3(a) is the direct path peak and not the preceding or the succeeding peak, and the example displayed in Figure 3.2 and 3.3 is far from the hardest to analyze. In c_2, distinguishing the

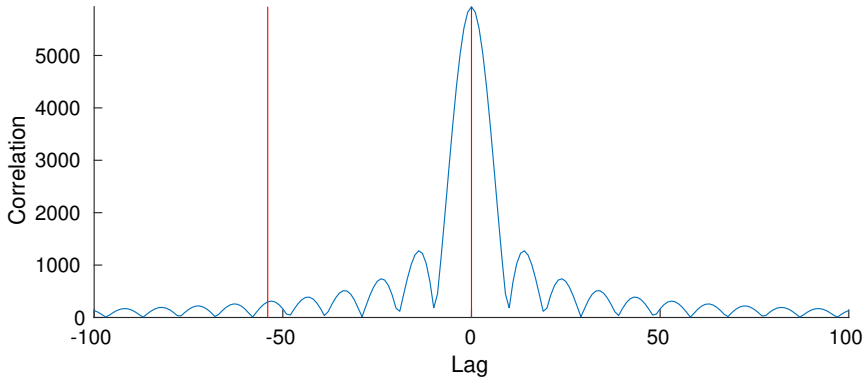

Figure 3.1: The auto-correlation of t about zero lag in blue. The sequence between the red lines are denoted a_t and used for the second correlation.

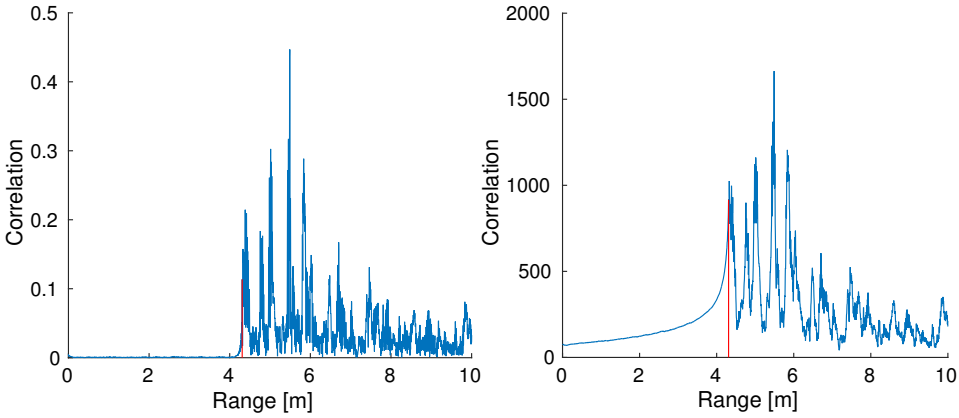

(a) The correlation sequence c_1.

(b) The correlation sequence c_2.

Figure 3.2: The correlation sequences c_1 and c_2 between 0 and 10 meters. The red line marks the direct path peak at 4.309m.

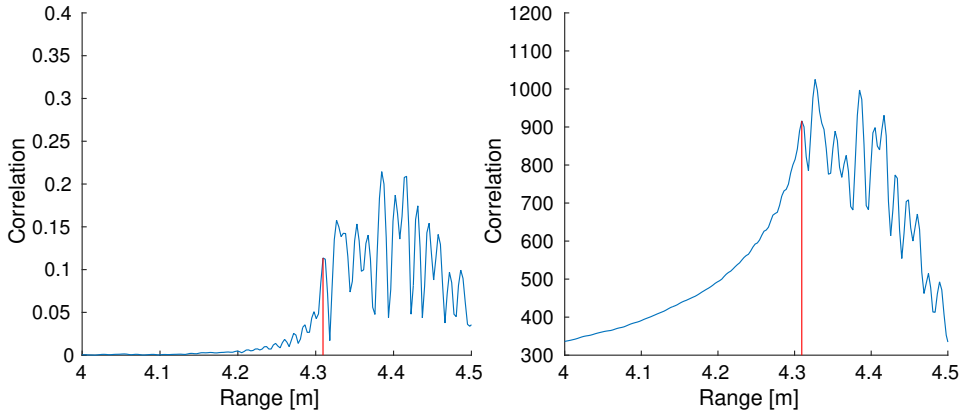

(a) The correlation sequence c_1.

(b) The correlation sequence c_2.

Figure 3.3: A closer look at the same correlation sequences as in Figure 3.2 about the direct path peak.

direct path peak from the multipath peaks have become much simpler as the preceding peaks in c_1 have vanished, and the first significant peak represents the direct path.

The algorithm searching for the first significant peak is not covered here, as it is an ad hoc algorithm that does not provide much insight.

3.2.3 Range Filtering

In Figure 3.4, the 16 ranges measured from the 4 transmitters to the 4 receivers are shown along with the true ranges calculated from the position and attitude output by the Oqus camera system. We see that there are some outlier range measurements. These are filtered out by a simple outlier rejection algorithm. It rejects the current range measurement if the difference between the current range and the last accepted range is larger than some limit. This limit is proportional to the time difference between the current range and the last accepted range. The slope of this limit is a tuning variable, and should be set to the maximum plausible speed of the vehicle.

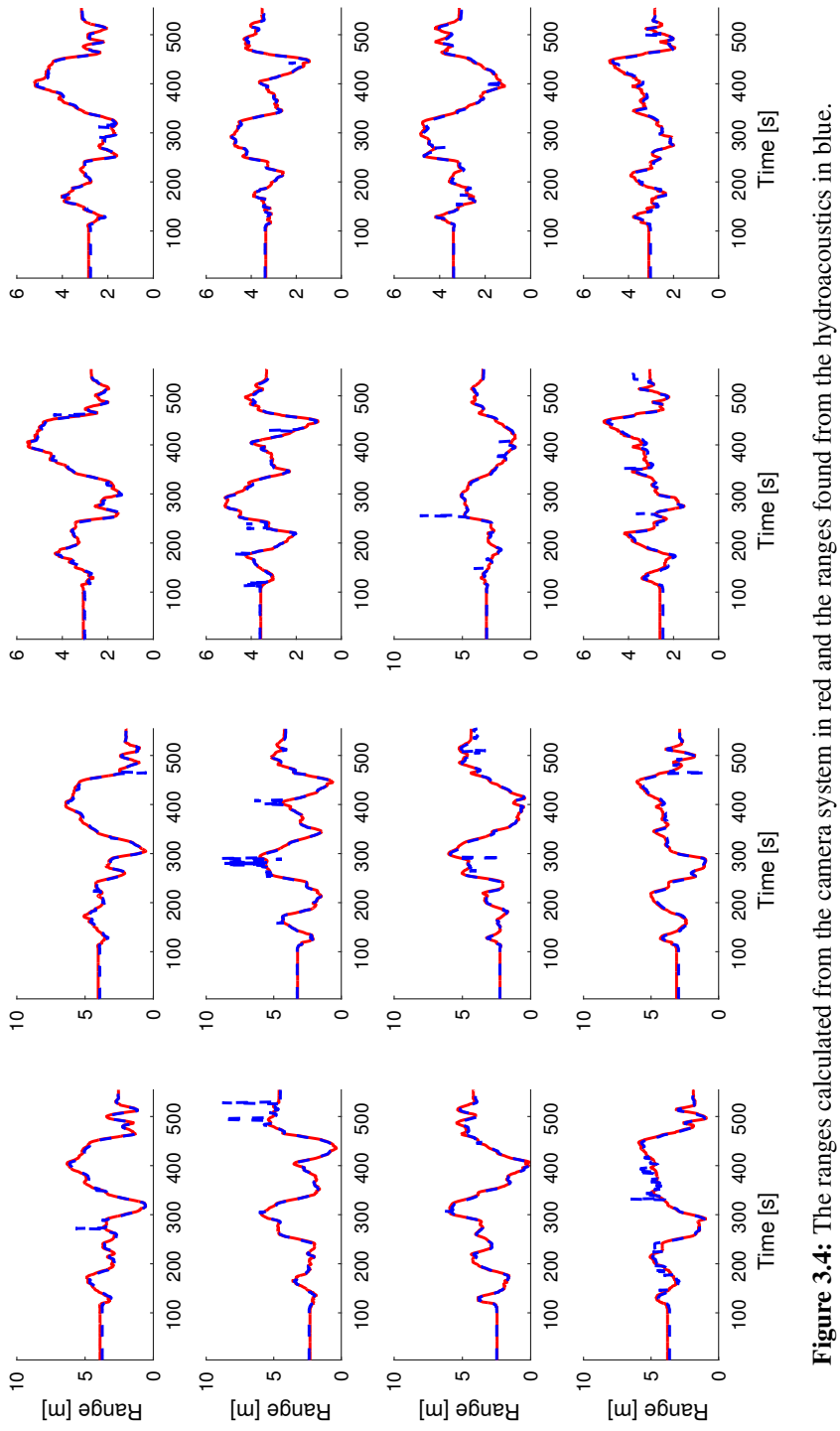

Figure 3.4: The ranges calculated from the camera system in red and the ranges found from the hydroacoustics in blue.

Part II

Research Contributions

Chapter 4

The Multiplicative eXogenous Kalman Filter for Attitude Estimation

This chapter is based on the work of Stovner et al. [66], in which a novel GES KF-based attitude and ARS bias estimator is developed. Furthermore, it is shown to yield similar performance in both simulations and experiments as the MEKF. This is a significant contribution as it provides an estimator with global stability properties and the high estimation accuracy of one of the industry standard solutions, the MEKF. Using the GES NLO of Grip et al. [52] and building on the results of Johansen and Fossen [74], the filter is developed and its global stability is proven. Beyond the theoretically guaranteed robustness and transient performance, the MXKF is compared in simulations and experimentally with the NLO and an MEKF.

4.1 Preliminaries

The true state and NLO and linearized KF state estimates z, $\bar{z}$, and $\hat{z}$, respectively, are defined as

$$z \triangleq \begin{bmatrix} q_b^{n\star} \\ b_{ars}^b \end{bmatrix}, \quad \bar{z} \triangleq \begin{bmatrix} q_{\bar{b}}^n \\ \bar{b}_{ars}^{\bar{b}} \end{bmatrix}, \quad \hat{z} \triangleq \begin{bmatrix} q_{\hat{b}}^n \\ \hat{b}_{ars}^{\hat{b}} \end{bmatrix}, \tag{4.1}$$

where $\bar{b}_{ars}^{\bar{b}}$ and $\hat{b}_{ars}^{\hat{b}}$ are the NLO's and linearized KF's ARS bias estimates decomposed in their respective frames, and $q_b^{n\star}$ resolves the quaternion ambiguity by the following definition.

Definition 4.1.1. *Define $q_b^{n\star}$ as the one of q_b^n and $-q_b^n$ that is closest to $q_{\hat{b}}^n$, i.e.*

$$q_b^{n\star} \triangleq \begin{cases} q_b^n, & \text{if } {q_{\hat{b}}^n}^\top q_b^n \geq 0 \\ -q_b^n, & \text{if } {q_{\hat{b}}^n}^\top q_b^n < 0 \end{cases}. \tag{4.2}$$

Furthermore, the true quaternion and its NLO and linearized KF estimates are composed of

$$q_b^{n\star} = \begin{bmatrix} \eta \\ \varepsilon \end{bmatrix}, \; q_{\bar{b}}^n = \begin{bmatrix} \bar{\eta} \\ \bar{\varepsilon} \end{bmatrix}, \; q_{\hat{b}}^n = \begin{bmatrix} \hat{\eta} \\ \hat{\varepsilon} \end{bmatrix}, \tag{4.3}$$

respectively.

Definition 4.1.1 requires that the multiplicative and additive errors (2.5) and (2.7), respectively, are redefined:

$$\delta q = \begin{bmatrix} \delta\eta \\ \delta\varepsilon \end{bmatrix} \triangleq (q_{\hat{b}}^n)^{-1} \otimes q_b^{n\star} \tag{4.4}$$

$$\tilde{q} \triangleq q_b^{n\star} - q_{\hat{b}}^n. \tag{4.5}$$

The measurements are modeled by

$$y_i^b = R(q_b^n)^\top y_i^n + \epsilon_{y,i}, \tag{4.6}$$

where $\epsilon_{y,i} \sim \mathcal{N}(0, \sigma_{y,i}^2)$. Furthermore, as mentioned in Section 1.5, two nonparallel vector measurements are needed for attitude determination. This is stated by the following assumption:

Assumption 4.1.1. *At least two reference vectors y_1^n and y_2^n are nonparallel, i.e., there exists a positive constant γ such that $|y_1^n \times y_2^n| \geq \gamma > 0$.*

4.2 Nonlinear Observer

Figure 4.1 shows the role of the NLO in the structure of the MXKF. Any NLO estimating the attitude and ARS bias with strong convergence properties can be used. Here, the attitude observer from Grip et al. [52] is used, which with a rotation

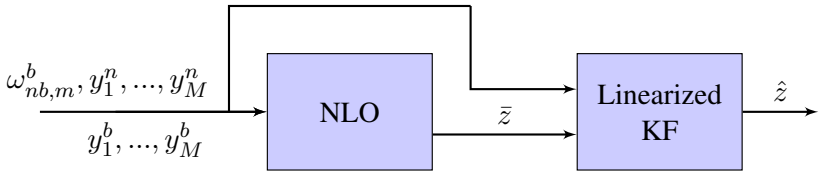

Figure 4.1: The structure of the MXKF.

matrix attitude estimate $\bar{R}^n_{\bar{b}}$ is given by

$$\dot{\bar{R}}^n_{\bar{b}} = \bar{R}^n_{\bar{b}} S(\omega^b_{nb,m} - \bar{b}^{\bar{b}}) + \sigma K_P J(\bar{R}^n_{\bar{b}}, t) \tag{4.7a}$$

$$\dot{\bar{b}}^{\bar{b}} = \text{Proj}(\bar{b}^{\bar{b}}, -k_I \text{vex}(\mathbb{P}(\bar{R}^{n\top}_{\bar{b}\,s} K_P J(\bar{R}^n_{\bar{b}}, t)))) \tag{4.7b}$$

$$J(R^n_b, t) = \sum_{j=1}^{3} (w^n_j - R^n_b w^b_j) w^{b\top}_j \tag{4.7c}$$

$$w^\iota_1 = \frac{y^\iota_1}{\|y^\iota_1\|_2}, w^\iota_2 = \frac{S(y^\iota_1) y^\iota_2}{\|S(y^\iota_1) y^\iota_2\|_2}, w^\iota_3 = \frac{S(y^\iota_1)^2 y^\iota_2}{\|S(y^\iota_1)^2 y^\iota_2\|_2},$$

where $\iota \in (n, b)$, K_P is a symmetric positive-definite gain matrix, k_I is a strictly positive scalar gain, $\sigma \geq 1$ is a stability tuning factor, $\bar{R}^n_{\bar{b}\,s}$ is the matrix $\bar{R}^n_{\bar{b}}$ with all its elements saturated between ± 1, Proj is a projection function that ensures $\|\bar{b}^{\bar{b}}\| \leq \bar{M}$ for $\bar{M} > M$ where M is an a priori known upper bound on the ARS bias, i.e. $\|b^b\| < M$, $\mathbb{P}(X) = 0.5(X + X^\top)$ for any square matrix X, and $\text{vex}(S(x)) = x$. Note that $\bar{R}^n_{\bar{b}}$ is not always on SO(3), but it *converges to* SO(3). When $\bar{R}^n_{\bar{b}}$ is projected onto SO(3), the result is denoted $R^n_{\bar{b}}$.

Denote by $\bar{\Sigma}$ the dynamics of the estimation error $R(q^n_b) - \bar{R}^n_{\bar{b}}$ and $b^b - \bar{b}^{\bar{b}}$. Let $q^n_{\bar{b}}$ be extracted from $R^n_{\bar{b}}$ in such a way that it forms a continuous signal, and does not jump between the two representation $q^n_{\bar{b}}$ and $-q^n_{\bar{b}}$.

Proposition 4.2.1. *The origin* $R(q^n_b) - \bar{R}^n_{\bar{b}} = 0_3$ *and* $b^b - \bar{b}^{\bar{b}} = 0$ *of* $\bar{\Sigma}$ *is GES.*

Proof. The proof is given in Grip et al. [52]. □

4.3 Linearized Kalman Filter

In this section, the linearized KF part of the MXKF is derived. The derivation is conducted in the following steps:

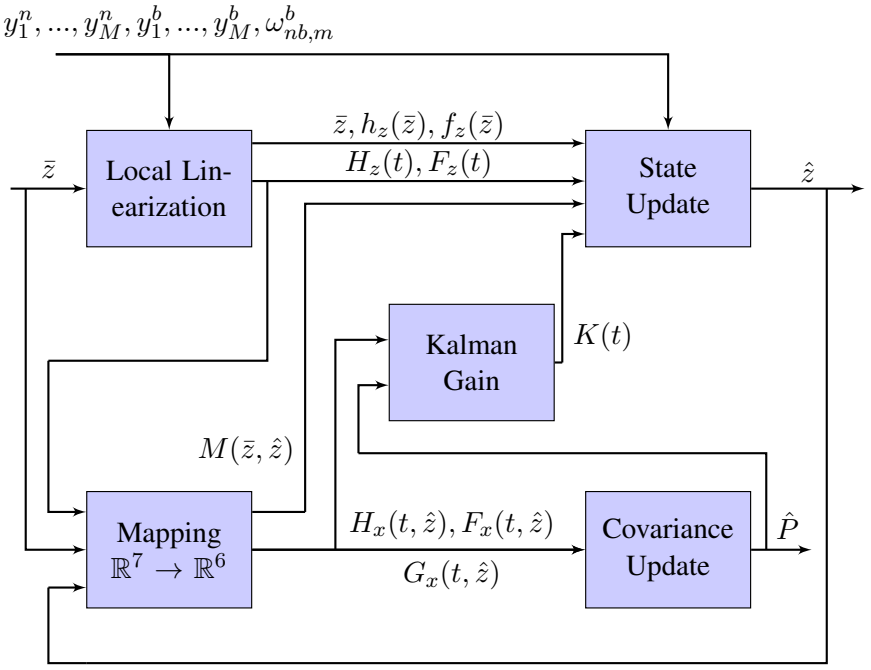

Figure 4.2: A closer look at the linearized KF part of the MXKF. The reset operation (4.20) is excluded for presentation purposes.

1. Define an update equation for $\hat{z}$ and formulate the seventh-order additive error dynamics

2. Derive a mapping between the seventh-order additive error (4.5) and the sixth-order multiplicative error (4.4)

3. Insert the mapping into the additive error dynamics to achieve a multiplicative error dynamics.

The internal structure of the linearized KF is shown in Figure 4.2.

4.3.1 Additive Model

Inserting the ARS measurement model (2.16) into the quaternion kinematics (2.8) allows us to write the full-state dynamic equation

$$\dot{q}_b^n = f_q(z,t) = \frac{1}{2}\Xi(q_b^n)(\omega_{nb,m}^b - b_{ars}^b - \epsilon_{ars}) \tag{4.8a}$$
$$= \frac{1}{2}\Omega(\omega_{nb,m}^b - b_{ars}^b - \epsilon_{ars})q_b^n$$
$$\dot{b}^b = f_b(t) = \epsilon_b \tag{4.8b}$$

which is expressed in the compact form

$$\dot{z} = f_z(z,t) = \begin{bmatrix} f_q(z,t) \\ f_b(t) \end{bmatrix}. \tag{4.9}$$

We define the process noise vector $\epsilon_z \triangleq [\epsilon_{ars}^\top, \epsilon_b^\top]^\top$.

The measurement equation is

$$y_i^b = h_i(z, y_i^n) = R^\top(q_b^n)y_i^n + \epsilon_{y,i}, \tag{4.10}$$

for vector measurements $i = 1, ..., M$, where $\epsilon_{y,i}$ is the noise on measurement i. We concatenate (4.10) for all i as

$$y^b = h(z, y^n) \tag{4.11}$$

$$y^b = \begin{bmatrix} y_1^b \\ \vdots \\ y_M^b \end{bmatrix},\ y^n = \begin{bmatrix} y_1^n \\ \vdots \\ y_M^n \end{bmatrix},\ \epsilon_y = \begin{bmatrix} \epsilon_{y,1} \\ \vdots \\ \epsilon_{y,M} \end{bmatrix},\ h(z,y^n) = \begin{bmatrix} h_1(z, y_1^n) \\ \vdots \\ h_M(z, y_M^n) \end{bmatrix}. \tag{4.12}$$

Additive Estimation Error Model

The models (4.9) and (4.11) are linearized about the exogenous signal $\bar{z}$

$$f_z(z,t) = f_z(\bar{z},t) + F_z(t)(z-\bar{z}) + G_z(t)\epsilon_z + \chi_z(t) \tag{4.13a}$$
$$h_z(z,t) = h_z(\bar{z},t) + H_z(t)(z-\bar{z}) + \epsilon_y + \chi_y(t), \tag{4.13b}$$

where $\chi_z(t)$ and $\chi_y(t)$ represent higher order terms of the linearizations. From (4.8), we find that $F_z(t)$ and $G_z(t)$ become

$$F_z(t) = \left.\frac{\mathrm{d}f_z(z,t)}{\mathrm{d}z}\right|_{z=\bar{z}} = \frac{1}{2}\begin{bmatrix} \Omega(\omega_{nb,m}^b - \bar{b}^{\bar{b}}) & -\Xi(q_{\bar{b}}^n) \\ 0_3 & 0_3 \end{bmatrix}$$
$$G_z(t) = \left.\frac{\mathrm{d}f_z(z,t)}{\mathrm{d}\epsilon_z}\right|_{z=\bar{z}} = \begin{bmatrix} -\frac{1}{2}\Xi(q_{\bar{b}}^n) & 0_{4\times 3} \\ 0_3 & I_3 \end{bmatrix}.$$

Using equation (A.44) from Markley and Crassidis [26], we find $H_z(\bar{z})$ to be

$$H_z(t) = \begin{bmatrix} 2S(y_1^{\bar{b}})\Xi^\top(q_{\bar{b}}^n) & 0_3 \\ \vdots & \\ 2S(y_M^{\bar{b}})\Xi^\top(q_{\bar{b}}^n) & 0_3 \end{bmatrix},$$

where $y_i^{\bar{b}} = R^\top(q_{\bar{b}}^n)y_i^n$. Notice that the dependency of known bounded time-varying signals have been replaced by dependency of time in $F_z(t)$, $G_z(t)$, $H_z(t)$, $\chi_z(t)$, and $\chi_y(t)$.

We define an estimator

$$\dot{\hat{z}} \triangleq f_z(\bar{z},t) + F_z(t)(\hat{z}-\bar{z}) + M(\bar{z},\hat{z})K(t)(y-\hat{y}) \tag{4.14a}$$

$$\hat{y} \triangleq h_z(\bar{z},t) + H_z(t)(\hat{z}-\bar{z}), \tag{4.14b}$$

where the gain matrix $K(t)$ and mapping matrix $M(\bar{z},\hat{z})$ are specified later.

Define $\tilde{y} \triangleq y - \hat{y}$. Now, subtracting (4.14) from (4.13) yields the additive estimation error model

$$\dot{\tilde{z}} = F_z(t)\tilde{z} - M(\bar{z},\hat{z})K(t)\tilde{y} + G_z(t)\epsilon_z + \chi_z(t) \tag{4.15a}$$

$$\tilde{y} = H_z(t)\tilde{z} + \epsilon_y + \chi_y(t). \tag{4.15b}$$

Inserting (4.15b) into (4.15a) yields the additive error dynamics

$$\begin{aligned} \hat{\Sigma}_A : \dot{\tilde{z}} = &\left(F_z(t) - M(\bar{z},\hat{z})K(t)H_z(t)\right)\tilde{z} + G_z(t)\epsilon_z \\ &+ \chi_z(t) - M(\bar{z},\hat{z})K(t)\left(\epsilon_y + \chi_y(t)\right). \end{aligned} \tag{4.16}$$

4.3.2 Mapping from Additive to Multiplicative Error

Lemma 4.3.1. *The additive error state $\tilde{z}$ can be mapped to the multiplicative error state δx by the mapping*

$$\tilde{z} = M(z,\hat{z})\delta x = (M(\bar{z},\hat{z}) + \tilde{M}(z,\bar{z}))\delta x, \tag{4.17}$$

where

$$M(\bar{z},\hat{z}) = \begin{bmatrix} \Psi(q_{\bar{b}}^n) + \Psi(q_{\hat{b}}^n) & 0_{4\times 3} \\ 0_3 & I_3 \end{bmatrix} \tag{4.18}$$

$$\tilde{M}(z,\bar{z}) = \begin{bmatrix} \Psi(q_b^{n\star}) - \Psi(q_{\bar{b}}^n) & 0_{4\times 3} \\ 0_3 & 0_3 \end{bmatrix}. \tag{4.19}$$

Moreover, the mapping approximation converges, i.e. $M(\bar{z},\hat{z}) \to M(z,\hat{z})$, as the NLO converges.

Proof. The proof is stated in Appendix 4.A. □

4.3.3 Multiplicative Model

In this section, we transform the error dynamics from $\mathbb{R}^7$ to $\mathbb{R}^6$. We begin by defining $\delta\check{q} = [\delta\check{\eta}; \delta\check{\varepsilon}] \triangleq (q_{\hat{b}}^n)^{-1} \otimes q_{\check{b}}^n$ and $\delta\bar{q} = [\delta\bar{\eta}; \delta\bar{\varepsilon}] \triangleq (q_{\hat{b}}^n)^{-1} \otimes q_{\bar{b}}^{n\star}$. Later, it will be required that $q_{\hat{b}}^n \neq -q_{\check{b}}^n$, and from (2.9) we must have $\delta\eta > -1$. Both are guaranteed by the following Lemma.

Lemma 4.3.2. *The reset rule*

$$\hat{z} \leftarrow \bar{z} \text{ if } {q_{\hat{b}}^n}^\top q_{\check{b}}^n \leq \epsilon \tag{4.20}$$

guarantees both that $q_{\hat{b}}^n \neq -q_{\check{b}}^n$ *and* $\delta\eta > -1 + \Delta(\epsilon)$ *where* $\Delta(\epsilon) > 0$ *for any input* $\epsilon > 0$.

Proof. The proof is stated in Appendix 4.B. □

Lemma 4.3.3. *The seventh order additive error dynamics* $\hat{\Sigma}_A$ *in* (4.16) *can be transformed by the approximate linear mapping* $M(\bar{z}, \hat{z})$ *to the sixth order multiplicative error dynamics*

$$\begin{aligned}\hat{\Sigma}_M : \delta\dot{x} =& (F_x(\hat{z}, t) - K(t)H_x(\hat{z}, t))\delta x + \chi_x(\hat{z}, t) \\ &+ G_x(\hat{z}, t)\epsilon_z - K(t)\epsilon_y + \zeta(\hat{z}, \delta x, t),\end{aligned} \tag{4.21}$$

where

$$F_x(\hat{z}, t) \triangleq M^\dagger(\bar{z}, \hat{z})(F_z(t)M(\bar{z}, \hat{z}) - \dot{M}(\bar{z}, \hat{z})) \tag{4.22a}$$
$$G_x(\hat{z}, t) \triangleq M^\dagger(\bar{z}, \hat{z})G_z(t) \tag{4.22b}$$
$$\chi_x(\hat{z}, t) \triangleq M^\dagger(\bar{z}, \hat{z})\chi_z(t) - K(t)\chi_y(t) \tag{4.22c}$$
$$H_x(\hat{z}, t) \triangleq H_z(t)M(\bar{z}, \hat{z}), \tag{4.22d}$$

and $(\cdot)^\dagger$ *denotes the Moore-Penrose pseudo-inverse operation* $C^\dagger = (C^\top C)^{-1}C^\top$. *Furthermore,*

$$\chi_x(\hat{z}, t) \leq k_\chi ||z - \bar{z}||_2^2 \tag{4.23a}$$
$$\zeta(\hat{z}, \delta x, t) \leq k_\zeta \|z - \bar{z}\|_2^2. \tag{4.23b}$$

Proof. The proof is stated in Appendix 4.C. □

In the following, explicit expressions for the matrices (4.22a), (4.22b), and (4.22d) are derived. From Markley and Crassidis [26] we have that

$$\frac{\mathrm{d}}{\mathrm{d}t}\Psi(q_{\hat{b}}^n) = \frac{1}{2}\Omega(\omega_{nb,m}^b - \hat{b}^{\hat{b}})\Psi(q_{\hat{b}}^n)$$

and similarly for $\Psi(q_{\bar{b}}^n)$. This is used in order to find

$$\begin{aligned}
F_x(\hat{z},t) &= \begin{bmatrix} F_1(\hat{z},t) & F_2(\hat{z},t) \\ 0_3 & 0_3 \end{bmatrix} \\
F_1(\hat{z},t) &= \frac{\Psi^\top(q_{\bar{b}}^n) + \Psi^\top(q_{\hat{b}}^n)}{4(1+\delta\check{\eta})}\Omega(\hat{b}^{\hat{b}} - \bar{b}^{\bar{b}})\Psi(q_{\hat{b}}^n) \\
F_2(\hat{z},t) &= -\frac{\Psi^\top(q_{\bar{b}}^n) + \Psi^\top(q_{\hat{b}}^n)}{4(1+\delta\check{\eta})}\Xi(q_{\bar{b}}^n) = -\frac{1}{4}D_1(\hat{z},t)R(q_{\bar{b}}^n).
\end{aligned}$$

Here, $\Psi^\top(q_{\bar{b}}^n)\Xi(q_{\bar{b}}^n) = R(q_{\bar{b}}^n)$, $\Xi(q_{\bar{b}}^n) = \Psi(q_{\bar{b}}^n)R(q_{\bar{b}}^n)$, and $\Psi^\top(q_{\hat{b}}^n)\Psi(q_{\bar{b}}^n) = I_3\delta\check{\eta} - S(\delta\check{\varepsilon})$ have been used to find the useful identities

$$\begin{aligned}
&(\Psi^\top(q_{\bar{b}}^n) + \Psi^\top(q_{\hat{b}}^n))\Xi(q_{\bar{b}}^n) = D(\hat{z},t)R(q_{\bar{b}}^n) \\
&D(\hat{z},t) = (1+\delta\check{\eta})I_3 - S(\delta\check{\varepsilon}) \\
&D_1(\hat{z},t) = \frac{1}{1+\delta\check{\eta}}D(\hat{z},t) = I_3 - S(\delta\check{u}),
\end{aligned}$$

where $\delta\check{u} = \delta\check{\varepsilon}/(1+\delta\check{\eta})$. $G_x(\hat{z},t)$ and $H_x(\hat{z},t)$ are found to be

$$\begin{aligned}
G_x(\hat{z},t) &= \begin{bmatrix} -\frac{1}{4}D_1(\hat{z},t)R(q_{\bar{b}}^n) & 0_{4\times 3} \\ 0_3 & I_3 \end{bmatrix} \\
H_x(\hat{z},t) &= \begin{bmatrix} 2R^\top(q_{\bar{b}}^n)S(y_1^n)D^\top(\hat{z},t) & 0_3 \\ \vdots & \vdots \\ 2R^\top(q_{\bar{b}}^n)S(y_M^n)D^\top(\hat{z},t) & 0_3 \end{bmatrix}
\end{aligned}$$

and $S(y_i^{\bar{b}}) = S(R^\top(q_{\bar{b}}^n)y_i^n) = R^\top(q_{\bar{b}}^n)S(y_i^n)R(q_{\bar{b}}^n)$ has been used to find $H_x(\hat{z},t)$.

$K(t)$ introduced in (4.14a) is found by (1.3b)–(1.3c) inserted $F_x(\hat{z},t)$, $H_x(\hat{z},t)$, $G_x(\hat{z},t)$, $\mathcal{Q}(t) = \mathrm{E}(\epsilon_z\epsilon_z^\top)$, and $\mathcal{R}(t) = \mathrm{E}(\epsilon_y\epsilon_y^\top)$, where $P(t)$ is the covariance estimate with initial value $P(0) = P_0$.

4.4 Stability Analysis

Lemma 4.4.1. *The pair $(F_x(\hat{z},t), H_x(\hat{z},t))$ is uniformly completely observable (UCO) and $(F_x(\hat{z},t), G_x(\hat{z},t))$ is uniformly completely controllable (UCC).*

Proof. The proof is stated in Appendix 4.D □

Proposition 4.4.1. *Consider the estimator defined by* (4.7), (4.14), *and* (4.20), *and assume* $\epsilon_z = 0$, $\epsilon_y = 0$. *The equilibrium points* $R(q_b^n) - \bar{R}_{\bar{b}}^n = 0_3$, $b^b - \bar{b}^{\bar{b}} = 0$, *and* $\delta x = 0$ *of the cascaded error dynamics* $\bar{\Sigma}$–$\hat{\Sigma}_M$ *is GES for positive definite symmetric matrices* P_0, $\mathcal{Q}$, *and* $\mathcal{R}$. *Consequently, the equilibrium point* $\tilde{z} = 0$ *is GES.*

Proof. The proof is stated in Appendix 4.E □

4.5 Results and Discussion

Both the MXKF and MEKF discussed hereafter are implemented as discrete time KFs. The discrete-time implementation of the MXKF is given in Table 4.1. c2d()

Table 4.1: Discrete implementation of the MXKF. a_k^- and a_k^+ denote a priori and a posteriori values of a at time instance t_k, respectively.

Initialisation

Determine $\bar{R}_{\bar{b}}^n(0)$, $q_{\bar{b}}^n(0)$, $\bar{b}^{\bar{b}}(0)$, $\hat{b}^{\hat{b}}(0)$, P_0

$0 < \epsilon \ll 1$

Measurement update

$$\hat{z}^- \leftarrow \bar{z} \text{ if } q_{\hat{b}}^{n-\top} q_{\bar{b}}^n < \epsilon$$

$$\hat{z}_k^+ = \hat{z}_k^- + \bar{M}(t_k, \hat{z}_k^-) K_k (y_k - \hat{y}_k)$$

$$\hat{y}_k = h_z(\bar{z}_k) + H_z(t_k)(\hat{z}_k^- - \bar{z}_k))$$

$$P_k^+ = (I_6 - K_k H_{x,k}) P_k^- (I_6 - K_k H_{x,k})^\top + K_k \mathcal{R} K_k^\top$$

$$K_k = P_k^- H_{x,k}^\top (H_{x,k} P_k^- H_{x,k}^\top + \mathcal{R})^{-1}$$

$$H_{x,k} = \begin{bmatrix} 2R^\top(q_{\bar{b},k}^n) S(y_{1,k}^n) D^\top(t_k, \hat{z}_k^-) & 0_3 \\ \vdots & \vdots \\ 2R^\top(q_{\bar{b},k}^n) S(y_{\bar{M},k}^n) D^\top(t_k, \hat{z}_k^-) & 0_3 \end{bmatrix}$$

Time update

$$\hat{z}_{k+1}^- = \hat{z}_k^+ + \Delta t_k (f_z(t_k, \bar{z}_k) + F_z(t_k)(\hat{z}_k^+ - \bar{z}_k))$$

$$P_{k+1}^- = \Phi(t_k) P_k^+ \Phi^\top(t_k) + \Gamma(t_k) \mathcal{Q} \Gamma^\top(t_k)$$

$$[\Phi(t_k), \Gamma(t_k)] = \text{c2d}(F_x(t_k, \hat{z}_k^+), G_x(t_k, \hat{z}_k^+), \Delta t_k)$$

Table 4.2: The number of scalar addition (A.), multiplication (M.), division (D.) subtraction (S.), and square root (Sq.) operations performed in one time and measurement update of each estimator in their respective implementations. Available normalized measurements have been assumed here.

	A.+S.	M.	D.	Sq.
NLO	149	220	12	4
MXKF^2	1998	2542	38	2
MEKF^2	1736	2204	30	2
NLO+MXKF^2	2147	2762	50	6

is a function that finds the discretized system matrices $\Phi(t_k)$ and $\Gamma(t_k)$ from the continuous system matrices $F_x(t_k, \hat{z}_k^+)$ and $G_x(t_k, \hat{z}_k^+)$ given the step length $\Delta t_k = t_{k+1} - t_k$.

The small angle approximation commonly used in the development of the MEKF is not used for the MXKF. Instead, the XKF method ensures that all linearization errors vanish as the NLO converges, yielding a global stability result. However, this also increases the computational burden of the algorithm, as F_x, G_x, and H_x become more complex to compute and an NLO is needed. Table 4.2 shows an increase of approximately 25% in computational complexity when using the MXKF linearized about the estimate from an NLO relative to the MEKF.

The linearization point provided by the NLO is used directly in the MXKF design. Thus, the uncertainty of a noisy linearization point is neglected. If the noise on the NLO estimate is large, it might be beneficial to account for the added uncertainty of the noisy linearization point by scaling of $\mathcal{Q}$ and $\mathcal{R}$ or adding appropriate noise terms in the model. This is an interesting topic in the design of XKFs generally, but outside the scope of this thesis.

In the following comparison study, four estimators are included: an aggressively tuned NLO (denoted $\overline{\text{NLO}}$), a conservatively tuned NLO, an MXKF, and a standard MEKF using the MRP formulation. The aggressively tuned NLO serves as a linearization point with fast convergence and the conservatively tuned NLO is included to provide a fair comparison of steady-state performance.

Euler angle errors are used to calculate MAE values and display attitude error trajectories. These have been found by extracting the Euler angles from $(q_b^n)^{-1} \otimes q_b^n$, where q_b^n is a placeholder for the NLO, MXKF, and MEKF estimates.

The simulated scenario is a rotating vehicle with no translative motion. Accelerometer and magnetometer measurements, $f^b_{nb,m}$ and m^b_m respectively, form vector pairs with the NED counterparts

$$-g^n = \begin{bmatrix} 0 \\ 0 \\ -9.818 \end{bmatrix}, \; m^n = \begin{bmatrix} 0.3197 \\ 0 \\ 0.6926 \end{bmatrix},$$

respectively. We define

$$y^n_1 \triangleq \frac{-g^n}{\|g^n\|_2}, \; y^b_1 \triangleq \frac{f^b_{nb,m}}{\|f^b_{nb,m}\|_2}, \; y^n_2 \triangleq \frac{m^n}{\|m^n\|_2}, \; y^b_2 \triangleq \frac{m^b_m}{\|m^b_m\|_2}$$

which are related by $y^b_1 = R^\top(q^n_b)y^n_1 + \epsilon_1$ and $y^b_2 = R^\top(q^n_b)y^n_2 + \epsilon_2$. The noise $\epsilon_1 = [\epsilon_{1x}, \epsilon_{1y}, \epsilon_{1z}]^\top$ and $\epsilon_2 = [\epsilon_{2x}, \epsilon_{2y}, \epsilon_{2z}]^\top$ consist of white noise terms $\epsilon_{1w} \sim \mathcal{N}(0, \sigma_1^2)$ and $\epsilon_{2w} \sim \mathcal{N}(0, \sigma_2^2)$ for $w \in \{x, y, z\}$.

100 different 600 seconds long scenarios have been simulated. The same attitude trajectory was used in all simulations, which was generated by

$$\omega^b_{nb}(t) = \begin{bmatrix} -0.1\cos(0.15t) \\ 0.1\sin(0.10t) \\ -0.1\cos(0.05t) \end{bmatrix}, q^n_b(0) = \begin{bmatrix} 1 \\ 0 \\ 0 \\ 0 \end{bmatrix}.$$

Furthermore,

$$b^b_{ars} = \begin{bmatrix} 0.012 \\ -0.021 \\ 0.014 \end{bmatrix} \frac{\text{rad}}{\text{s}}, \; \bar{b}^{\bar{b}}_{ars}(0) = \hat{b}^{\hat{b}}_{ars}(0) = \begin{bmatrix} 0 \\ 0 \\ 0 \end{bmatrix} \frac{\text{rad}}{\text{s}},$$

$\sigma_1 = 2 \cdot 10^{-3}$, $\sigma_2 = 4 \cdot 10^{-3}$, and $\sigma_\omega = 10^{-3}$rad/s. The NLO tuning parameters were set to $K_p = 10$, $k_I = 0.02$, and $\sigma = 1$ for the aggressively tuned one and $K_p = 1.5$, $k_I = 0.02$, and $\sigma = 1$ for the conservatively tuned one. For the MXKF and MEKF, the true values of σ_1, σ_2, and σ_ω were used in addition to $\sigma_b = 10^{-4}$, and the initial covariance matrix was $P(0) = \text{blockdiag}(I_3, I_3 \cdot 10^{-7})$, where blockdiag$(\cdot)$ forms a block diagonal matrix of its inputs. The estimators were given the same initial estimate of attitude and bias in each simulation, and the initial attitude was randomly drawn from a uniform distribution between -180° and 180°. Both the IMU and estimators were updated with 100Hz.

Table 4.3: MAE values describing the steady-state performance of the estimators.

	Roll (deg)	Pitch (deg)	Yaw (deg)
$\overline{\text{NLO}}$	0.029	0.032	0.147
NLO	0.021	0.026	0.073
MXKF	0.007	0.007	0.021
MEKF	0.007	0.007	0.022

In Table 4.3 and 4.4, the MAE values representing the steady-state and transient behaviors of the attitude estimators are shown, respectively. The steady-state MAE values are calculated from the last 300 seconds of the attitude error trajectories, whereas the transient MAE values are calculated from the first 200 seconds. In Figure 4.3, the bias error trajectories for each estimator averaged over all scenarios are shown.

The aggressively tuned NLO can be seen to achieve significantly improved transient performance relative to the conservatively tuned NLO without a similar deterioration of steady-state performance. The largest performance decrease can be seen in yaw. This is because there is relatively little information about yaw in the measurements as all of g^n and most of m^n are vertical components, and thus, noise sensitivity increases. Still, the performance difference is small enough to not affect the performance of the MXKF, which is apparent from the identical steady-state MAE values of the MXKF and the MEKF. This makes the NLO of Grip et al. [52] a suitable auxiliary estimator in the MXKF.

The improved transient performance of the aggressively tuned NLO is seen to yield significantly better transient performance of the MXKF than of the MEKF. Combined with the identical steady-state performance of the MXKF and MEKF, this is an important result. It shows that the tuning of the MXKF w.r.t. transient and steady-state performance can be decoupled; tune the NLO for fast convergence and the linearized KF for steady-state performance.

The MXKF and MEKF inherit the near-optimality of the linearized KF, which from Table 4.3 can be seen to yield significantly better steady-state performance than the NLOs. Also, with the linearized KF, the reference vector measurements are used directly and their noises are tuned for individually. The NLO, on the other hand, calculates (4.7c) and does not offer as intuitive tuning w.r.t. measurement noise.

The experiments were conducted in the MCLab at NTNU, which contains a wa-

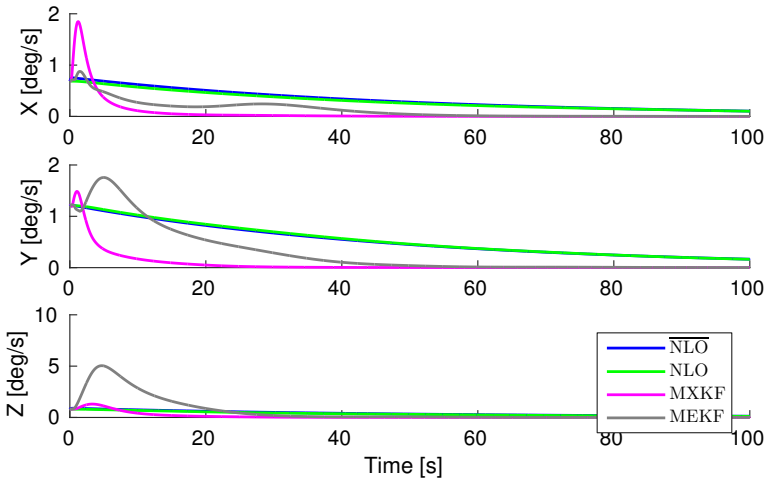

Figure 4.3: The 100 first seconds of the ARS bias estimation errors averaged over the 100 simulations.

Table 4.4: MAE values describing the transient performance of the estimators.

	Roll (deg)	Pitch (deg)	Yaw (deg)
$\overline{\text{NLO}}$	0.065	0.062	0.174
NLO	0.410	0.161	0.583
MXKF	0.065	0.051	0.323
MEKF	0.173	0.092	1.357

ter tank for experimental testing described in Section 3.1. The IMU used in the experiments was an Xsens MTi-3, set up to deliver accelerometer, ARS, and magnetometer measurements at 25 Hz, the same rate with which the estimators were updated. IMU calibration yielded the values of g^n, m^n, σ_1, σ_2, and σ_{ars} used in the simulations, which are also used here. The tuning of the estimators in the experiments were identical to the tuning in the

The experimental data is primarily meant to verify that the estimators work in practice, as seen in Figure 4.4–4.6, and not to provide a qualitative comparison of the estimators. It is still interesting to see that the MAE values of the MXKF and MEKF are lower than that of the NLOs, and that the MXKF does not seem to suffer greatly from a less accurate linearization point. This confirms the conclusions drawn from the simulations study.

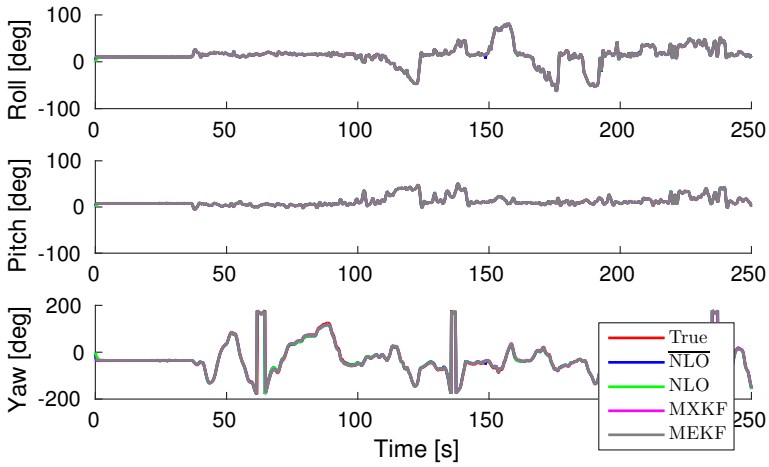

Figure 4.4: This figure shows the true and estimated attitude trajectories from Qualisys (as "True") and NLO, MXKF, and MEKF, respectively.

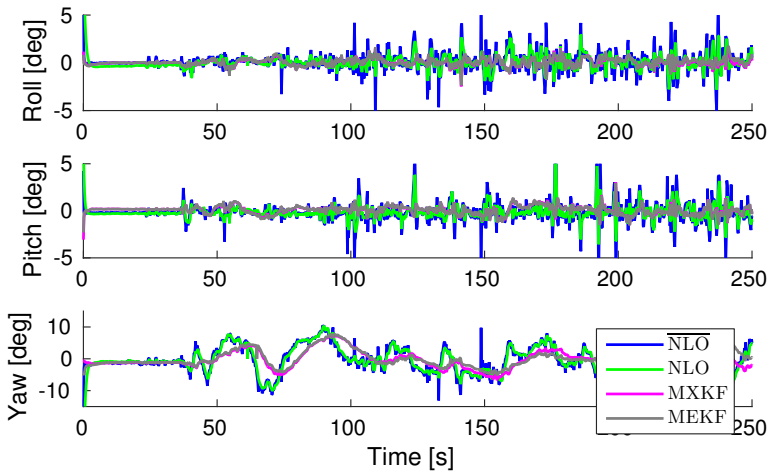

Figure 4.5: This figure shows the attitude error trajectories of the estimators, where the Qualisys attitude trajectory was used as truth reference.

Table 4.5: MAE values calculated from 50 seconds to the end of the experiments.

	Roll (deg)	Pitch (deg)	Yaw (deg)
$\overline{\text{NLO}}$	0.705	0.714	4.276
NLO	0.484	0.497	4.109
MXKF	0.311	0.407	3.023
MEKF	0.330	0.417	2.748

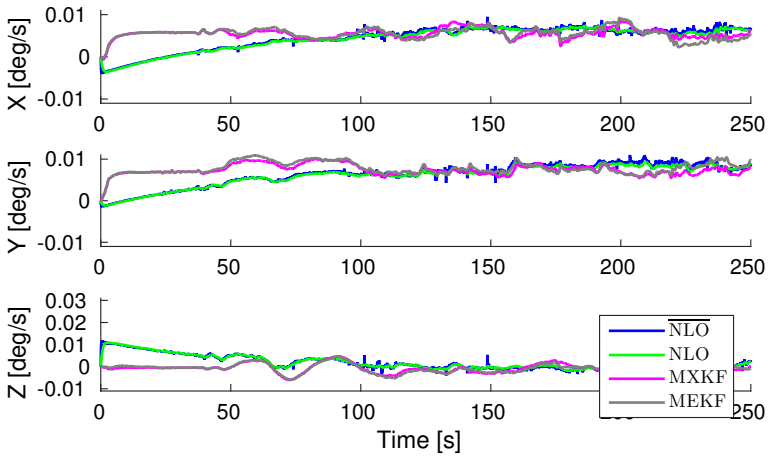

Figure 4.6: The bias estimates from experimental data.

4.6 Conclusion and Future Work

In this chapter, the MXKF was developed and shown to be GES. Furthermore, it was shown both in simulations and experimentally to have identical steady-state performance as, and better transient performance than, the MEKF with identical tuning. This is a significant result, as it is the first KF-based attitude and ARS bias estimator using a minimal state representation with proven global stability and MEKF-like performance.

This chapter aimed at answering the research question "*Can the XKF method be applied to attitude estimation to yield a filter with similar performance as the MEKF, but with global stability?*". This chapter has positively shown that it can.

Further work should include developing an MXKF in which the resetting of the state estimate is not needed. This may require using another state representation, or simply a smarter proof of the MXKF developed here.

Appendix

4.A Proof of Lemma 4.3.1

In order to verify the mapping $\tilde{z} = M(z, \hat{z})\delta x$, we insert (4.4) in (4.5) twice to get $\tilde{q} = q_b^{n\star} - q_{\hat{b}}^n = q_{\hat{b}}^n \otimes \delta q - q_b^{n\star} \otimes (\delta q)^{-1}$. Further, we apply (2.6) twice to get

$$\begin{aligned} \tilde{q} &= q_{\hat{b}}^n \delta\eta + \Psi(q_{\hat{b}}^n)\delta\varepsilon - q_b^{n\star}\delta\eta + \Psi(q_b^{n\star})\delta\varepsilon \\ (1+\delta\eta)\tilde{q} &= (\Psi(q_{\hat{b}}^n) + \Psi(q_b^{n\star}))\delta\varepsilon \\ \tilde{q} &= (\Psi(q_{\hat{b}}^n) + \Psi(q_b^{n\star}))\delta u \end{aligned}$$

Noticing that $\tilde{q} = (\Psi(q_{\hat{b}}^n + q_{\tilde{b}}^n) + \Psi(q_b^{n\star} - q_{\tilde{b}}^n))\delta u$ verifies the mapping using (4.17) and (4.19). From Proposition 4.2.1, we know that $R(q_b^n) - R(q_{\tilde{b}}^n) \to 0$, which together with (4.2) means that $q_{\tilde{b}}^n \to q_b^{n\star}$. This proves that $\tilde{M}(z, \bar{z}) \to 0$ exponentially.

4.B Proof of Lemma 4.3.2

From $\delta q = \delta\check{q} \otimes \delta\bar{q}$, we get $\delta\eta = \delta\bar{\eta}\delta\check{\eta} - \delta\bar{\varepsilon}^\top\delta\check{\varepsilon}$. From (4.2), we have that $\delta\bar{\eta} \geq 0$, while (4.20) ensures that $\delta\check{\eta} > \epsilon$. Therefore, $\delta\bar{\eta}\delta\check{\eta} > 0$.

Using $\|\delta\bar{\varepsilon}\|_2 \leq 1$ and $\|\delta\check{\varepsilon}\|_2 = \sqrt{1-\epsilon^2} \leq 1 - \Delta(\epsilon)$, we show

$$\begin{aligned} \delta\eta &\geq -\delta\bar{\varepsilon}^\top\delta\check{\varepsilon} \\ &\geq -\|\delta\bar{\varepsilon}\|_2\|\delta\check{\varepsilon}\|_2 \\ &\geq -\sqrt{1-\epsilon^2} \geq -1 + \Delta(\epsilon) \end{aligned}$$

which concludes the proof.

4.C Proof of Lemma 4.3.3

Differentiating (4.17) w.r.t. time yields

$$\begin{aligned}\dot{\tilde{z}} =&\dot{M}(\bar{z},\hat{z})\delta x + M(\bar{z},\hat{z})\delta\dot{x} + \dot{\tilde{M}}(z,\bar{z},t)\delta x + \tilde{M}(z,\bar{z})\delta\dot{x}\\ \delta\dot{x} =&M^{\dagger}(\bar{z},\hat{z})(\dot{\tilde{z}} - \dot{M}(\bar{z},\hat{z})\delta x - \dot{\tilde{M}}(z,\bar{z},t)\delta x - \tilde{M}(z,\bar{z})\delta\dot{x})\end{aligned}$$

Defining $M_1 \triangleq M_1(\hat{z},t) = I_3 + M^{\dagger}(\bar{z},\hat{z})\tilde{M}(z,\bar{z})$ and collecting $\delta\dot{x}$ yields

$$\delta\dot{x} = M_1^{-1}M^{\dagger}(\bar{z},\hat{z})\left(\dot{\tilde{z}} - \dot{M}(\bar{z},\hat{z})\delta x - \dot{\tilde{M}}(z,\bar{z},t)\delta x\right). \tag{4.24}$$

It is straight-forward to show that

$$\det(M_1) = \frac{1+\delta\eta+\delta\bar{\eta}+\delta\check{\eta}}{2(1+\delta\check{\eta})}\det\left(I_3 + \frac{S(\delta\varepsilon+\delta\bar{\varepsilon}+\delta\check{\varepsilon}))}{(1+\delta\eta+\delta\bar{\eta}+\delta\check{\eta})}\right).$$

Since

- $\delta\check{\eta} > \epsilon > -1$
- $1+\delta\eta+\delta\bar{\eta}+\delta\check{\eta} > \epsilon + \Delta(\epsilon)$
- $x^{\top}(I_3+A)x = x^{\top}x > 0 \;\forall\; x \neq 0$ for any skew-symmetric matrix A,

then $\det(M_1) \neq 0$ which means that M_1 is invertible. By the Sherman-Morrison-Woodbury formula [75], we have that

$$\begin{aligned}M_1^{-1} &= I_3 - M_2\\ M_2 \triangleq M_2(\hat{z},t) &= (I_3 + M^{\dagger}(\bar{z},\hat{z})\tilde{M}(z,\bar{z}))^{-1}M^{\dagger}(\bar{z},\hat{z})\tilde{M}(z,\bar{z})\end{aligned}$$

Now, inserting (4.22) and expanding M_1^{-1} in (4.24), it can be rewritten as

$$\begin{aligned}\delta\dot{x} =&(I_3 - M_2)\Big((F_x(\hat{z},t) - K(t)H_x(\hat{z},t))\delta x + \chi_x(\hat{z},t)\\ &+ G_x(\hat{z},t)\epsilon_z - K(t)\epsilon_y - \dot{\tilde{M}}(z,\bar{z},t)\delta x\Big)\\ \delta\dot{x} =&(F_x(\hat{z},t) - K(t)H_x(\hat{z},t))\delta x + \chi_x(\hat{z},t)\\ &+ G_x(\hat{z},t)\epsilon_z - K(t)\epsilon_y + \zeta(\hat{z},\delta x,t)\end{aligned}$$

where $\zeta(\hat{z}, \delta x, t) \triangleq -M_2((F_x(\hat{z}, t) - K(t)H_x(\hat{z}, t))\delta x + \chi_x(\hat{z}, t) + G_x(\hat{z}, t)\epsilon_z - K(t)\epsilon_y) - M_1^{-1}\dot{M}(z, \bar{z}, t)\delta x$. Using that $\Psi^\top(q_{\hat{b}}^n)\Psi(q_{\hat{b}}^n) = I_3\delta\check{\eta} - S(\delta\check{\varepsilon})$, we find

$$(M^\top(\bar{z}, \hat{z})M(\bar{z}, \hat{z}))^{-1} = \begin{bmatrix} \frac{1}{2(1+\delta\check{\eta})}I_3 & 0 \\ 0 & I_3 \end{bmatrix} \tag{4.25}$$

and we see that $M^\dagger(\bar{z}, \hat{z})$ exists whenever $\delta\check{\eta} = q_{\hat{b}}^{n\top} q_{\bar{b}}^n \neq -1$, i.e., when $q_{\hat{b}}^n \neq -q_{\bar{b}}^n$, which is guaranteed by Lemma 4.3.2.

Due to the boundedness of $\bar{z}$ and $q_{\hat{b}}^n$ and the smoothness of f_z, h_z, G_z, and $\tilde{M}$, there exist constants $k_\zeta, k_\chi > 0$ such that $\chi_x(\hat{z}, t) < k_\chi||z - \bar{z}||_2^2$, $\zeta(\hat{z}, \delta x, t) < k_\zeta\|z - \bar{z}\|_2^2$.

4.D Proof of Lemma 4.4.1

First, we show UCO of the pair $(F_x(\hat{z}, t), H_x(\hat{z}, t))$. Generally, in order to show UCO of the time-varying pair $(A(t), D(t))$, we form the observability co-distribution

$$\mathrm{d}\mathcal{O}(t) = \begin{bmatrix} \mathrm{d}\mathcal{O}_0(t) \\ \vdots \\ \mathrm{d}\mathcal{O}_N(t) \end{bmatrix} \tag{4.26a}$$

$$\mathrm{d}\mathcal{O}_0(t) = D(t) \tag{4.26b}$$

$$\mathrm{d}\mathcal{O}_n(t) = \mathrm{d}\dot{\mathcal{O}}_{n-1}(t) + \mathrm{d}\mathcal{O}(t)A(t),\ n = (1, ..., N), \tag{4.26c}$$

where N is the dimension of the state space, i.e. $A(t) \in \mathbb{R}^{N\times N}$. From Theorem 6.O12 of Chen [76], we know that $(A(t), D(t))$ is UCO if and only if $\mathrm{rank}(\mathcal{O}) = N$.

Now, since both $H_x(\hat{z}, t)$ and $F_x(\hat{z}, t)$ are continuously differentiable, $\mathrm{d}\mathcal{O}$ can be formed. It suffices to examine only

$$\begin{bmatrix} \mathrm{d}\mathcal{O}_0(t) \\ \mathrm{d}\mathcal{O}_1(t) \end{bmatrix} = \begin{bmatrix} \mathcal{O}_1 & 0_{3M\times 3} \\ \mathcal{O}_2 & \mathcal{O}_3 \end{bmatrix},$$

because if it has full column rank, $\mathrm{d}\mathcal{O}$ must have full rank. Here, where M is the number of reference vector measurements. Furthermore, as proven by Meyer [77], it suffices to prove full rank of $\mathcal{O}_1$ and $\mathcal{O}_3$, for if they both have full rank, the whole

block triangular matrix has full rank. They are found to be

$$\mathcal{O}_1 = 2(1+\delta\check{\eta})R^\top(q_b^n)S_{1:M}D_1^\top(\hat{z},t)$$
$$\mathcal{O}_3 = -\frac{1+\delta\check{\eta}}{2}R^\top(q_b^n)S_{1:M}D_1^\top(\hat{z},t)D_1(\hat{z},t)R(q_b^n),$$

where

$$S_{1:M} = \begin{bmatrix} S(y_1^n) \\ \vdots \\ S(y_M^n) \end{bmatrix}.$$

Through the well known identity

$$\text{rank}(\mathcal{O}) = \text{rank}(\mathcal{O}^\top\mathcal{O})$$

for any matrix $\mathcal{O}$, we examine the ranks of $\mathcal{O}_1$ and $\mathcal{O}_3$:

$$\text{rank}(\mathcal{O}_1) = \text{rank}\Big(-4(1+\delta\check{\eta})^2 D_1(\hat{z},t)S_{1:M}^\top S_{1:M}D_1^\top(\hat{z},t)\Big)$$
$$\text{rank}(\mathcal{O}_3) = \text{rank}\Big(-\frac{(1+\delta\check{\eta})^2}{4}R^\top(q_b^n)D_1^\top(\hat{z},t)D_1(\hat{z},t) S_{1:M}^\top S_{1:M}D_1^\top(\hat{z},t)D_1(\hat{z},t)R(q_b^n)\Big).$$

The determinant of $D_1(\hat{z},t)$ is $\det(D_1(\hat{z},t)) = 1 + \delta\check{u}^\top\delta\check{u} > 0$, meaning that $D_1(\hat{z},t)$ always has full rank. Under Assumption 4.1.1, $S_{1:M}^\top S_{1:M} = \sum_{j=1}^M S^2(y_j^n)$ also has full rank. Since the product of square full rank matrices has full rank and $\delta\check{\eta} > \epsilon$ as guaranteed by (4.20), we know that both $\mathcal{O}_1$ and $\mathcal{O}_3$ has full rank. Therefore, we know that observability co-distribution as full rank and thus, $(F_x(\hat{z},t), H_x(\hat{z},t))$ is UCO.

In order to show that the time-varying pair $(A(t), G(t))$ is UCC, we show full rank of the controllability co-distribution

$$\mathrm{d}\mathcal{C}(t) = \begin{bmatrix}\mathrm{d}\mathcal{C}_0(t) & \cdots & \mathrm{d}\mathcal{C}_N(t)\end{bmatrix} \tag{4.27a}$$
$$\mathrm{d}\mathcal{C}_0(t) = G(t) \tag{4.27b}$$
$$\mathrm{d}\mathcal{C}_n(t) = \mathrm{d}\dot{\mathcal{C}}_{n-1}(t) + A(t)\mathrm{d}\mathcal{C}_{n-1}(t) \tag{4.27c}$$

Since $F_x(\hat{z},t)$ and $G_x(\hat{z},t)$ are continuously differentiable and $\text{rank}(G_x(\hat{z},t)) = 6$, we have shown that $(F_x(\hat{z},t), G_x(\hat{z},t))$ is UCC.

4.E Proof of Proposition 4.4.1

First we examine the case when no resets of the form (4.20) occur. Under Proposition 4.2.1, Lemma 4.4.1, (4.23), and choosing $\mathcal{Q}$, $\mathcal{R}$, and $P(0)$ to be symmetric and positive definite, Theorem 2.1 of Johansen and Fossen [8] proves that the origin $R(q_b^n) - R_{\bar{b}}^n = 0$, $b^b - \bar{b}^{\bar{b}} = 0$, and $\delta x = 0$ of the cascaded error dynamics Σ_1–Σ_2 is GES.

If resets occur, it is sufficient to prove that there will only be a finite number of them, after the last of which the above result will be true.

There exists a threshold ξ_1 such that when $\delta\bar{u} < \xi_1$, there exists a $\xi_2(\|\delta\bar{u}\|_2)$ such that if $\|\delta u\|_2 < \xi_2(\|\delta\bar{u}\|_2)$, no resets can occur. That such a threshold exists is apparent when $\|\delta\bar{u}\|_2 = 0 \Rightarrow \delta u = \delta\check{u}$, and $\|\delta u\|_2^2 \geq (1-\epsilon)/(1+\epsilon)$ in order for a reset to occur. Therefore, $\xi_2(0) = (1-\epsilon)/(1+\epsilon)$ and $\xi_2(\|\delta\bar{u}\|_2) > 0 \ \forall \ \|\delta\bar{u}\|_2 < \xi_1$. Let resets occur at times $t_k, k = 0, 1, ...$ where $k = 0$ is the index of initialization and $k > 0$ are the indices of resets. By Theorem 4.14 in [6], we have between resets for the GES error dynamics Σ_1–Σ_2 that $c_1\|\delta x(t)\|_2^2 \leq V(\delta x(t)) \leq c_2\|\delta x(t)\|_2^2$ and $\dot{V}(\delta x(t), t) \leq -c_3\|\delta x(t)\|_2^2$. From the latter and $-V(\delta x(t))/c_2 \geq -\|\delta x(t)\|_2^2$ we find

$$\begin{aligned}
\int \frac{\mathrm{d}V(\delta x(t))}{V(\delta x(t))} &\leq \int -\frac{c_3}{c_2}\mathrm{d}t \\
V(\delta x(t)) &\leq V(\delta x(t_k))e^{-\frac{c_3}{c_2}(t-t_k)} \\
\|\delta x(t)\|_2 &\leq c\|\delta x(t_k)\|_2 e^{-\frac{c_3}{2c_2}(t-t_k)}
\end{aligned}$$

where $c = \sqrt{c_2/c_1}$. Since c_1 and c_2 always can be chosen strictly positive and bounded, respectively, c always exists and is bounded. In order to prove that the number of resets is finite, we explore the claim about an infinite number of resets. Since $\|\delta\bar{x}\|_2$ is exponentially decaying, there must then come a k such that $\|\delta\bar{x}(t_k)\|_2 = \|\delta x(t_k)\|_2 \leq \xi_2(\|\delta\bar{x}(t)\|_2)/c$. Since $c \geq 1$, this means that $\|\delta x(t_k)\|_2 \leq \xi_2(\|\delta\bar{x}(t)\|_2)$, and clearly, the last reset has occured. The claim is therefore false, and only a finite number of resets can occur. Consequently, $\delta x \to 0$ exponentially.

Since $\|\delta u\|_2 = 0 \Rightarrow \delta q = [1, 0, 0, 0]^\top$ and $q_{\hat{b}}^n = q_b^{n\star} \otimes (\delta q)^{-1}$, we know that $\|\delta u\|_2 \to 0$ implies $q_{\hat{b}}^n \to q_b^{n\star}$, and consequently, that $\|\delta x\|_2 \to 0$ implies $\|\tilde{z}\|_2 \to 0$. This concludes the proof.

Chapter 5

Position, Velocity, and Wave Speed Estimation Using a Long Baseline Network

This chapter is based on the work of Stovner et al. [68]. Here, a 3SF for position, velocity, and wave speed estimation using an LBL network is developed. The AT of the 3SF is an adaptation of the explicit formulas of Bancroft [57] and Chaffee and Abel [58] for an additive error term to the multiplicative error factor that is the unknown wave speed factor. This estimation problem was studied by Batista [63], where a different solution using state augmentation to handle the nonlinearities was used. Contrary to Stovner et al. [68], range-rate measurements are not considered in this chapter.

The main contributions of this chapter are the transformation of the nonlinear measurement equation with a multiplicative bias term to a linear measurement model and the development of a filter with GES error dynamics. This is the work done in Stovner et al. [68]. The low disparity between transponder positions along the vertical axis typically present in LBL networks yield low accuracy in that dimension. Therefore, a slightly altered filter is presented in this chapter as well, where depth measurements are used in the AT to improve accuracy. This also lowers the numbers of transponders required from 4 to 3. The new filter is additionally shown to perform better than that of Stovner et al. [68].

The structure of the 3SF developed in this chapter is seen in Figure 5.1. Trough

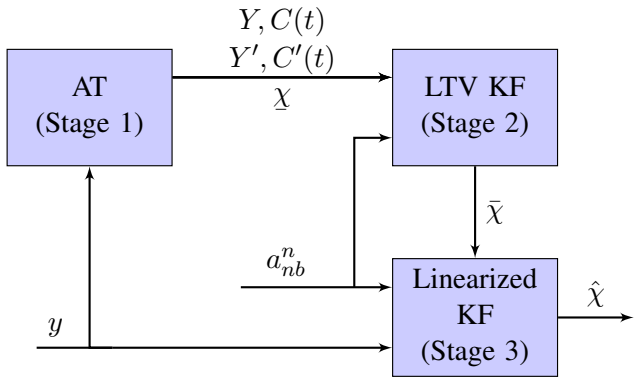

Figure 5.1: Block diagram showing the 3SF.

Section 5.1–5.3, the three stages are derived. First, the state and relevant measurement equations are defined.

The true state and its second and third stage estimates are given by

$$\chi = \begin{bmatrix} p^n_{nb} \\ \beta \\ v^n_{nb} \end{bmatrix}, \ \bar{\chi} = \begin{bmatrix} \bar{p}^n_{nb} \\ \bar{\beta} \\ \bar{v}^n_{nb} \end{bmatrix}, \ \hat{\chi} = \begin{bmatrix} \hat{p}^n_{nb} \\ \hat{\beta} \\ \hat{v}^n_{nb} \end{bmatrix}, \tag{5.1}$$

respectively, where β accounts for the uncertain wave speed.,

Denote the true range of the vehicle relative to transponder i by

$$\rho_i = \|p^n_{nb} - p^n_{nt_i}\|_2. \tag{5.2}$$

Now, the pseudo-range measurements from transponder i is modeled by

$$y_i(t) = h_{y,i}(\chi, t) = \frac{1}{\sqrt{\beta}} \left(\rho_i + \epsilon_{y,i}(t)\right), \tag{5.3}$$

where $\epsilon_{y,i} \sim \mathcal{N}(0, \sigma_y^2)$. This is concatenated for M transponders as

$$y(t) = h(\chi, t), \tag{5.4}$$

where

$$y(t) = \begin{bmatrix} y_1(t) \\ \vdots \\ y_M(t) \end{bmatrix}, \ h(\chi) = \begin{bmatrix} h_1(\chi, t) \\ \vdots \\ h_M(\chi, t) \end{bmatrix}, \ \epsilon_y(t) = \begin{bmatrix} \epsilon_{y,1}(t) \\ \vdots \\ \epsilon_{y,M}(t) \end{bmatrix}$$

Notice that $1/\sqrt{\beta}$ has taken the place of the wave speed error factor α in (2.18). This is done to facilitate the ATs in Section 5.1.

LBL transponders that are mounted to the sea floor have relatively little disparity along the z-axis, making the z-component of the NED position hard to estimate. Therefore, a depth measurement will estimate the vertical component while the LBL measurements are used solely for estimating the horizontal position. We denote the horizontal position by

$$p^n_{nb,xy} = \begin{bmatrix} p^n_{nb,x} \\ p^n_{nb,y} \end{bmatrix}, \tag{5.5}$$

where $p^n_{nb,x}$ and $p^n_{nb,y}$ are the north and east components, and the vertical position $p^n_{nb,z}$. Furthermore, we denote the partial state vector

$$s_2 = \begin{bmatrix} p^n_{nb,xy} \\ \beta \end{bmatrix}.$$

In the new AT of Section 5.1.2, an estimate $\underline{s_2}$ is calculated from the LBL and depth measurements. Along with the depth measurement d_m, this constitutes a linearization point $\underline{\chi}$ about which the nonlinear measurement model is linearized. The new second stage KF is therefore a linearized KF, only differing from the third stage KF in the point of linearization.

The depth measurement d_m is modeled by (2.21).

5.1 Stage 1: Algebraic Transformation

5.1.1 AT1

The AT described here is taken from [68] and is denoted AT1. Constructing the measurement

$$\beta y_i^2 = \|p^n_{nb}\|_2^2 - 2{p^n_{nt_i}}^\top p^n_{nb} + \|p^n_{nt_i}\|_2^2 + 2\rho_i \epsilon_{y,i} + \epsilon_{y,i}^2$$

and neglecting the noise terms, allows us to write

$$\beta y_i^2 = r - 2{p^n_{nt_i}}^\top p^n_{nb} + \|p^n_{nt_i}\|^2, \tag{5.6}$$

where $r = {p^n_{nb}}^\top p^n_{nb}$. Now, a linear model can either be achieved through finding and inputting r or through subtraction of one constructed measurement from another. The latter method can be used if 5 or more transponders are available, while the former must be used when there are 4 transponders.

4 transponders

We define a partial state vector and a selection matrix

$$s_1 = \begin{bmatrix} p^n \\ \beta \end{bmatrix}, \; M = \begin{bmatrix} I_3 & 0_{3\times 1} \\ 0_{1\times 3} & 0 \end{bmatrix}$$

such that r can be expressed in terms of s_1 as

$$r = s_1^\top M s_1, \tag{5.7}$$

We notice that (5.6) and (5.7) adds up to 5 equations for the 5 unknowns p^n, β, and r. Now, we show that r can be found explicitly. Concatenating (5.6) yields

$$C_{p\beta} s_1 - r l_N = z, \tag{5.8}$$

where

$$C_{p\beta} = \begin{bmatrix} 2{p^n_{nt_1}}^\top & y_1^2 \\ \vdots & \vdots \\ 2{p^n_{nt_M}}^\top & y_N^2 \end{bmatrix}, \; z = \begin{bmatrix} \|p^n_{nt_1}\|_2^2 \\ \vdots \\ \|p^n_{nt_M}\|_2^2 \end{bmatrix}. \tag{5.9}$$

If $C_{p\beta}$ is invertible, we can find

$$s_1 = r \underbrace{C_{p\beta}^{-1} l_N}_{\text{c}} + \underbrace{C_{p\beta}^{-1} z}_{\text{w}} = rc + w. \tag{5.10}$$

Inserting (5.10) into (5.7) yields the second order equation

$$\begin{aligned} r = (rc+w)^\top M (rc+w) &= r^2 c^\top M c + 2rc^\top M w + w^\top M w \\ r^2 c^\top M c + r \underbrace{(2c^\top M w - 1)}_{h} &+ w^\top M w = 0. \end{aligned}$$

This equation has two solutions

$$r_1, r_2 = \frac{-h \pm \sqrt{h^2 - 4c^\top M c \cdot w^\top M w}}{2c^\top M c}, \tag{5.11}$$

where r_1 denotes the correct and r_2 denotes the wrong one. In order to solve this ambiguity, one might often use circumstantial knowledge, e.g. such as that s_1, when r_2 is inserted into (5.10), has a position that is below the sea floor or a β that greatly differs from 1.

Assuming r_1 is found, the following linear measurement model has been achieved

$$Y = C(t)\chi, \tag{5.12}$$

where

$$Y = z + r_1 l_N,\ C(t) = \begin{bmatrix} C_{p\beta}(t) & 0_{N\times 3} \end{bmatrix}.$$

Assumption 5.1.1. *When $N = 4$, the ambiguity between r_1 and r_2 can be resolved and the correct one found.*

Under Assumption 5.1.1, the measurement equation (5.12) is valid.

5 or more transponders

With five or more transponders, r can be eliminated by subtracting one constructed measurement (5.6) from another. We are now left with at least 4 linear equations for the 4 unknowns p^n and β. We choose to use the Nth measurement for subtraction for presentation purposes and without loss of generality.

$$\begin{aligned} \beta(y_i^2 - y_N^2) =& 2{p_{t_i t_N}^n}^\top p_{nb}^n + \|p_{nt_i}^n\|_2^2 - \|p_{nt_N}^n\|_2^2 \\ &+ 2\rho_i\epsilon_{y,i} + \epsilon_{y,i}^2 - 2\rho_N\epsilon_{y,N} - \epsilon_{y,N}^2. \end{aligned} \tag{5.13}$$

Concatenating and rearranging (5.13) yields

$$Y' = C'\chi, \tag{5.14}$$

where

$$Y' = \begin{bmatrix} \|p_{nt_1}^n\|_2^2 - \|p_{nt_N}^n\|_2^2 \\ \vdots \\ \|p_{nt_{N-1}}^n\|_2^2 - \|p_{nt_N}^n\|_2^2 \end{bmatrix}, C'(t) = \begin{bmatrix} -p_{t_1 t_N}^n & y_1^2(t) - y_M^2(t) \\ \vdots & \vdots \\ -p_{t_{N-1} t_N}^n & y_{N-1}^2(t) - y_N^2(t) \end{bmatrix}.$$

5.1.2 AT2

The AT developed here, denoted AT2, is not entirely similar to those of Section 5.1.1. Instead, the techniques of the Section 5.1.1 are used to gain an estimate of the state, about which a linearization is done. Constructing the measurement

$$\beta y_i^2 = \|p_{nb,xy}^n\|_2^2 - 2{p_{nt_i,xy}^n}^\top p_{nb,xy}^n + \|p_{nt_i,xy}^n\|_2^2 + \|p_{nb,z}^n - p_{nt_i,z}^n\|_2^2$$

and inserting d_m for $p^n_{nb,z}$ allows us to write

$$D_i s_2 = r + z_i, \tag{5.15}$$

where $r = \|p^n_{nb,xy}\|_2^2$ and

$$D_i = \begin{bmatrix} 2{p^n_{nt_i,xy}}^\top & y_i^2 \end{bmatrix}, \; z_i = \|p^n_{nt_i,xy}\|_2^2 + \|p^n_{nb,z} - p^n_{nt_i,z}\|_2^2.$$

For $N = 3$, we concatenate (5.15) as

$$D s_2 = r l_N + z,$$

where

$$D = \begin{bmatrix} D_1 \\ \vdots \\ D_N \end{bmatrix}, \; z = \begin{bmatrix} z_1 \\ \vdots \\ z_N \end{bmatrix},$$

and find

$$s_2 = D^\dagger l_N r + D^\dagger z = cr + w.$$

Now, we assumed that we can find the correct solution r_1, which yields the solution

$$\underline{s}_2 = \begin{bmatrix} \underline{p}^n_{nb,xy} \\ \underline{\beta} \end{bmatrix} = cr_1 + w. \tag{5.16}$$

For $N \geq 4$, we find

$$\underline{s}_2 = D'^\dagger z', \tag{5.17}$$

where

$$D' = \begin{bmatrix} D_1 - D_N \\ \vdots \\ D_{N-1} - D_N \end{bmatrix}, \; z' = \begin{bmatrix} z_1 - z_N \\ \vdots \\ z_{N-1} - z_N \end{bmatrix}.$$

From either (5.16) or (5.17), we find the linearization point

$$\underline{\chi} = \begin{bmatrix} \underline{p}^n_{nb,xy} \\ d_m \\ \underline{\beta} \\ 0_{3\times 1} \end{bmatrix}.$$

The linearization is done by the Taylor expansion

$$h(\chi, t) = h(\underset{\sim}{\chi}, t) + H(\underset{\sim}{\chi})(\chi - \underset{\sim}{\chi}) + \varphi(\chi - \underset{\sim}{\chi}, t), \tag{5.18}$$

where $\varphi(\chi - \underset{\sim}{\chi}, t)$ contains all higher order terms of the linearization and

$$H(\underset{\sim}{\chi}) = \left.\frac{\mathrm{d}h(\chi)}{\mathrm{d}\chi}\right|_{\chi=\underset{\sim}{\chi}} = \begin{bmatrix} H_{p\beta}(\bar{\chi}) & 0_{M\times 3} \end{bmatrix},$$

where

$$H_{p\beta}(\chi) = \begin{bmatrix} \frac{1}{\sqrt{\beta}} \frac{(p^n_{nb} - p^n_{nt_1})^\top}{\|p^n_{nb} - p^n_{nt_1}\|_2} & -\frac{\|p^n_{nb} - p^n_{nt_1}\|_2}{2\sqrt{\beta}^3} \\ \vdots & \vdots \\ \frac{1}{\sqrt{\beta}} \frac{(p^n_{nb} - p^n_{nt_N})^\top}{\|p^n_{nb} - p^n_{nt_N}\|_2} & -\frac{\|p^n_{nb} - p^n_{nt_N}\|_2}{2\sqrt{\beta}^3} \end{bmatrix}.$$

Note that $\varphi = 0$ when $\underset{\sim}{\chi} = \chi$.

5.2 Stage 2: Linear Time-Varying Kalman Filter

Here, second stage KFs using the linear measurement models achieved in Section 5.1 are developed.

5.2.1 LTV KF1

Inserting (2.15) into (2.12) and modeling the wave speed error factor β as a Wiener process yields the following dynamics

$$\begin{aligned} \dot{p}^n_{nb} &= v^n_{nb} \\ \dot{\beta} &= \varepsilon_\beta(t) \\ \dot{v}^n_{nb} &= a^n_{nb} + \varepsilon_{acc}(t), \end{aligned}$$

where the attitude $R^n_b(t)$ is assumed to be a known input signal. The dynamics can be written in compact form as

$$\dot{\chi} = A\chi + Bu(t) + G\epsilon_\chi(t), \tag{5.19}$$

where

$$u(t) = a^n_{nb}\,, \epsilon_\chi(t) = \begin{bmatrix} \epsilon_\beta(t) \\ \epsilon_{acc}(t) \end{bmatrix}$$

$$A = \begin{bmatrix} 0_{3\times3} & 0_{3\times1} & I_3 \\ 0_{1\times3} & 0 & 0_{1\times3} \\ 0_{3\times3} & 0_{3\times1} & 0_{3\times3} \end{bmatrix}, B = \begin{bmatrix} 0_{3\times3} \\ 0_{1\times3} \\ I_3 \end{bmatrix}, G = \begin{bmatrix} 0_{3\times1} & 0_{3\times3} \\ 1 & 0_{1\times3} \\ 0_{3\times1} & I_3 \end{bmatrix}.$$

Now, an LTV KF using this dynamic model with measurement model (5.12) or (5.14) can be employed

$$\dot{\bar{\chi}}_1 = A\bar{\chi}_1 + B(t)u(t) + \bar{K}_1(t)(\grave{Y} - \grave{C}(t)\bar{\chi}_1), \tag{5.20}$$

where $\bar{\chi}_1$ is the state estimate, $\grave{Y}$ and $\grave{C}(t)$ are placeholders for either Y and $C(t)$ or Y' and $C'(t)$, respectively. Furthermore, $\bar{K}_1(t) = \bar{P}_1(t)\grave{C}^\top(t)\grave{\bar{\mathcal{R}}}^{-1}$ where $\bar{P}_1(t)$ is the covariance estimate and $\grave{\bar{\mathcal{R}}} = \{\bar{\mathcal{R}}, \bar{\mathcal{R}}'\}$. The covariance estimate is updated by (1.3c) inserted A, $\grave{C}(t)$, G, $\grave{\bar{\mathcal{R}}}$, $\mathcal{Q}$, and with initial value $\bar{P}_1(0) = \bar{P}_{10}$. Note that $\bar{K}_1(t)$ depends on $\grave{C}(t)$ and $\grave{\bar{\mathcal{R}}}$, and is therefore different for the two ATs. The process covariance matrix $\mathcal{Q}$ is chosen as

$$\mathcal{Q} = \mathrm{E}(\epsilon_\chi(t)\epsilon_\chi^\top(t)) = \begin{bmatrix} \sigma_\beta^2 & 0_{1\times3} \\ 0_{1\times3} & \sigma_{acc}^2 I_3 \end{bmatrix}. \tag{5.21}$$

The measurement covariance matrices $\bar{\mathcal{R}}$ and $\bar{\mathcal{R}}'$ for (5.12) and (5.14), respectively, are provided in Appendix 5.A.

Define $\tilde{\bar{\chi}}_1 = \chi - \bar{\chi}_1$. Subtracting (5.20) from (5.19) yields the error dynamics in the noise-free case

$$\bar{\Sigma}_1 : \dot{\tilde{\bar{\chi}}}_1 = (A - \bar{K}_1(t)\grave{C}(t))\tilde{\bar{\chi}}_1. \tag{5.22}$$

5.2.2 LTV KF2

Using the linearized measurement model (5.18) allows us to develop the second stage KF

$$\dot{\bar{\chi}}_2 = A\bar{\chi}_2 + Bu(t) + \bar{K}_2(t)(y - h(\underline{\chi}) - H(\underline{\chi})(\bar{\chi}_2 - \underline{\chi}),$$

where $\bar{\chi}_2$ denotes the state estimate, $\bar{K}_2(t) = \bar{P}_2(t)H^\top(\underline{\chi})\mathcal{R}^{-1}$ and $\bar{P}_2(t)$ is the covariance estimate. The covariance estimate is updated by (1.3c) inserted A, $H^\top(\underline{\chi})$, G, $\mathcal{R}$, and $\mathcal{Q}$, and with initial value $\bar{P}_{\chi 2}(0) = \bar{P}_{\chi 20}$. The measurement covariance matrix is $\mathcal{R} = I_N\sigma_y^2$.

Define $\tilde{\bar{\chi}}_2 \triangleq \chi - \bar{\chi}_2$. Now, the error dynamics is found to be

$$\bar{\Sigma}_2 : \dot{\tilde{\bar{\chi}}}_2 = (A - \bar{K}_2(t)H(\underline{\chi}))\tilde{\bar{\chi}}_2 + \bar{K}_1(t)\varphi(\chi - \underline{\chi}, t). \tag{5.23}$$

5.3 Stage 3: Linearized Kalman Filter

The third stage linearized KF is identical to that of Section 5.2.2, except for different linearization points. We denote the third stage estimate $\hat{\chi}$, and using the linearization point $\bar{\chi} \in \{\bar{\chi}_1, \bar{\chi}_2\}$ we find the estimator

$$\dot{\hat{\chi}} = A\hat{\chi} + B(t)u(t) + \hat{K}(t)(y(t) - h(\bar{\chi}) - H(\bar{\chi})(\hat{\chi} - \bar{\chi}), \tag{5.24}$$

where $\hat{K}(t) = \hat{P}(t)H^\top(\bar{\chi})\mathcal{R}^{-1}$ and $\hat{P}(t)$ is the covariance estimate. The covariance estimate is updated by (1.3c) inserted A, $H^\top(\bar{\chi})$, G, $\mathcal{R}$, $\mathcal{Q}$, and with initial value $\hat{P}(0) = \hat{P}_0$.

Defining $\tilde{\chi} = \chi - \hat{\chi}$ and subtracting (5.24) from (5.19) yields the error dynamics

$$\hat{\Sigma}: \ \dot{\tilde{\chi}} = (A - \hat{K}(t)H(\bar{\chi})) + \hat{K}(t)\varphi(\chi - \bar{\chi}, t). \tag{5.25}$$

5.4 Stability Analysis

Assumption 5.4.1. *There are $N \geq 3$ non-collinear transponders.*

Assumption 5.4.2. *There are $N \geq 4$ non-coplanar transponders.*

Assumption 5.4.3. *There are $N \geq 5$ non-coplanar transponders.*

Lemma 5.4.1. *The matrix pair (A, G) is UCC, $(A, H(\check{\chi}))$ is UCO under Assumption 5.4.1 for $\check{\chi} \in \{\underline{\chi}, \bar{\chi}_1, \bar{\chi}_2\}$, $(A, C(t))$ is UCO under Assumption 5.4.2, and $(A, C'(t))$ is UCO under Assumption 5.4.3.*

Proof. The proof is given in Appendix 5.B. □

Proposition 5.4.1. *Suppose $\epsilon_\chi = 0$ and $\epsilon_y = 0$, and $\mathcal{Q}$, $\bar{P}_{10}$, $\bar{P}_{20}$, $\mathcal{R}$, $\bar{\mathcal{R}}$, and $\bar{\mathcal{R}}'$ are chosen positive definite.*

1. *The origin $\tilde{\bar{\chi}}_1 = 0$ of the error dynamics $\bar{\Sigma}_1$ is GES.*
2. *The origin $\tilde{\bar{\chi}}_2 = 0$ of the error dynamics $\bar{\Sigma}_2$ is GES.*

Proof. The proof is given in Appendix 5.C □

Proposition 5.4.2. *Suppose $\epsilon_\chi = 0$ and $\epsilon_y = 0$ and $\mathcal{Q}$, $\bar{P}_{10}$, $\bar{P}_{20}$, $\hat{P}_0$, $\mathcal{R}$, $\bar{\mathcal{R}}$, and $\bar{\mathcal{R}}'$ are chosen positive definite.*

1. *The origin* $\tilde{\bar{\chi}}_1 = 0$ *and* $\tilde{\chi} = 0$ *of the cascaded error dynamics* $\bar{\Sigma}_1$–$\hat{\Sigma}$ *is GES.*
2. *The origin* $\tilde{\bar{\chi}}_2 = 0$ *and* $\tilde{\chi} = 0$ *of the cascaded error dynamics* $\bar{\Sigma}_2$–$\hat{\Sigma}$ *is GES.*

Proof. Both proofs follow directly from Johansen and Fossen [8]. □

5.5 Results

Here, results is shown of a simulation study with 50 simulations of 500 seconds each with different randomly generated noise about the same trajectory. In order to compare the filter behavior at different distances from the transponders, three different transponder positions are used. The transponders are located at

$$p^n_{nt_1} = \begin{bmatrix} 10k \\ 10k \\ 0 \end{bmatrix}, \; p^n_{nt_2} = \begin{bmatrix} 10k \\ -10k \\ -5 \end{bmatrix}, \; p^n_{nt_3} = \begin{bmatrix} -10k \\ 10k \\ -5 \end{bmatrix}, \; p^n_{nt_4} = \begin{bmatrix} -10k \\ -10k \\ 0 \end{bmatrix},$$

where $k = \{1, 10, 100\}$ which gives the different transponder positions. The transceiver is located at the origin of the body-fixed coordinate frame. The standard deviation of the range measurement noise term is assumed to increase with k, i.e., $\sigma_y = 0.2m$, $\sigma_y = 1m$, and $\sigma_y = 10m$ are used for $k = 1$, $k = 10$, and $k = 100$, respectively. The standard deviation of the acceleration noise term is $\sigma_{acc} = 0.01m/s^2$ in all three cases.

The simulated trajectory is identical for all simulations, where the vehicle descends before following a lawn-mowing pattern, the first 300 seconds of which can be seen in Figure 5.2. The initial state of the vehicle was

$$p^n_{nb} = \begin{bmatrix} 0 \\ 0 \\ 0 \end{bmatrix}, \; v^n_{nb} = \begin{bmatrix} 0 \\ 0 \\ 0 \end{bmatrix},$$

the true wave speed was $1500m/s$, and the guessed wave speed was $1450m/s$. This yields a wave speed error factor of $\beta = 1.0702$.

The filters of Section 5.1.1 and 5.1.2 are denoted LTV KF1 and LTV KF2, respectively. Similarly, the linearized filters relying on the estimates of LTV KF1 and LTV KF2 as inputs are denoted Lin KF1 and Lin KF2. In addition to these filters, a standard EKF is used as a benchmark. All filters are tuned identically, with $\sigma_\beta = 10^{-3}$, $\sigma_d = 0.1$, and the true values of σ_y and σ_{acc}. The initial covariance

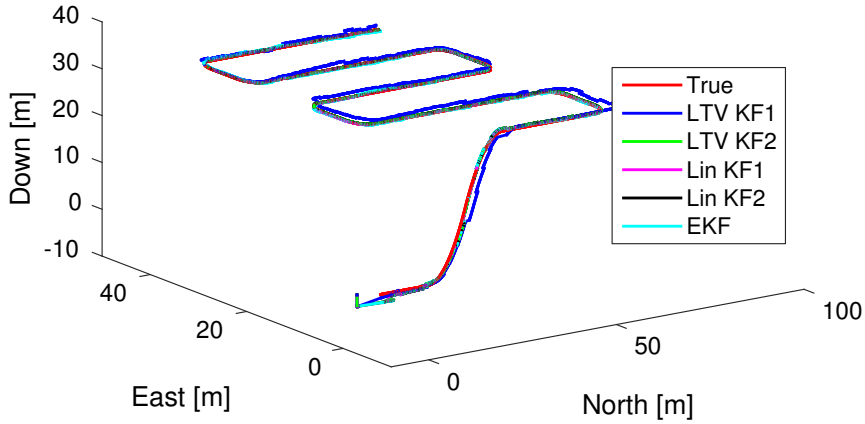

Figure 5.2: The first 300 seconds of the simulated trajectory is shown here for presentation purposes. In the last 200 seconds of the simulation, the vehicle continues straight. Furthermore, $k = 10$ was used.

matrix estimate of all matrices were $P_0 = \text{diag}(1, 1, 1, 0.01, 0.1, 0.1, 0.1)$. The initial position estimate for all filters at each simulation is uniformly drawn from the interval $(-10, 10)m$ for each of the tree axes. The initial velocity estimate is zero, and the initial wave speed error factor is naturally chosen as 1.

The range measurement noise models for the different k-values attempt to model an uncertainty in the range measurements that is increasing with distance. However, it is not claimed that the chosen model is realistic for varying distances. Therefore, the simulation study is not suited to describe a filter's performance at varying distances. Rather, the different filters' performance should be compared for the same values of k.

From Table 5.1, we can immediately conclude that using depth measurements in the AT is beneficial from the performances of LTV KF1 and LTV KF2. The latter consistently outperforms the former in horizontal MAE in all three scenarios. The reason for this seems to be the large errors induced by using the range measurements for estimating the vertical position estimation as well as the horizontal. The depth measurement corrects for this in the state estimate of LTV KF1, but does not prevent it from deteriorating the AT. This is clearly seen in Figure 5.3, where a failure of convergence of the wave speed error factor is caused by the detrimental effect that large noise terms has on the calculation of r_1 in (5.11).

Aiding the AT with a depth measurement can also be seen to provide a position

Table 5.1: Horizontal MAE values in meters from 50 simulations with 3 transponders except LTV KF1 that used 4. EKF* shows the lowest MAE in the 50 simulations.

	$k=1$		$k=10$		$k=100$	
Estimator	XY	Z	XY	Z	XY	Z
LTV KF1	0.652	0.019	3.713	0.019	12.455	0.019
LTV KF2	0.496	0.019	0.441	0.019	1.807	0.019
Lin KF1	0.305	0.019	0.456	0.019	2.965	0.019
Lin KF2	0.304	0.019	0.434	0.019	1.798	0.019
EKF	0.911	0.028	0.550	0.028	1.884	0.028
EKF*	0.359	0.024	0.453	0.024	1.518	0.024

estimate that is sufficiently accurate to use as an input to a linearized KF, which is the LTV KF2. This is apparent from the similar performance between it and the two third stage filters Lin KF1 and Lin KF2. The implementation of LTV KF2 as a linearized KF instead of using a linear transformed model, makes the comparison with LTV KF1 not straight-forward. However, it can safely be concluded that implementing LTV KF1 as a linearized KF would not yield the same accuracy, due to the high MAE of Lin KF1 when $k = 100$.

Interestingly, the high performance of LTV KF2 opens the possibility for not implementing a third stage filter, thereby cutting the computational costs in half. This would make for a filter with the same computational burden as an EKF, but with a global stability result. Furthermore, Table 5.1 suggests that it would not come at a great performance cost either, as it seems to outperform the EKF in every simulation. This is, however, mostly due to the faster convergence of LTV KF2 than that of the EKF. Here, the EKF has been tuned identically as the other filters, which may be far from optimal. However, faster convergence is a significant result in itself. This simulations study does not give evidence that the the steady state behavior of LTV KF2, Lin KF1, or Lin KF2 is any better than that of the EKF. This is exemplified by the EKF's lowest MAE value of all the 50 simulations shown in the bottom row, where the convergence presumably was approximately as fast as the convergence of the other ones.

5.6 Conclusion and Further Work

In this chapter, 3SFs for GES estimation of position, velocity, and the wave speed was developed, and shown in a simulation study to yield similar performance as an EKF. Moreover, it was shown that extending the work of Stovner et al. [68]

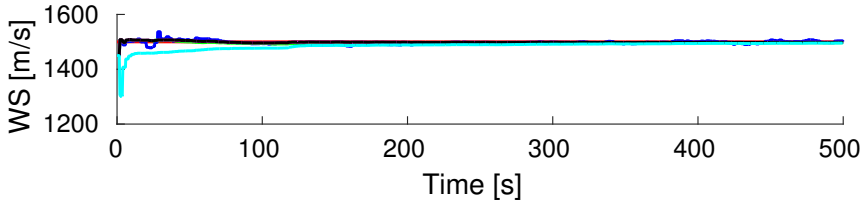

(a) $k = 1$

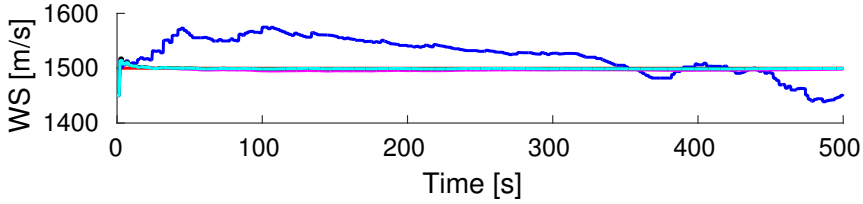

(b) $k = 10$

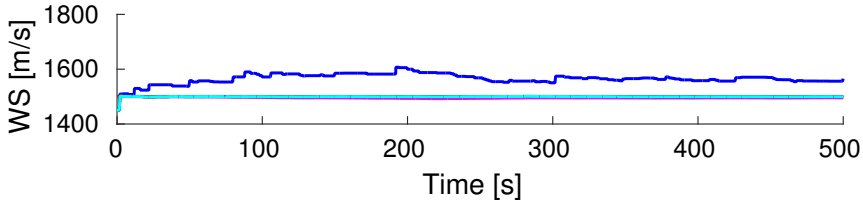

(c) $k = 100$

Figure 5.3: Examples of the wave speed error factor estimation in one of the 50 simulations with the three different transponder positions. The red line marks the true wave speed, while the blue, green, pink, black, and cyan lines represent the LTV KF1, LTV KF2, Lin KF1, Lin KF1, and EKF estimates, respectively.

by aiding the AT with a depth measurement yielded a significant performance improvement. A result of this was that with only a minor performance cost, the third stage filter could be excluded, thus lowering the computational burden by 50%. This gives a filter with approximately the same computational load and estimation accuracy as an EKF, but with the benefits of faster convergence and proven global stability.

This chapter aimed at answering the research question: "*Can the XKF method be applied to position and wave speed estimation using an LBL network in order to improve performance w.r.t. stability and transient behavior, while maintaining the high accuracy of, the EKF?*". The simulation study conducted in this chapter suggests that it can, even at the same computational cost. This motivates further research, which should include:

- a simulation study with more realistic noise models
- verifying the results experimentally in a pool where the wave speed can be assumed to be homogeneous and accurately estimated/measured a priori
- verifying the results experimentally in the sea where spatially varying wave speeds must be assumed, especially at great distances, and effects like bending are present. Also, it can be looked into whether wave speed estimation is helpful or possibly harmful in the presence of these phenomena.

Appendix

5.A Covariance of Constructed Measurements

The algebraically transformed measurements can be described as

$$\begin{aligned} y_i^2 =& \frac{1}{\beta}(\rho_i^2 + 2\rho_i\epsilon_{y,i} + \epsilon_{y,i}^2) \\ y_i^2 - y_M^2 =& \frac{1}{\beta}(\rho_i^2 + 2\rho_i\epsilon_{y,i} + \epsilon_{y,i}^2 - \rho_M^2 - 2\rho_M\epsilon_{y,M} - \epsilon_{y,M}^2) \end{aligned}$$

from which the measurement covariance matrices $\bar{\mathcal{R}}$ and $\bar{\mathcal{R}}'$ can be found with elements

$$\begin{aligned} \mathcal{R}_{ii} =& 4\rho_i^2\sigma_y^2 + 2\sigma_y^4 \\ \mathcal{R}_{ij} =& 0,\ i \neq j \\ \mathcal{R}'_{ii} =& 4(\rho_i^2 + \rho_M^2)\sigma_y^2 + 4\sigma_y^4 \\ \mathcal{R}'_{ij} =& 4\rho_M^2\sigma_y^2 + 2\sigma_y^4,\ i \neq j. \end{aligned}$$

For the unknown value ρ_i, y_i is used.

5.B Proof of Lemma 5.4.1

Let $D(t) \in \{C(t), C'(t), H(\chi)\}$ be a placeholder matrix, and note its general structure $D(t) = [D_y(t), D_\beta(t), \mathbf{0}]$, where $\mathbf{0}$ is a matrix of zeros with appropriate dimensions. Now, we form the partial observability co-distribution (4.26)

$$\mathrm{d}\mathcal{O}_p(t) = \begin{bmatrix} \mathrm{d}\mathcal{O}_0(t) \\ \mathrm{d}\mathcal{O}_1(t) \end{bmatrix} = \begin{bmatrix} D_y(t) & D_\beta(t) & \mathbf{0} \\ \star & \star & D_y(t) \end{bmatrix}.$$

Theorem 4.2 of Meyer [77] proves that $\mathrm{d}\mathcal{O}_p(t)$ has full rank if $[D_y(t), D_\beta(t)]$ and $D_y(t)$ have full rank. This is guaranteed under Assumption 5.4.1–5.4.3, and thus, the systems are UCO.

In order to show that (A, G) is UCC, we form the partial controllability co-distribution (4.27)

$$\mathrm{d}\mathcal{C}_p = \begin{bmatrix} \mathrm{d}\mathcal{C}_0 & \mathrm{d}\mathcal{C}_1 \end{bmatrix} = \begin{bmatrix} 0_{3\times 1} & 0_{3\times 3} & 0_{3\times 1} & I_3 \\ 1 & 0_{1\times 3} & 0 & 0_{1\times 3} \\ 0_{3\times 1} & I_3 & 0_{3\times 1} & 0_{1\times 3} \end{bmatrix}.$$

Since $\mathrm{rank}(\mathrm{d}\mathcal{C}_p) = 7$, the controllability co-distribution has full rank, which concludes the proof.

5.C Proof of Proposition 5.4.1

Neglecting noise, we have that $\underline{\chi} = \chi$, and consequently, that $\varphi = 0$. Now, Kalman and Bucy [5] proves that the origins $\tilde{\bar{\chi}}_1 = 0$ and $\tilde{\bar{\chi}}_2 = 0$ of the error dynamics $\bar{\Sigma}_1$ and $\bar{\Sigma}_2$ are GES, respectively.

Chapter 6

Position Estimation Using Inverted Short Baseline Network

This chapter is based on Stovner, Johansen, and Schjølberg [11, 67] and considers the estimation of the position and velocity of a vehicle using an iSBL hydroacoustic sensor network and a single transponder in the vehicle's surroundings. The hydroacoustic set-up can be seen in Figure 2.5 with $N = 1$ transponder. Two classes of filters are developed, differing in which coordinate frame the state is expressed, i.e. the NED or the body-fixed frame. The development of these filters, the comparison study between them, and the analysis of their stability properties are the main contributions of this chapter.

Figure 6.1 shows the structure of the two classes of filters developed in this chapter. We see that both 3SFs rely on input from an attitude estimator. The estimator (4.7) is used in this chapter, which uses ARS, accelerometer, and magnetometer measurements to find the attitude estimate $\check{z} = (R^n_{\check{b}}, \check{b}^{\check{b}}_{ars})$. Extending this notation, $\tilde{z} = (R^n_b - R^n_{\check{b}}, b^b_{ars} - \check{b}^{\check{b}}_{ars})$ denotes the estimation error and $\dot{z} = (\dot{R}^n_b, \dot{b}^b_{ars})$ the dynamics.

The range and range-difference measurements of the iSBL network are given by (2.19) and (2.20), respectively. In order to simplify derivations, we use the notation

$$\rho_j = \|p^n_{nb} - p^n_{nt} + R^n_b p^b_{bc_j}\|_2 \tag{6.1a}$$

$$= \|p^b_{tb} + p^b_{bc_j}\|_2. \tag{6.1b}$$

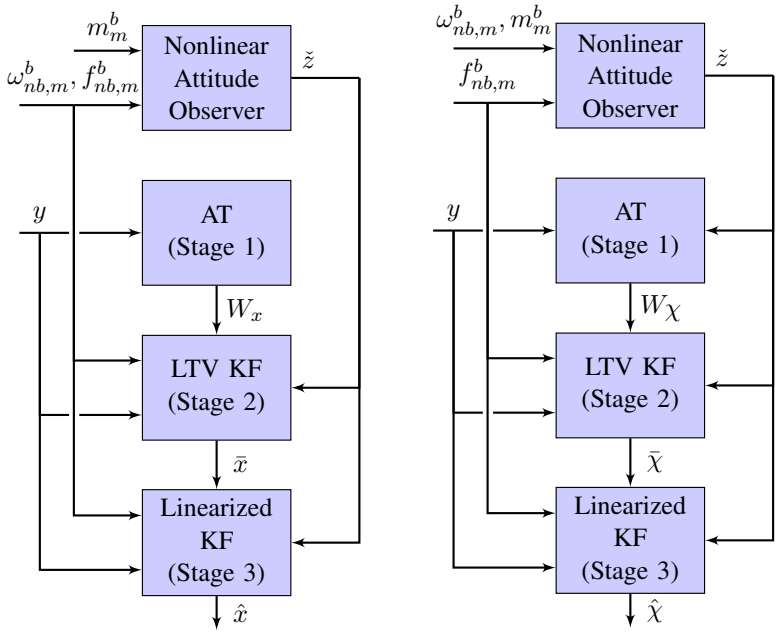

(a) The body-fixed 3SF **(b)** The NED 3SF

Figure 6.1: The structure of the 3SF for the body-fixed and NED formulations, where W_x and W_χ denote the outputs from the body-fixed and NED ATs, respectively.

This allows us to write the measurement equations

$$y_M = h_M(\chi, z) \equiv h_M(x) \triangleq \rho_M + \epsilon_{y,M} \tag{6.2a}$$
$$\partial y_j = h_j(\chi, z) \equiv h_j(x) \triangleq \rho_j - \rho_M + \epsilon_{\partial,j}, \tag{6.2b}$$

which is concatenated into

$$y = \begin{bmatrix} \partial y_1 \\ \vdots \\ \partial y_{M-1} \\ y_M \end{bmatrix}, \; h = \begin{bmatrix} h_1 \\ \vdots \\ h_M \end{bmatrix}, \; \epsilon_\partial = \begin{bmatrix} \epsilon_{\partial,1} \\ \vdots \\ \epsilon_{\partial,M-1} \end{bmatrix}, \; \epsilon_y = \begin{bmatrix} \epsilon_\partial \\ \epsilon_{y,M} \end{bmatrix}.$$

Inserting (2.15)–(2.16) into (2.13) yields

$$\dot{p}_{tb}^b = -S(\omega_{ars}^b - b_{ars}^b)p_{tb}^b + v_{nb}^b \tag{6.3a}$$
$$\dot{v}_{nb}^b = -S(\omega_{ars}^b - b_{ars}^b)v_{nb}^b + f_{nb,m}^b + R_b^{n\top} g^n - \epsilon_{acc}, \tag{6.3b}$$

which is concatenated as

$$\dot{x} = A_x(t,z)x + B_x(z)u(t) + G_x(x)\epsilon_x, \tag{6.4}$$

where

$$A_x(t,z) = \begin{bmatrix} -S(\omega^b_{ars} - b^b_{ars}) & I_3 \\ 0 & -S(\omega^b_{ars} - b^b_{ars}) \end{bmatrix}, \; B_x(z) = \begin{bmatrix} 0 & 0 \\ I_3 & R^{n\top}_b \end{bmatrix}$$
$$G_x(x) = \begin{bmatrix} -S(p^b_{tb}) & 0 \\ -S(v^b_{nb}) & -I_3 \end{bmatrix}, \; u(t) = \begin{bmatrix} f^b_{acc} \\ g^n \end{bmatrix}, \; \epsilon_x = \begin{bmatrix} \epsilon_{ars} \\ \epsilon_{acc} \end{bmatrix}.$$

Inserting (2.15) into (2.12) yields

$$\dot{p}^n_{nb} = v^n_{nb} \tag{6.5a}$$
$$\dot{v}^n_{nb} = R^n_b(f^b_{acc} - \epsilon_{acc}) + g^n, \tag{6.5b}$$

which is concatenated as

$$\dot{\chi} = A_\chi \chi + B_\chi(z)u(t) + G_\chi \epsilon_\chi, \tag{6.6}$$

where

$$A_\chi = \begin{bmatrix} 0 & I_3 \\ 0 & 0 \end{bmatrix}, B_\chi(z) = \begin{bmatrix} 0 & 0 \\ R^n_b & I_3 \end{bmatrix}$$
$$G_\chi(z) = \begin{bmatrix} 0 \\ R^n_b \end{bmatrix}, \epsilon_\chi = \epsilon_{acc}.$$

6.1 Stage 1: Algebraic Transformation

In this section, the ATs of Stovner, Johansen, and Schjølberg [11, 67] are derived in Section 6.1.1–6.1.2 and 6.1.3–6.1.4, respectively. Section 6.1.1–6.1.2 describe ATs that require 3 receivers, while those in Section 6.1.3–6.1.4 require 4.

6.1.1 Body-Fixed Formulation 1

By constructing

$$\begin{aligned}(\partial y_j + y_M)^2 =& (\rho_j - \rho_M + \rho_M + \epsilon_{\partial,j} + \epsilon_{y,M})^2 \\ =& \|p^b_{tb}\|_2^2 + 2{p^b_{bc_j}}^\top p^b_{tb} + \|p^b_{bc_j}\|_2^2 + 2\rho_j(\epsilon_{\partial,j} + \epsilon_{y,M}) + (\epsilon_{\partial,j} + \epsilon_{y,M})^2 \\ y_M^2 =& (\rho_M + \epsilon_{y,M})^2 \\ =& \|p^b_{tb}\|_2^2 + 2{p^b_{bc_M}}^\top p^b_{tb} + \|p^b_{bc_M}\|_2^2 + 2\rho_M \epsilon_{y,M} + \epsilon^2_{y,M},\end{aligned}$$

we get an equation that is quadratic in p_{tb}^b. Defining $r_x \triangleq \|p_{tb}^b\|_2^2$ and neglecting noise, we can write the above as

$$Y_x - l_M r_x = C_{xp} p_{tb}^b + \epsilon_Y, \tag{6.7}$$

where

$$Y_x = \begin{bmatrix} y_1^2 - \|p_{bc_1}^b\|_2^2 \\ \vdots \\ y_M^2 - \|p_{bc_M}^b\|_2^2 \end{bmatrix}, \; C_{xp} = \begin{bmatrix} 2{p_{bc_1}^b}^\top \\ \vdots \\ 2{p_{bc_M}^b}^\top \end{bmatrix}$$

$$\epsilon_{Y_x} = \begin{bmatrix} 2\rho_1(\epsilon_{\partial,1} + \epsilon_{y,M}) + (\epsilon_{\partial,1} + \epsilon_{y,M})^2 \\ \vdots \\ 2\rho_{M-1}(\epsilon_{\partial,M-1} + \epsilon_{y,M}) + (\epsilon_{\partial,M-1} + \epsilon_{y,M})^2 \\ 2\rho_M \epsilon_{y,M} + \epsilon_{y,M}^2 \end{bmatrix}.$$

Now, if r_x can be found explicitly and inserted into (6.7), a linear measurement model is achieved.

Assuming $M \geq 3$ and $\text{rank}(C_{xp}) = 3$, we can find $c_x = C_{xp}^\dagger l_M$ and $w_x = C_{xp}^\dagger Y_x$, where † denotes the Moore-Penrose pseudo-inverse. Now, we find

$$p_{tb}^b = -r_x c_x + w_x \tag{6.8}$$

and insert it into $r_x = \|p_{tb}^b\|_2^2$:

$$r_x^2 \|c_x\|_2^2 - r_x \underbrace{(2c_x^\top w_x + 1)}_{h_x} + \|w_x\|_2^2 = 0.$$

Two solutions can generally be found

$$r_{x1}, r_{x2} = \frac{h_x \pm \sqrt{h_x^2 - 4\|c_x\|_2^2 \|w_x\|_2^2}}{2\|c_x\|_2^2}. \tag{6.9}$$

When $\|c_x\| \neq 0$, the correct of which we denote r_{x1}. If $\|c_x\| = 0$, then $r_{x1} = \|w_x\|_2^2 / h_x$. Assuming this ambiguity can be resolved when $\|c_x\| \neq 0$, and the correct solution can be found, we have successfully constructed a linear measurement equation

$$Y_x + l r_{x1} = C_x x + \epsilon_Y, \tag{6.10}$$

where $C_x = \begin{bmatrix} C_{xp} & 0_{M\times 3} \end{bmatrix}$.

6.1.2 North-East-Down Formulation 1

The derivation of the AT for the NED formulation will be similar to that in Section 6.1.1. The difference is starting from (6.1a) instead of (6.1b):

$$\begin{aligned}(y_j + y_M)^2 =& \|p^n_{nb}\|_2^2 + 2(R^n_b p^b_{bc_j} - p^n_{nt})^\top p^n_{nb} + \|R^n_b p^b_{bc_j} - p^n_{nt}\|_2^2 \\ &+ 2\rho_j(\epsilon_{\partial,j} + \epsilon_{y,M}) + (\epsilon_{\partial,j} + \epsilon_{y,M})^2 \\ y_M^2 =& \|p^n_{nb}\|_2^2 + 2(R^n_b p^b_{bc_j} - p^n_{nt})^\top p^n_{nb} + \|R^n_b p^b_{bc_j} - p^n_{nt}\|_2^2 \\ &+ 2\rho_M \epsilon_{y,M} + \epsilon^2_{y,M}.\end{aligned}$$

Again, neglecting noise and defining $r_\chi = {p^n_{nb}}^\top p^n_{nb}$ yields

$$Y_\chi - l_M r_{\chi 1} = C_\chi \chi + \epsilon_Y, \tag{6.11}$$

where

$$Y_\chi = \begin{bmatrix} y_1^2 - \|R^n_b p^b_{bc_j} - p^n_{nt}\|_2^2 \\ \vdots \\ y_M^2 - \|R^n_b p^b_{bc_M} - p^n_{nt}\|_2^2 \end{bmatrix}, \; C_{\chi_p}(z) = \begin{bmatrix} 2(R^n_b p^b_{bc_1} - p^n_{nt})^\top \\ \vdots \\ 2(R^n_b p^b_{bc_M} - p^n_{nt})^\top \end{bmatrix},$$

$C_\chi(z) = [C_{\chi_p}(z), 0_{M-1\times 3}]$, and $r_{\chi 1}$ is found in the same way as r_{x1}.

6.1.3 Body-Fixed Formulation 2

We begin by computing, in the noise-free case,

$$\begin{aligned}\rho_j^2 - \rho_M^2 =& (\rho_j - \rho_M)(\rho_j + \rho_M) = \\ & 2(p^b_{bc_j} - p^b_{bc_M})^\top p^b_{tb} + \|p^b_{bc_j}\|_2^2 - \|p^b_{bc_M}\|_2^2.\end{aligned}$$

Inspired by Batista, Silvestre, and Oliveira [55], we write

$$\rho_j - \rho_M - \frac{\|p^b_{bc_j}\|^2 - \|p^b_{bc_M}\|^2}{\rho_j + \rho_M} = 2\frac{(p^b_{bc_j} - p^b_{bc_M})^\top}{\rho_j + \rho_M} p^b_{tb}$$

and insert δy_j for $\rho_j - \rho_M$ and $\delta y_j + 2y_M$ for $\rho_j + \rho_M$ to obtain

$$Z'_x = \begin{bmatrix} \delta y_1 + \nu_{x,1} \\ \vdots \\ \delta y_{M-1} + \nu_{x,M-1} \end{bmatrix} = \underbrace{\begin{bmatrix} D_{x,1} \\ \vdots \\ D_{x,M-1} \end{bmatrix}}_{D'_{xp}} p^b_{tb} + \epsilon_\partial, \tag{6.12}$$

where

$$\nu_{x,j} = -\frac{\|p^b_{bc_j}\|_2^2 - \|p^b_{bc_M}\|_2^2}{\delta y_j + 2y_M}, \qquad D_{x,j} = 2\frac{(p^b_{bc_j} - p^b_{bc_M})^\top}{\delta y_j + 2y_M}$$

and the noise in the denominator of $\nu_{x,j}$ and $D_{x,j}$ has been neglected.

In the measurement model (6.12), the $M-1$ range difference measurements are used. In order to use the Mth measurement, i.e. the range measurement between the sender and transponder, we use (6.12) to calculate a crude estimate of p^b_{tb} about which we linearize (6.2a):

$$\underline{p}^b_{tb} = D'^{\dagger}_{x,p} Z'_x.$$

Now, we define

$$\underline{x} \triangleq \begin{bmatrix} \underline{p}^b_{tb} \\ 0_{3\times 1} \end{bmatrix}$$

about which we Taylor expand $h_M(x)$ in (6.2a), i.e.

$$h_M(x) = h_M(\underline{x}) + H_{x,M}(\underline{x})(x - \underline{x}) + \bar{\varphi}_{x,M}(p^b_{tb} - \underline{p}^b_{tb}),$$

where $\bar{\varphi}_{x,M}(p^b_{tb} - \underline{p}^b_{tb})$ are higher order terms, $\bar{\varphi}_{x,M}(0) = 0$, and

$$H_{x,M}(\underline{x}) = \left.\frac{\mathrm{d}h_M(x)}{\mathrm{d}x}\right|_{x=\underline{x}} = \begin{bmatrix} \frac{(\underline{p}^b_{tb} - p^b_{bc_M})^\top}{\|\underline{p}^b_{tb} - p^b_{bc_M}\|_2} & 0_{1\times 3} \end{bmatrix}. \tag{6.13}$$

Finally, we define $D'_x \triangleq [D'_{x,p}, 0_{M-1\times 3}]$ and

$$D_x(\underline{x}) \triangleq \begin{bmatrix} D'_x \\ H_{x,M}(\underline{x}) \end{bmatrix}, \; Z_x \triangleq \begin{bmatrix} Z'_x \\ y_M - h(\underline{x}) + H(\underline{x})\underline{x} \end{bmatrix}, \; \bar{\varphi}_x(p) = \begin{bmatrix} 0 \\ \vdots \\ \bar{\varphi}_{x,M}(p) \end{bmatrix}$$

in order to write the linear measurement model

$$Z_x = D_x(\underline{x})x + \bar{\varphi}_x(p^b_{tb} - \underline{p}^b_{tb}) + \epsilon_y. \tag{6.14}$$

6.1.4 North-East-Down Formulation 2

By the same approach as in Section 6.1.3, but starting with the NED-formulated measurement model (6.1b), a linear measurement model is found as

$$Z'_\chi = D'_{\chi,p}(z)p^b_{tb} + \epsilon_\partial \tag{6.15}$$

for the $M-1$ range difference measurements, where

$$Z'_\chi = \begin{bmatrix} \delta y_1 + \nu_{\chi,1}(z) \\ \vdots \\ \delta y_{M-1} + \nu_{\chi,M-1}(z) \end{bmatrix}, D'_{\chi,p}(z) = \begin{bmatrix} D_{\chi,1}(z) \\ \vdots \\ D_{\chi,M-1}(z) \end{bmatrix}$$

$$\nu_{\chi,j}(z) = \frac{2p^{n\top}_{nt} R^n_b (p^b_{bc_j} - p^b_{bc_M}) - \|p^b_{bc_j}\|_2^2 + \|p^b_{bc_M}\|_2^2}{\delta y_j + 2y_M} \tag{6.16a}$$

$$D_{\chi,j}(z) = \frac{2\left(R^n_b (p^b_{bc_j} - p^b_{bc_M})\right)^\top}{\delta y_j + 2y_M}. \tag{6.16b}$$

Again, the noise in the denominator of $\nu_{\chi,j}$ and $C_{\chi,j}$ was neglected. A position estimate $\underline{p}^n_{nb}$ can be found, about which the range measurement model $h_M(\chi, z)$ in (6.2a) is linearized:

$$\underline{p}^n_{nb} = D'_{\chi,p}(\check{z})^\dagger Z'_\chi.$$

Now, define

$$\underline{\chi} \triangleq \begin{bmatrix} \underline{p}^n_{nb} \\ 0_{3\times 1} \end{bmatrix}$$

and Taylor expand

$$h_{\chi,M}(\chi, z) = h_{\chi,M}(\underline{\chi}, z) + H_{\chi,M}(\underline{\chi}, z)(\chi - \underline{\chi}) + \bar{\varphi}_{\chi,M}(p^n_{nb} - \underline{p}^n_{nb}),$$

where

$$H_{\chi,M}(\underline{\chi}, z) = \begin{bmatrix} \frac{\underline{p}^n_{nb} - p^n_{nt} + R^n_b p^b_{bc_j}}{\|\underline{p}^n_{nb} - p^n_{nt} + R^n_b p^b_{bc_j}\|_2} & 0_{1\times 3} \end{bmatrix}, \tag{6.17}$$

$\bar{\varphi}_{\chi,M}(p^n_{nb} - \underline{p}^n_{nb})$ is higher order terms, and $\bar{\varphi}_{\chi,M}(0) = 0$. Lastly, we define $D'_\chi(z) \triangleq [D'_{\chi,p}(z), 0_{M-1\times 3}]$ and

$$D_\chi(\underline{\chi}, z) \triangleq \begin{bmatrix} D'_\chi(z) \\ H_{\chi,M}(\underline{\chi}, z) \end{bmatrix}, \; Y_\chi \triangleq \begin{bmatrix} Z'_\chi \\ y_M \end{bmatrix}, \; \bar{\varphi}\chi(p) = \begin{bmatrix} 0 \\ \vdots \\ \bar{\varphi}_{\chi,M}(p) \end{bmatrix}$$

in order to write the linear measurement model

$$Z_\chi = D_\chi(\underline{\chi}, z)\chi + \bar{\varphi}_\chi(p^n_{nb} - \underline{p}^n_{nb}) + \epsilon_y. \tag{6.18}$$

6.2 Stage 2: Linear Time-Varying Kalman Filter

In this section, one KF for each of the ATs in Section 6.1 is defined. The error dynamics of each filter is derived for the stability analysis in Section 6.4.

6.2.1 Body-Fixed Formulation 1

The LTV KF based on the linear measurement model (6.10) with estimate $\bar{x}_1$ is defined as

$$\dot{\bar{x}}_1 \triangleq A_x(\check{z}, t)\bar{x} + B_x(\check{z})u(t) + \bar{K}_{x1}(t)(Y_x + l_M r_{x1} - C_x\bar{x}_1), \tag{6.19}$$

where $\bar{K}_{x1}(t) = \bar{P}_{x1}(t)C_x^\top \mathcal{R}_Y^{-1}$ and $\bar{P}_{x1}(t)$ is the covariance estimate. The covariance estimate is updated by (1.3c) inserted $A_x(\check{z}, t)$, C_x, $G_x(0)$, the process covariance matrix

$$\mathcal{Q}_x = \mathrm{E}(\epsilon_x \epsilon_x^\top) = \begin{bmatrix} \sigma^2_{ars} I_3 & 0_{3\times 3} \\ 0_{3\times 3} & \sigma^2_{acc} I_3 \end{bmatrix}, \tag{6.20}$$

and the measurement covariance matrix

$$\bar{\mathcal{R}}_Y = \mathrm{Cov}(\epsilon_Y, \epsilon_Y) = \mathrm{E}\left((\epsilon_Y - \mathrm{E}(\epsilon_Y))(\epsilon_Y - \mathrm{E}(\epsilon_Y))^\top\right) \tag{6.21}$$

whose elements are given by

$$\bar{\mathcal{R}}_{Y,ji} = \begin{cases} 4\rho_j\rho_i(\sigma_y^2 + \sigma_\partial^2) + 2(\sigma_\partial^2 + \sigma_y^2)^2, & i = j \text{ and } i, j \in (1, ..., M-1) \\ 4\rho_j\rho_i\sigma_y^2 + 2\sigma_y^4, & \text{otherwise.} \end{cases} \tag{6.22}$$

The initial covariance estimate is $\bar{P}_{x1}(0) = \bar{P}_{x10}$. Notice that the matrix $G_x(0)$ with zero input was chosen. This choice is explained in Appendix 6.A.

Define the estimation error $\tilde{\bar{x}}_1 \triangleq x - \bar{x}_1$. Subtracting (6.19) from (6.4), inserting (6.10), and neglecting noise yield the error dynamics

$$\bar{\Sigma}_{x1} : \dot{\tilde{\bar{x}}}_1 = (A_x(\check{z}, t) - \bar{K}_{x1}(t)C_x)\tilde{\bar{x}}_1 + \bar{\xi}_{x1}(z, \check{z}, x, t), \tag{6.23}$$

where $\bar{\xi}_{x1}(z, \check{z}, x, t) = (A_x(z, t) - A_x(\check{z}, t))x + (B_x(z) - B_x(\check{z}))u(t)$.

6.2.2 North-East-Down Formulation 1

The LTV KF based on the linear measurement model (6.11) with estimate $\bar{\chi}_1$ is defined as

$$\dot{\bar{\chi}}_1 \triangleq A_\chi \bar{\chi}_1 + B_\chi(\check{z})u + \bar{K}_{\chi 1}(t)(Y_\chi + l_M r_{\chi 1} - C_\chi(\check{z})\bar{\chi}_1), \tag{6.24}$$

where $\hat{K}_{\chi 1}(t) = \bar{P}_{\chi 1}(t)C_\chi^\top(\check{z})\mathcal{R}_Y^{-1}$ and $\bar{P}_{\chi 1}(t)$ is the covariance estimate. The covariance estimate is updated by (1.3c) inserted A_χ, $C_\chi(\check{z})$, $G_\chi(\check{z})$, $\mathcal{R}_Y$, and the process covariance matrix

$$Q_\chi = E(\epsilon_\chi \epsilon_\chi^\top) = I_3 \sigma_{acc}^2. \tag{6.25}$$

The initial value of the covariance estimate is $\bar{P}_{\chi 1}(0) = \bar{P}_{\chi 10}$.

The implicit assumption that r_{x1} and $r_{\chi 1}$ does not contribute to the measurement noise has been made here, and is far from true. Jørgensen, Johansen, and Schjølberg [78] numerically models the noise in the r-term, which could have be done here also to improve performance.

Define the estimation error $\tilde{\bar{\chi}}_1 \triangleq \chi - \bar{\chi}_1$. Subtracting (6.24) from (6.6), inserting (6.11), and neglecting noise yield the error dynamics

$$\bar{\Sigma}_{\chi 1}: \ \dot{\tilde{\bar{\chi}}}_1 = (A_\chi - \bar{K}_{\chi 1}(t)C_\chi(\check{z}))\tilde{\bar{\chi}}_1 + \bar{\xi}_{\chi 1}(z, \check{z}, t), \tag{6.26}$$

where

$$\bar{\xi}_{\chi 1}(z, \check{z}, t) = \bar{K}_{\chi 1}(t)(C_\chi(z) - C_\chi(\check{z}))\chi + (B_\chi(z) - B_\chi(\check{z}))u(t).$$

6.2.3 Body-Fixed Formulation 2

The LTV KF based on the linear measurement model (6.14) with estimate $\bar{x}_2$ is defined as

$$\dot{\bar{x}}_2 = A_x(\check{z}, t)\bar{x}_2 + B_x(\check{z})u(t) + \bar{K}_{x2}(t)(Z_x - D_x(\underline{x})\bar{x}_2), \tag{6.27}$$

where $\bar{K}_{x2}(t) = \bar{P}_{x2}(t)D_x^\top(\underline{x})\mathcal{R}^{-1}$ and $\bar{P}_{x2}(t)$ is the covariance estimate. The covariance estimate is updated by (1.3c) inserted $A_x(\check{z}, t)$, $D_x(\underline{x})$, $G_x(0)$, $\mathcal{Q}_x$ in (6.20), and measurement covariance matrix

$$\begin{aligned}\mathcal{R} &= \mathrm{Cov}(\epsilon_y, \epsilon_y) = \mathrm{E}\left((\epsilon_y - \mathrm{E}(\epsilon_y))(\epsilon_y - \mathrm{E}(\epsilon_y))^\top\right) \\ &= \begin{bmatrix} \sigma_\partial^2 I_{M-1} & 0_{M-1\times 1} \\ 0_{1\times M-1} & \sigma_y^2 \end{bmatrix}.\end{aligned} \tag{6.28}$$

The initial estimate of the covariance matrix is $\bar{P}_{x2}(0) = \bar{P}_{x20}$.

Define the estimation error $\tilde{\bar{x}}_2 = x - \bar{x}_2$. Subtracting (6.27) from (6.4), inserting (6.14), and neglecting noise yield the error dynamics

$$\bar{\Sigma}_{x2}: \ \dot{\tilde{\bar{x}}}_2 = (A_x(\check{z},t) - \bar{K}_{x2}(t)D_x)\tilde{\bar{x}}_2 + \bar{\xi}_{x2}(z,\check{z},p^b_{tb},\underline{p}^b_{tb},t), \tag{6.29}$$

where

$$\begin{aligned}\bar{\xi}_{x2}(z,\check{z},p^b_{tb},\underline{p}^b_{tb},t) =&(A_x(z,t) - A_x(\check{z},t))x + (B_x(z) - B_x(\check{z}))u(t)\\ &+ \bar{K}_{x2}(t)\bar{\varphi}_x(p^b_{tb} - \underline{p}^b_{tb}).\end{aligned}$$

6.2.4 North-East-Down Formulation 2

The LTV KF based on the linear measurement model (6.18) with estimate $\bar{\chi}_2$ is defined as

$$\dot{\bar{\chi}}_2 \triangleq A_\chi \bar{\chi}_2 + B_\chi(\check{z})u + \bar{K}_{\chi 2}(Z_\chi - D_\chi(\underline{\chi},\check{z})\bar{\chi}_2), \tag{6.30}$$

where $\bar{K}_{\chi 2}(t) = \bar{P}_{\chi 1}(t)D^\top_\chi(\underline{\chi},\check{z})\mathcal{R}^{-1}$ and $\bar{P}_{\chi 2}(t)$ is the covariance estimate. The covariance estimate is updated by (1.3c) inserted A_χ, $D_\chi(\underline{\chi},\check{z})$, $G_\chi(\check{z})$, $\mathcal{R}$, $\mathcal{Q}_x$, and with initial value $\bar{P}_{\chi 2}(0) = \bar{P}_{\chi 20}$.

Define the estimation error $\tilde{\bar{\chi}}_2 = \chi - \bar{\chi}$. Subtracting (6.30) from (6.6), inserting (6.18), and neglecting noise yield the error dynamics

$$\bar{\Sigma}_{\chi 2}: \ \dot{\tilde{\bar{\chi}}}_2 = (A_\chi - \bar{K}_{\chi 2}(t)D_\chi(\underline{\chi},\check{z}))\tilde{\bar{\chi}}_2 + \bar{\xi}_{\chi 2}(z,\check{z},t), \tag{6.31}$$

where

$$\begin{aligned}\bar{\xi}_{\chi 2}(z,\check{z},p^n_{nb},\underline{p}^n_{nb},t) =&(B_\chi(z) - B_\chi(\check{z}))u(t) + \bar{K}_{\chi 2}(t)\bar{\varphi}_\chi(p^n_{nb} - \underline{p}^n_{nb})\\ &+ \bar{K}_{\chi 2}(t)(D_\chi(\underline{\chi},z) - D_\chi(\underline{\chi},\check{z}))\chi.\end{aligned}$$

6.3 Stage 3: Linearized Kalman Filter

In this section, KFs are developed that use models linearized about the stage 2 estimates in Section 6.2.

6.3.1 Body-Fixed Formulation

Linearizing (6.2) about $\bar{x}_i, i \in \{1, 2\}$ yields

$$h(x) = h(\bar{x}) + H_x(\bar{x})\tilde{\bar{x}}_i + \hat{\varphi}_x(\tilde{\bar{x}}_i), \tag{6.32}$$

where $\tilde{\bar{x}}_i \triangleq x - \bar{x}_i$, $\hat{\varphi}_x$ is higher order terms,

$$H_x(x) = \begin{bmatrix} H_{x,1}(x) \\ \vdots \\ H_{x,M}(x) \end{bmatrix},$$

$$H_{x,j}(x) = \begin{bmatrix} \frac{(p^b_{tb} - p^b_{bc_j})^\top}{\|p^b_{tb} - p^b_{bc_j}\|_2} - \frac{(p^b_{tb} - p^b_{bc_M})^\top}{\|p^b_{tb} - p^b_{bc_M}\|_2} & 0_{1\times 3} \end{bmatrix}, \; j = (1, ..., M-1),$$

and $H_{x,M}(x)$ is given by (6.13).

Denote by $\hat{x}$ the state estimate, which is updated by

$$\dot{\hat{x}} \triangleq A_x(\check{z}, t)\hat{x} + B_x(\check{z})u(t) + \hat{K}_x(t)(y - \hat{y}_x) \tag{6.33a}$$

$$\hat{y}_x \triangleq h(\bar{x}_i) + H_x(\bar{x}_i)(\hat{x} - \bar{x}_i), \tag{6.33b}$$

where $\hat{K}_x(t) = \hat{P}_x(t)H_x^\top(\bar{x}_i)\mathcal{R}^{-1}$ and $\hat{P}_x(t)$ is the covariance estimate. The covariance estimate is updated by (1.3c) inserted $A_x(\check{z}, t)$, $H_x(\bar{x}_i)$, $G_x(\bar{x}_i)$, $\mathcal{Q}_x$ in (6.20), and $\mathcal{R}$ in (6.28) and with initial estimate $\hat{P}_x(0) = \hat{P}_{x0}$.

Define the estimation error $\tilde{x} \triangleq x - \hat{x}$. Subtracting (6.33a) from (6.4), inserting (6.33b), and neglecting noise yield the error dynamics

$$\hat{\Sigma}_x : \; \dot{\tilde{x}} = (A_x(\check{z}, t) - \hat{K}_x(t)H_x(\bar{x}))\tilde{x} + \hat{\xi}_x(x, z, \bar{x}, \check{z}, t), \tag{6.34}$$

where

$$\hat{\xi}_x(x, z, \bar{x}, \check{z}, t) = (A_x(z, t) - A_x(\check{z}, t))x + (B_x(z) - B_x(\check{z}))u(t) - \hat{K}_x(t)\hat{\varphi}_x(\tilde{\bar{x}}).$$

6.3.2 North-East-Down Formulation

Linearizing (6.2) about $\bar{\chi}_i, i \in \{1, 2\}$ yields

$$h(\chi, z) = h(\bar{\chi}_i, z) + H_\chi(\bar{\chi}_i, z)\tilde{\bar{\chi}}_i + \hat{\varphi}_\chi(\tilde{\bar{\chi}}_i),$$

where $\tilde{\bar{\chi}}_i \triangleq \chi - \bar{\chi}_i, i \in (1,2)$, $\hat{\varphi}\chi$ is higher order terms,

$$H_{\chi,j}(\chi,z) = \begin{bmatrix} \frac{(p^n_{nb}+R^n_b p^b_{bc_j}-p^n_{nt})^\top}{\|p^n_{nb}+R^n_b p^b_{bc_j}-p^n_{nt}\|_2} - \frac{(p^n_{nb}+R^n_b p^b_{bc_m}-p^n_{nt})^\top}{\|p^n_{nb}+R^n_b p^b_{bc_m}-p^n_{nt}\|_2} & 0_{1\times 3} \end{bmatrix}$$

for $j \in (1,...,M-1)$, and $H_{\chi,M}(\chi,z)$ is given by (6.17).

Let $\hat{\chi}$ denote the state estimate whose update equations is defined as

$$\dot{\hat{\chi}} \triangleq A_\chi \hat{\chi} + B_\chi(\check{z})u + \hat{K}_\chi(t)(y - \hat{y}_\chi) \tag{6.35a}$$

$$\hat{y}_\chi \triangleq h(\bar{\chi}_i,\check{z}) + H(\bar{\chi}_i,\check{z})(\hat{\chi} - \bar{\chi}_i), \tag{6.35b}$$

where $\hat{K}_\chi(t) = \hat{P}_\chi(t)H^\top_\chi(\bar{\chi}_i,\check{z})\mathcal{R}^{-1}$ and $\hat{P}_\chi(t)$ is the covariance estimate. The covariance estimate is updated by (1.3c) inserted A_χ, $H_\chi(\bar{\chi}_i,\check{z})$, $G_\chi(\bar{\chi}_i)$, $\mathcal{Q}_\chi$, and $\mathcal{R}$ with the initial value $\hat{P}_{\chi_0}$.

Now, define the estimation error $\tilde{\chi} = \chi - \hat{\chi}$. Subtracting (6.35a) from (6.6), inserting (6.35b), and neglecting noise yield the error dynamics

$$\hat{\Sigma}_\chi : \dot{\tilde{\chi}} = (A_\chi - \hat{K}_\chi(t)H_\chi(\bar{\chi}_i,\check{z}))\tilde{\chi} + \hat{\xi}_\chi(\chi,\bar{\chi}_i,z,\check{z},t), \tag{6.36}$$

where

$$\begin{aligned}\hat{\xi}_\chi(\chi,\bar{\chi}_i,z,\check{z},t) =& h(\bar{\chi}_i,z) - h(\bar{\chi}_i,\check{z}) + (H_x(\bar{\chi}_i,z) - H_x(\bar{\chi}_i,\check{z}))\tilde{\bar{\chi}}_i \\ &- \hat{K}_\chi(t)\hat{\varphi}_\chi(\tilde{\bar{\chi}}_i) + (B_\chi(z) - B_\chi(\check{z}))u(t).\end{aligned}$$

6.4 Stability Analysis

Assumption 6.4.1. *There are at least 3 non-collinear receivers on the vehicle.*

Assumption 6.4.2. *There are at least 4 non-coplanar receivers on the vehicle.*

Lemma 6.4.1. *The systems*

1. $(A_x(\check{z},t), C_x, G_x(0))$ *under Assumption 6.4.1*
2. $(A_\chi, C_\chi(\check{z}), G_\chi(\check{z}))$ *under Assumption 6.4.1*
3. $(A_x(\check{z},t), D_x(\underline{x}), G_x(0))$ *under Assumption 6.4.2*
4. $(A_\chi, D_\chi(\underline{\chi},\check{z}), G_\chi(\check{z}))$ *under Assumption 6.4.2*

5. $(A_x(\check{z},t), H_x(\bar{x}), G_x(0))$ *under Assumption 6.4.1*
6. $(A_\chi, H_\chi(\bar{\chi},\check{z}), G_\chi(\check{z}))$ *under Assumption 6.4.1*

are UCO and UCC.

Proof. The proof is given in Appendix 6.B. □

In the following, the inputs $f^b_{nb,m}$ and $\omega^b_{nb,m}$ are assumed to be bounded.

Since A_x, B_x, C_x, D_x, h, $\bar{\varphi}_x$ are smooth and z, $\check{z}$, p^b_{tb}, $\underline{p}^b_{tb}$, u are bounded, there exist constants $\bar{\alpha}_{x1}, \bar{\alpha}_{x2} > 0$ such that

$$\bar{\xi}_{x1}(z,\check{z},x,t) \leq \bar{\alpha}_{x1}(\|\tilde{z}\|_2^2) \tag{6.37a}$$

$$\bar{\xi}_{x2}(z,\check{z},p^b_{tb},\underline{p}^b_{tb},t) \leq \bar{\alpha}_{x2}(\|p^b_{tb}-\underline{p}^b_{tb}\|_2^2 + \|\tilde{z}\|_2^2) \tag{6.37b}$$

Since B_χ, C_χ, D_χ, h, $\bar{\varphi}_\chi$ are smooth and z, $\check{z}$, p^n_{nb}, $\underline{p}^n_{nb}$, u are bounded, there exist constants $\bar{\alpha}_{\chi 1}, \bar{\alpha}_{\chi 2} > 0$ such that

$$\bar{\xi}_{\chi 1}(z,\check{z},t) \leq \bar{\alpha}_{\chi 1}(\|\tilde{z}\|_2^2) \tag{6.38a}$$

$$\bar{\xi}_{\chi 2}(z,\check{z},p^n_{nb},\underline{p}^n_{nb},t) \leq \bar{\alpha}_{\chi 2}(\|p^n_{nb}-\underline{p}^n_{nb}\|_2^2 + \|\tilde{z}\|_2^2). \tag{6.38b}$$

Proposition 6.4.1. *Let Σ_z denote the error dynamics $\dot{\tilde{z}}$. Assume $\mathcal{Q}_x$, $\mathcal{Q}_\chi$, $\mathcal{R}_Y$, $\mathcal{R}$, $\bar{P}_{xi0}$, $\bar{P}_{\chi i0}$, $i \in \{1,2\}$ are chosen positive definite, and $\epsilon_y = 0$,$\epsilon_x = 0$.*

1. *The equilibrium points $\tilde{z} = (0,0)$ and $\tilde{\bar{x}}_i = 0$ of the cascaded error dynamics Σ_z–$\bar{\Sigma}_{xi}$ for $i \in \{1,2\}$ is GES.*
2. *The equilibrium points $\tilde{z} = (0,0)$ and $\tilde{\bar{\chi}}_i = 0$ of the cascaded error dynamics Σ_z–$\bar{\Sigma}_{\chi i}$ for $i \in \{1,2\}$ is GES.*

Proof. The proof is given in Appendix 6.C □

Since A_x, B_x, h, H_x, $\hat{\varphi}_x$ are smooth and z, $\check{z}$, x, u, and $\bar{x}_i$, $i \in \{1,2\}$, are bounded, there exists a constant $\hat{\alpha}_x > 0$ such that

$$\hat{\xi}_x(z,\check{z},x,\bar{x}_i,t) \leq \hat{\alpha}_x(\|x-\bar{x}_i\|_2^2 + \|\tilde{z}\|_2^2), i \in \{1,2\}. \tag{6.39}$$

Since B_χ, h, H_χ, $\hat{\varphi}_\chi$ are smooth and z, $\check{z}$, χ, u, and $\bar{\chi}_i$, $i \in \{1,2\}$, are bounded, there exists a constant $\hat{\alpha}_\chi > 0$ such that

$$\hat{\xi}_\chi(z,\check{z},\chi,\bar{\chi}_i,t) \leq \hat{\alpha}_\chi(\|\chi-\bar{\chi}_i\|_2^2 + \|\tilde{z}\|_2^2), i \in \{1,2\}. \tag{6.40}$$

Proposition 6.4.2. *Assume $\mathcal{Q}_x$, $\mathcal{Q}_\chi$, $\mathcal{R}$, $\hat{P}_{x0}$, $\hat{P}_{\chi 0}$, are chosen positive definite, and $\epsilon_y = 0$,$\epsilon_x = 0$.*

1. *The origin $\tilde{z} = (0,0)$, $\tilde{\bar{x}}_i = 0$, and $\tilde{x} = 0$ of the error dynamics cascade Σ_z–$\bar{\Sigma}_{xi}$–$\hat{\Sigma}_x$, $i \in \{1,2\}$, is GES.*

2. *The origin $\tilde{z} = (0,0)$, $\tilde{\bar{\chi}}_i = 0$, and $\tilde{\chi} = 0$ of the error dynamics cascade Σ_z–$\bar{\Sigma}_{\chi i}$–$\hat{\Sigma}_\chi$, $i \in \{1,2\}$, is GES.*

Proof. The proof is similar to that of Proposition 6.4.1. □

6.5 Results

In this section, the results of simulations and experiments are shown.

A depth measurement, modeled by

$$y_d = p^n_{nt,z} + \underbrace{\begin{bmatrix} R^n_{b,z} & 0_{1\times 3} \end{bmatrix}}_{C^b_d(\check{z})} x = \underbrace{\begin{bmatrix} 0 & 0 & 1 & 0_{1\times 3} \end{bmatrix}}_{C^n_d} \chi \tag{6.41}$$

where $R^n_{b,z}$ and $p^n_{nt,z}$ are the third rows of $R^n_{b,z}$ and $p^n_{nt,z}$, respectively, is added to the filters by appending y_d to y, C^b_d to C_x and H_x, and C^n_d to C_χ and H_χ. It can be shown that this relaxes Assumption 6.4.2 to minimum 3 non-collinear receivers that construct minimally 2 non-vertical baselines.

In the implementation of the filters, some practical considerations were taken:

- $-S(p^b_{tb})$ and $-S(v^b_{nb})$ were removed from $G_x(x)$, i.e. $G_x(0)$ was used, since they greatly deteriorated the estimation accuracy. This is assumed to be caused by errors in the estimate of p^b_{tb} leading to an erroneous increase in the covariance matrix over time, and thus, far from optimal corrections.

- For the body-fixed filters, the depth measurement variance was increased by a factor of 100, i.e. $\mathcal{R}_d = 100\sigma^2_d$. This accounted for the impact of small errors in R^n_b, which was amplified by the distance to the transponder, as can be seen in (6.41).

In the plots below, the following color coding is used:

1. Red — True or camera system trajectory
2. Pink — Body-fixed stage 2 filter (6.19)
3. Blue — Body-fixed stage 2 filter (6.27)
4. Cyan — NED stage 2 filter (6.30)
5. Grey — Loosely coupled NED filter
6. Orange — Body-fixed stage 3 filter (6.33)
7. Green — NED stage 3 filter (6.35)
8. Black — EKF based on NED formulation

The loosely coupled filter 5 is a NED formulated filter with the measurement model $\breve{p}^n_{nb} = C\chi$, where $C = [I_3, 0_{3\times3}]$. The NED stage 2 filter (6.24) was not used due to its poor performance [11].

6.5.1 Simulations

The simulations were conducted with three different transponder positions in order to show how the estimators perform with increasing range measurements. In each of the three simulated scenarios, 50 simulations were run with different randomly generated noise. In the 800 seconds long scenario, the UV stood still for 400 seconds before following the trajectory shown in Figure 6.2.

The transponder was placed at $p^n_{nt} = [-10, -20, 5]m$, $p^n_{nt} = [-100, -200, 50]m$, and $p^n_{nt} = [-1000, -2000, 50]m$ in the three scenarios, while the $M = 4$ receivers on the body were placed at

$$p^b_{bc_1} = [0.6, 0.3, -0.3]m,\ p^b_{bc_2} = [0.6, -0.3, 0.3]m$$
$$p^b_{bc_3} = [-0.6, 0.3, 0.3]m,\ p^b_{bc_4} = [-0.6, -0.3, -0.3]m,$$

where $p^b_{bc_4}$ was also the position of the sender.

The initial state of the vehicle was given by $p^n_{nb} = [0, 0, 0]m$, $v^n_{nb} = [0, 0, 0]m/s$, $R^n_b = I_3$, while the ARS bias was $b^b = [0.012, -0.021, 0.014]rad/s$. The standard deviations of the measurement noises were $\sigma_y = 1m$, $\sigma_\partial = 0.01m$,

Table 6.1: MAE values of the last 400 seconds of simulation in the cases where distance to the transponder was short (s), medium (m), and long (l).

Est.	XY s [m]	Z s [m]	XY m [m]	Z m [m]	XY l [m]	Z l [m]
2)	0.095	0.240	0.226	0.254	15.437	0.406
3)	0.090	0.235	0.211	0.252	1.753	0.365
4)	0.082	0.025	0.194	0.025	0.848	0.025
5)	0.070	0.025	0.234	0.025	1.571	0.025
6)	0.087	0.236	0.200	0.251	1.735	0.365
7)	0.078	0.025	0.177	0.025	0.718	0.025
8)	0.078	0.025	0.176	0.025	0.718	0.025

$\sigma_d = 0.1m$, $\sigma_{acc} = 0.01m/s^2$, $\sigma_{ars} = 0.01rad/s$, and $\sigma_{mag} = 0.01$. The reference vectors used for attitude estimation were

$$r_1^n = -\frac{g^n}{\|g^n\|_2},\ r_1^b = \frac{f_{nb,m}^b}{\|f_{nb,m}^b\|_2},\ r_2^n = m^n = \begin{bmatrix}1\\0\\0\end{bmatrix},\ r_2^b = \frac{m_m^b}{\|m_m^b\|_2}.$$

The frequency of iSBL, depth, and IMU measurement retrieval were $1Hz$, $10Hz$, and $100Hz$, respectively.

The initial position, velocity, attitude, and bias estimates were $\check{p}_{nb}^n(0) = [0,0,0]m$, $\check{v}_{nb}^n(0) = [0,0,0]m/s$, $R_{\check{b}}^n(0) = I_3$, and $\check{b}^{\check{b}}(0) = [0,0,0]rad/s$, from which the initial state of all estimators were found. The initial value of all covariance matrices were chosen as $P(0) = \text{blockdiag}(I_3, 0.1I_3)$. Choices for the attitude observer tuning parameters were $k_I = 0.05$, $\sigma = 1$, and $K_p = 1$. All estimators were updated with $100Hz$.

The difficult geometry of this estimation problem, i.e. the short baselines between receivers compared to the distance to transponder, makes this set-up sensitive to noise on the acoustic measurements. This calls for conservative measurement updates in the KFs. This can be seen by the slow convergence of the estimators in Figure 6.3, which is seen to take approximately 100 seconds for all estimators even with no initial errors apart from the ARS bias. Little of the slow convergence can be attributed to the initial ARS bias error, since the NED and body-fixed filters converge with approximately the same speeds. Rather, this is due to the convergence of the covariance matrix.

In Table 6.1, the MAE of the horizontal (XY) and vertical (Z) positions for the last 400 seconds of simulations of the three scenarios is shown. The increasing

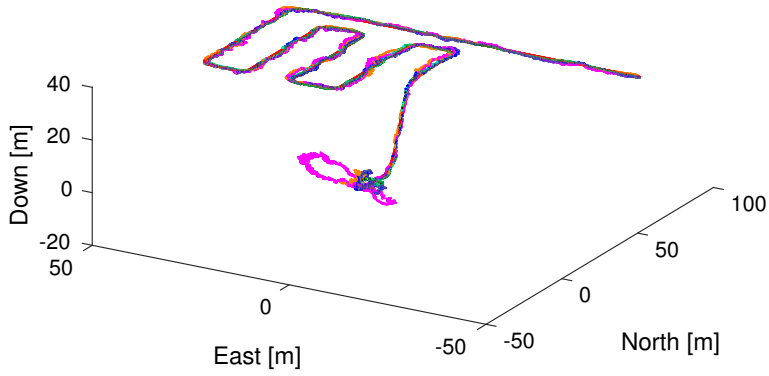

Figure 6.2: The simulated trajectory and estimates in one of the simulations.

horizontal MAE with increasing distance to transponder is evidence that the noise sensitivity increases with distance as well. The vertical errors, however, vary less with distance. The NED formulated filters 4, 5, 7, and 8 have constant vertical MAEs, while the body-fixed filters 2, 3, and 6 increase somewhat. Moreover, the vertical errors are more than 10 times higher for the body-fixed filters than the NED filters. This is due to the noisy rotation matrix in (6.41), which has a detrimental effect on the vertical position estimation. One can draw the conclusion that the NED filters generally outperform the body-fixed filters both in vertical and horizontal performance. Looking at the NED formulated filters only, we see that the loosely coupled filter 5 performs substantially worse than the others. This is due to the highly noise sensitive calculation of $\breve{p}^n_{nb}$, and speaks for the benefit of using a tightly coupled filter scheme. Filter 4 has somewhat higher MAE than the linearization based filters 7 and 8. Compared to filter 7, it only has half the computational complexity since it employs one KF instead of two, and compared to filter 8, it has guaranteed stability. Therefore, it is argued that filter 4 yields the best compromise between computational load, stability, and performance.

Filter 7 and 8 have similar performances, which is expected as filter 8 is just an EKF version of filter 7.

6.5.2 Experiments

The experiment was conducted in MCLab at NTNU, described in Section 3.1.

The experimental set-up was slightly different than in the simulations, described below:

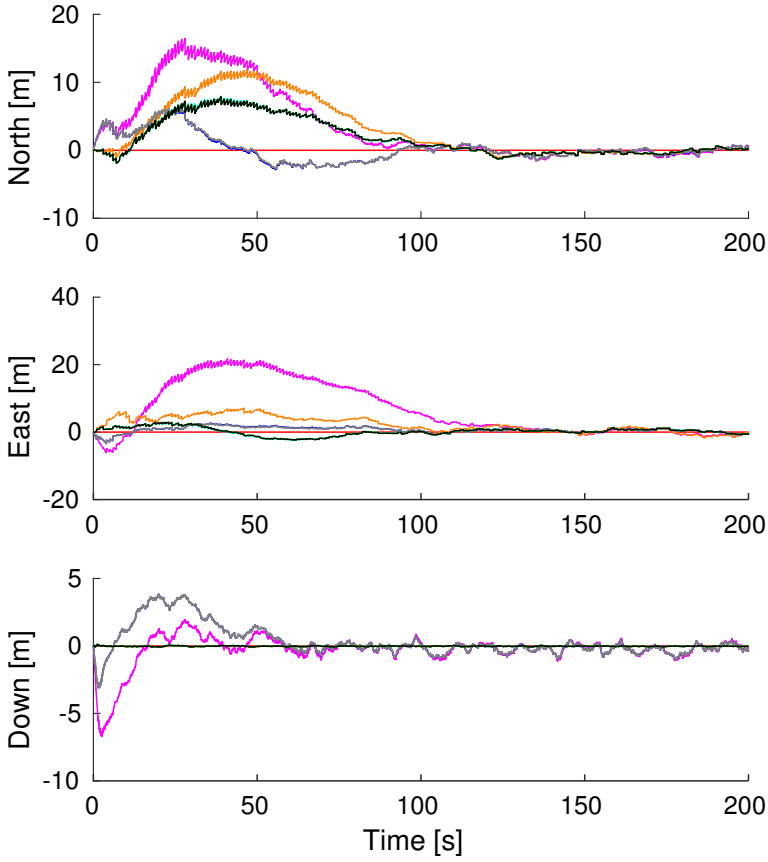

Figure 6.3: The transient of the NED position estimation errors in one of the simulations. The black, green, and cyan curves are overlapping, and so are the gray and blue.

Figure 6.4: The sensor platform with hydroacoustic transducers (on rods), Qualisys markers (reflective balls), and an underwater housing. The blue light is emitted from the OQUS camera system in order to better detect the reflective markers.

- The IMU used in the experiments, an ADIS16485, does not contain a magnetometer. Therefore, measurements from 3 additional transponders was used in order to provide yaw information to the attitude estimator. Also, for ease of implementation, a standard MEKF was employed, using accelerometer and the acoustics as reference vector measurements.
- No pressure sensor was available, so the vertical position output from the Qualisys camera system was used instead. Onto this signal, a white noise $w_d \sim \mathcal{N}(0, 0.05^2)$ was added.
- The acoustic system provided range measurements. From this, range difference measurements were calculated by subtraction. Simple outlier rejection was employed to prevent corruption of the estimates. This is described in Section 3.2.

The sensor platform was a $0.5 \times 0.5 \times 0.5m$ aluminum frame onto which an underwater housing with an IMU was fastened, seen in Figure 6.4. The transceiver positions were

$$p^b_{bc_1} = [0.78, 0.27, 0.26]m,\ p^b_{bc_2} = [0.45, -0.58, -0.28]m$$
$$p^b_{bc_3} = [-0.44, -0.23, 0.16]m,\ p^b_{bc_4} = [-0.44, 0.27, -0.25]m$$

and the transponder position $p^n_{nt} = [-2.11, 1.92, -0.76]m$. Acoustic measurements were retrieved with $1Hz$, while IMU and depth measurements were re-

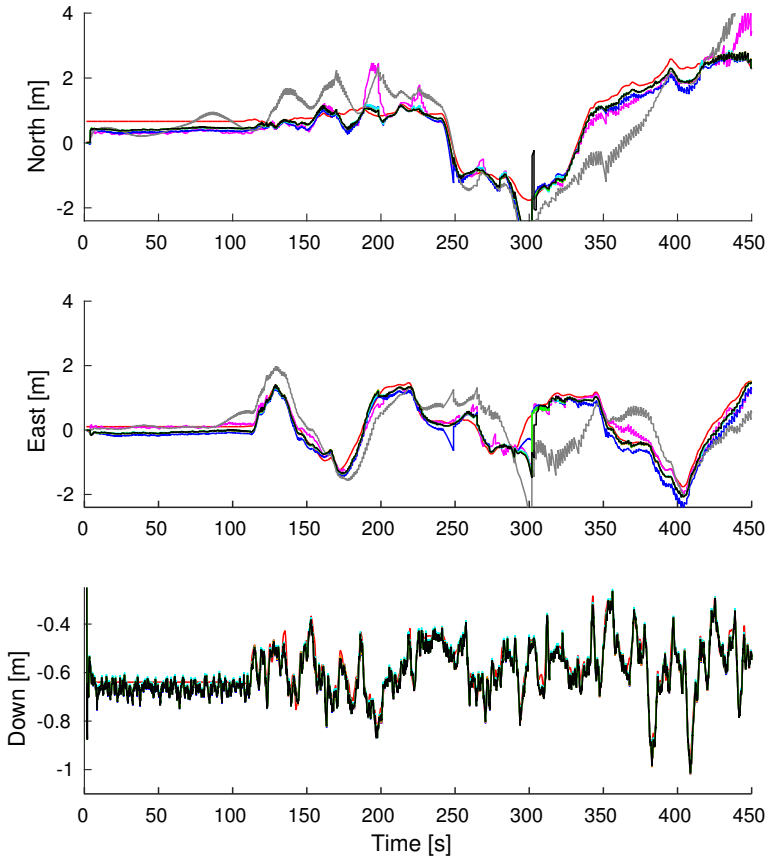

Figure 6.5: NED position estimates from experimental data.

trieved with $100Hz$ and $5Hz$, respectively. The tuning parameter standard deviations of the 3SFs and MEKF were $\sigma_y = 0.2m$, $\sigma_\partial = 0.1m$, $\sigma_{acc} = 0.034m/s^2$, $\sigma_{ars} = 0.0021rad/s$, and $\sigma_{\Delta p} = 0.1m$, where $\sigma_{\Delta p}$ represents the noise of the acoustic reference vector measurement used for the MEKF discussed above.

From Figure 6.5, we see that all filters except the loosely coupled filter 5 successfully tracked the true trajectory except about 300 seconds into the experiments. This was due to range measurement dropouts which resulted in a period of dead-reckoning. It is likely that filter 5 struggled because of small undetected outliers that greatly affected the noise sensitive calculation of $\underline{p}^n_{nb}$. Table 6.2 suggests that the body-fixed stage 2 filters, i.e. filter 2 and 3, performs worse than the NED stage 2 filter, i.e. filter 4. This confirms the conclusion drawn from the simulation study.

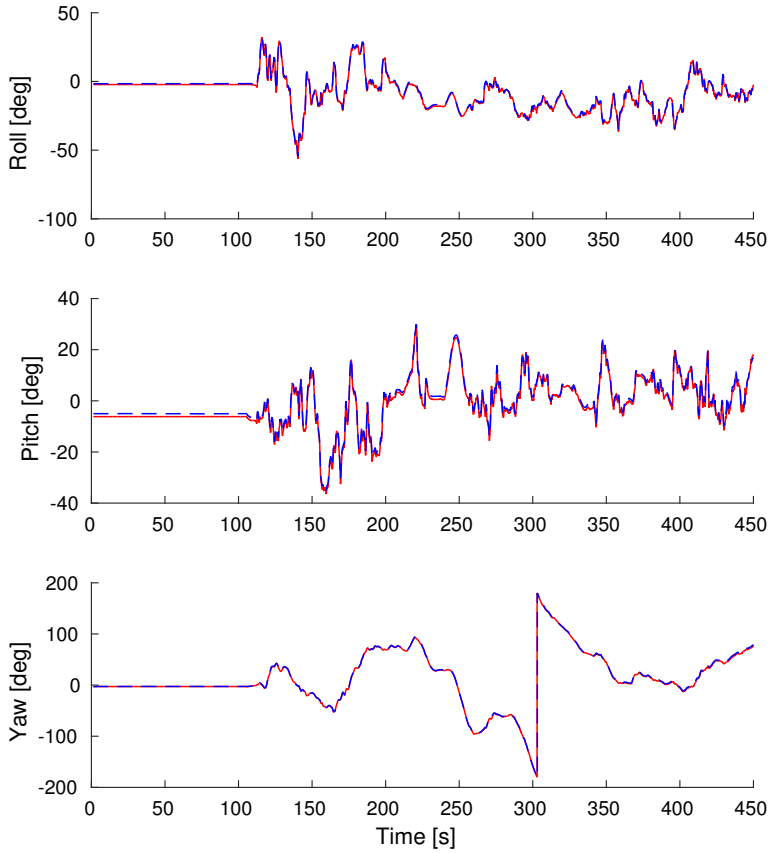

Figure 6.6: Euler angles in experiments. The red curve is the ground truth trajectory from the camera system, and the blue dashed line is the MEKF estimate.

Table 6.2: MAE values from the experiments.

Est.	XY [m]	Z [m]
2)	0.3979	0.0269
3)	0.4030	0.0274
4)	0.2746	0.0232
5)	0.9384	0.0266
6)	0.2734	0.0269
7)	0.2702	0.0266
8)	0.2763	0.0266

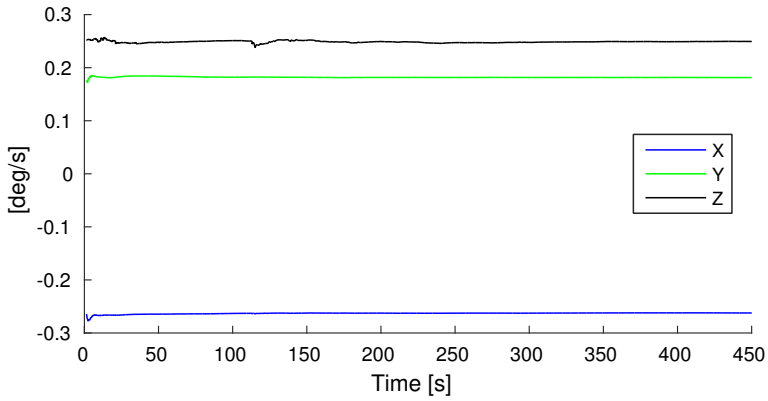

Figure 6.7: ARS bias in experiments.

Also, filter 4 performs equally well as the linearized filters, i.e. filter 6–8. This was also seen in the simulation study. Here, however, the distance between vehicle and transponder was much shorter than in the simulation study. This indicates that neglecting the noise terms in the denominators of (6.16) is justified also for short distances. That the performance of the body-fixed and NED linearized filters were similar, was expected, as the distance to the transponder was small. Figure 6.6–6.7 show satisfying attitude and ARS bias estimation in the experiments.

6.6 Conclusion

In this chapter, four different GES 3SFs for inertial navigation aided by an iSBL network was developed. Two of the filters formulated the state in the body-fixed coordinate frame, while the two other used the NED coordinate frame. The stability of all filters were analyzed and found to be GES. A simulation study was conducted, showing the NED frame to be a better frame of reference for estimation. The reason for this was two-fold. First, the NED formulated filters incorporated depth measurements better than the body-fixed ones, yielding lower vertical MAE. Secondly, the horizontal MAE was significantly smaller for the NED formulated filters than for the body-fixed ones. This was likely due to a more noisy kinematic model.

One of the second stage NED filters showed similar performance as the third stage filters and the EKF, meaning EKF-like performance can be achieved with global stability and half the computational cost of the full 3SF.

Further work should look into how the process noise matrix $G_x(x)$ can be modeled

more accurately for higher performance. This might give better performance of the body-fixed filters.

This chapter aimed at answering the research questions "*Can the iSBL network reduce the required installed infrastructure to one transponder while yielding adequate estimation accuracy? Furthermore, can the XKF method be applied to this problem to give global stability of the solution?*". A solution for position estimation with only one transponder has been achieved, and the XKF method has been applied in order to achieve global stability. Therefore, the research goals have been achieved.

Appendix

6.A Choice of $G_x(0)$

For the body-fixed filters, the choice for the system noise matrix

$$G_x(0) = \begin{bmatrix} 0_{3\times3} & 0_{3\times3} \\ 0_{3\times3} & -I_3 \end{bmatrix} \tag{6.42}$$

is made for two reasons:

1. To show controllability
2. To enhance performance

1. The controllability co-distribution (4.27) of $(A_x(z), G_x(x))$ is

$$\mathrm{d}\mathcal{C} = \begin{bmatrix} -S(p^b_{tb}) & 0_{3\times3} & S(\omega^b_{nb,m} - b^b_{ars})S(p^b_{tb}) - 2S(v^b_{nb}) & -I_3 \\ -S(v^b_{nb}) & -I_3 & S(\omega^b_{nb,m} - b^b_{ars})S(v^b_{nb}) - S(\dot{v}^b_{nb}) & S(\omega^b_{nb,m} - b^b_{ars}) \end{bmatrix},$$

the full rank of which can only be assumed. The choice (6.42), however, yields

$$\mathrm{d}\mathcal{C} = \begin{bmatrix} 0_{3\times3} & 0_{3\times3} & 0_{3\times3} & -I_3 \\ 0_{3\times3} & -I_3 & 0_{3\times3} & S(\omega^b_{nb,m} - b^b_{ars}) \end{bmatrix}$$

which can be shown to have full rank by

$$\begin{aligned} \mathrm{rank}(\mathrm{d}\mathcal{C}) &= \mathrm{rank}(\mathrm{d}\mathcal{C}\mathrm{d}\mathcal{C}^\top) \\ &= \begin{bmatrix} I_3 & S(\omega^b_{nb,m} - b^b_{ars}) \\ -S(\omega^b_{nb,m} - b^b_{ars}) & S(\omega^b_{nb,m} - b^b_{ars})S(\omega^b_{nb,m} - b^b_{ars})^\top + I_3 \end{bmatrix} \end{aligned}$$

$$\begin{bmatrix} x_1^\top & x_2^\top \end{bmatrix} \mathrm{d}\mathcal{C}\mathrm{d}\mathcal{C}^\top \begin{bmatrix} x_1 \\ x_2 \end{bmatrix} = x_1^\top x_1 + x_3^\top x_3 + x_2^\top x_2 > \ 0 \ \forall x_1^\top x_1 + x_2^\top x_2 \neq 0$$

where $x_3 = S(\omega^b_{nb,m} - b^b_{ars})^\top x_2$.

2. The most important reason for the choice (6.42) is the enhanced performance. When the distance between transponder and vehicle $\|p^b_{tb}\|_2$ is large, this causes a large build-up of uncertainty in the covariance estimate P_x. This increases the effect of the measurement, which seems to have a detrimental effect on the estimation performance. Therefore, the choice (6.42) is advised, along with increasing the Q_x-matrix. The latter accounts for the build-up of P_x that was lost.

6.B Proof of Lemma 6.4.1

Theorem 6.O12 in Chen [76] proves that the pair $(A(t), D(t))$ is UCO if the observability co-distribution (4.26) formed by $A(t)$ and $D(t)$ has full rank. We define the placeholder matrix $\mathcal{D}(t) \in \{C_x, C_\chi(\check{z}), D_x(\check{x}), D_\chi(\check{\chi}, \check{z}), H_x(\bar{x}), H_\chi(\bar{\chi}, \check{z})\}$ and note its general form $\mathcal{D} = [\mathcal{D}_p(t), 0_{M\times 3}]$ where $\mathcal{D}_p(t) \in \mathbb{R}^{M\times 3}$. The top $2M$ rows of the observability co-distributions are

$$\mathrm{d}\mathcal{O} = \begin{bmatrix} \mathcal{D}_p(t) & 0_{M\times 3} \\ \star & \mathcal{D}_p(t) \end{bmatrix}$$

where $\star$ denotes an arbitrary matrix of appropriate size. From Theorem 4.2 of Meyer [77], it follows that if $\mathcal{D}_p(t)$ has full rank, then $\mathrm{d}\mathcal{O}$ has full rank. The rank of $\mathcal{D}_p(t)$ is full for all systems under Assumption 6.4.2, and thus, all systems are UCO.

Theorem 6.12 in Chen [76] proves that the pair $A(t), G(t)$ is UCC if the controllability co-distribution (4.27) formed by $A(t)$ and $G(t)$ has full rank. This was proven for $(A_x(z,t), G_x(0))$ in Appendix 6.A, and the proof for $(A_\chi, G_\chi(z))$ is similar.

6.C Proof of Proposition 6.4.1

The origin $z - \check{z} = 0$ of the error dynamics Σ_z is GES under Proposition 4.2.1.

Notice that in the noise-free case when $\check{z} = z$, we have $\check{p}^b_{tb} \equiv p^b_{tb}$ and $\check{p}^n_{nb} \equiv p^n_{nb}$, and consequently, $\bar{\xi}_{xi} = 0$ and $\bar{\xi}_{\chi i} = 0$, $i \in \{1, 2\}$. In this case and under Lemma 6.4.1, the equilibrium points $\tilde{\bar{x}}_i = 0$ and $\tilde{\bar{\chi}}_i = 0$ of the error dynamics $\bar{\Sigma}_{xi}$ and $\bar{\Sigma}_{\chi i}$, respectively for $i \in \{1, 2\}$, are GES as proven by Anderson [79].

6.C.1 Cascade Proof *(separated for reference)*

When $\check{z} \neq z$, $\bar{\xi}_{xi}$ and $\bar{\xi}_{\chi i}$ are bounded by (6.37) and (6.38), respectively. Now, the rest of the proof follows from Theorem 2.1 and Proposition 2.3 of Loria and Panteley [80] and Proposition 4.2.1.

Chapter 7

Position and Attitude Estimation Using Inverted Short Baseline Network

This chapter is based on Stovner and Johansen [69], in which a 3SF for joint position and attitude estimation using an iSBL set-up with two or more transponders is developed. It is shown that with multiple transponders, the magnetic field measurements often used in attitude estimation can be replaced while GES estimation of both position and attitude is achieved. The hydroacoustic set-up can be seen in Figure 2.5.

The notation from Chapter 6 is slightly altered in order to accommodate several transponders. We define the translational state vector

$$x \triangleq \begin{bmatrix} p^b_{t_1 b} \\ \vdots \\ p^b_{t_N b} \\ v^b_{nb} \end{bmatrix} \tag{7.1}$$

where $p^b_{t_i b}$ is the position of the vehicle relative to transponder $t_i, i \in (1, N)$.

Similarly, we extend the notation of (6.1) to

$$\rho_{ij} = \|p^n_{nb} - p^n_{nt_i} + R^n_b p^b_{bc_j}\|_2 \tag{7.2a}$$
$$= \|p^b_{t_i b} + p^b_{bc_j}\|_2. \tag{7.2b}$$

This allows us to write the range and range difference measurement equations

$$y_{iM} = h_{iM}(x) \triangleq \rho_{iM} + \epsilon_{y,iM} \tag{7.3a}$$
$$\partial y_{ij} = h_{ij}(x) \triangleq \rho_{ij} - \rho_{iM} + \epsilon_{\partial,ij}, \tag{7.3b}$$

which is concatenated for $j \in (1, M)$ and $i \in (1, N)$

$$y_i = \begin{bmatrix} \partial y_{i1} \\ \vdots \\ \partial y_{iM-1} \\ y_{iM} \end{bmatrix}, \; h_i = \begin{bmatrix} h_{i1} \\ \vdots \\ h_{iM} \end{bmatrix}, \; \epsilon_{\partial,i} = \begin{bmatrix} \epsilon_{\partial,i1} \\ \vdots \\ \epsilon_{\partial,iM-1} \end{bmatrix}, \; \epsilon_{y,i} = \begin{bmatrix} \epsilon_{\partial,i} \\ \epsilon_{y,iM} \end{bmatrix}$$
$$y = \begin{bmatrix} y_1 \\ \vdots \\ y_N \end{bmatrix}, \; h = \begin{bmatrix} h_1 \\ \vdots \\ h_N \end{bmatrix}, \; \epsilon_y = \begin{bmatrix} \epsilon_{y,1} \\ \vdots \\ \epsilon_{y,N} \end{bmatrix}.$$

Due to the change in the state vector, the state dynamics must be changed accordingly:

$$\dot{x} = A(t, z)x + B(z)u(t) + G(x)\epsilon_x, \tag{7.4}$$

where

$$A(t, z) = \begin{bmatrix} -S(\omega^b_{ars} - b^b_{ars}) & \cdots & 0_{3\times3} & I_3 \\ \vdots & \ddots & \vdots & \vdots \\ 0_{3\times3} & \cdots & -S(\omega^b_{ars} - b^b_{ars}) & I_3 \\ 0_{3\times3} & \cdots & 0_{3\times3} & -S(\omega^b_{ars} - b^b_{ars}) \end{bmatrix}$$
$$G(x) = \begin{bmatrix} -S(p^b_{t_1 b}) & 0_3 \\ \vdots & \vdots \\ -S(p^b_{t_N b}) & 0_3 \\ -S(v^b_{nb}) & -I_3 \end{bmatrix}, \; B(z) = \begin{bmatrix} 0_{3N\times3} & 0_{3N\times3} \\ I_3 & R^{n\top}_b \end{bmatrix},$$

and ϵ_x and $u(t)$ are the the same as in Chapter 6.

In this chapter, the attitude is estimated by the attitude estimator (4.7). The magnetic field information previously used for attitude estimation is in this chapter replaced by the known and estimated vectors

$$y_2^n = \frac{p_{t_i t_N}^n}{\|p_{t_i t_N}^n\|_2} \tag{7.5a}$$

$$y_2^b = \frac{p_{t_i b}^b - p_{t_N b}^b}{\|p_{t_i b}^b - p_{t_N b}^b\|_2} = \frac{p_{t_i t_N}^b}{\|p_{t_i t_N}^b\|_2}, \tag{7.5b}$$

respectively. Gravity provides the other attitude measurement, i.e..

$$y_1^n = \frac{-g^n}{\|g^n\|_2},\ y_1^b = \frac{f_{nb,m}^b}{\|f_{nb,m}^b\|_2}.$$

The structure of the 3SF can be seen in Figure 7.1. On the left-hand side, the same stages of position estimation as in Chapter 6 are seen. New in this chapter is the attitude estimator present in each stage, shown on the right-hand side of Figure 7.1. Body-fixed position estimates that facilitate the calculation of the vector (7.5b) are available in each stage. Since the accuracy of these are expected to increase for each stage, it is reasonable to implement an attitude estimator in each stage as well. This way, the attitude is estimated from the best available body-fixed reference vector estimate.

7.1 Stage 1: Algebraic Transformation

7.1.1 3 Receivers

The AT for all measurements from transponder i is identical to the AT for the single transponder in (6.10). With the exact same derivation, we achieve the linear measurement model

$$Y_{x,i} + l_M r_{1,i} = C_x x + \epsilon_{Y,i}, \tag{7.6}$$

which can be concatenated to

$$Y = Cx + \epsilon_Y, \tag{7.7}$$

where

$$Y = \begin{bmatrix} Y_{x,1} + l_M r_{x1,1} \\ \vdots \\ Y_{x,N} + l_M r_{x1,N} \end{bmatrix},\ C = \begin{bmatrix} C_x \\ \vdots \\ C_x \end{bmatrix},\ \epsilon_Y = \begin{bmatrix} \epsilon_{Y,1} \\ \vdots \\ \epsilon_{Y,N} \end{bmatrix}.$$

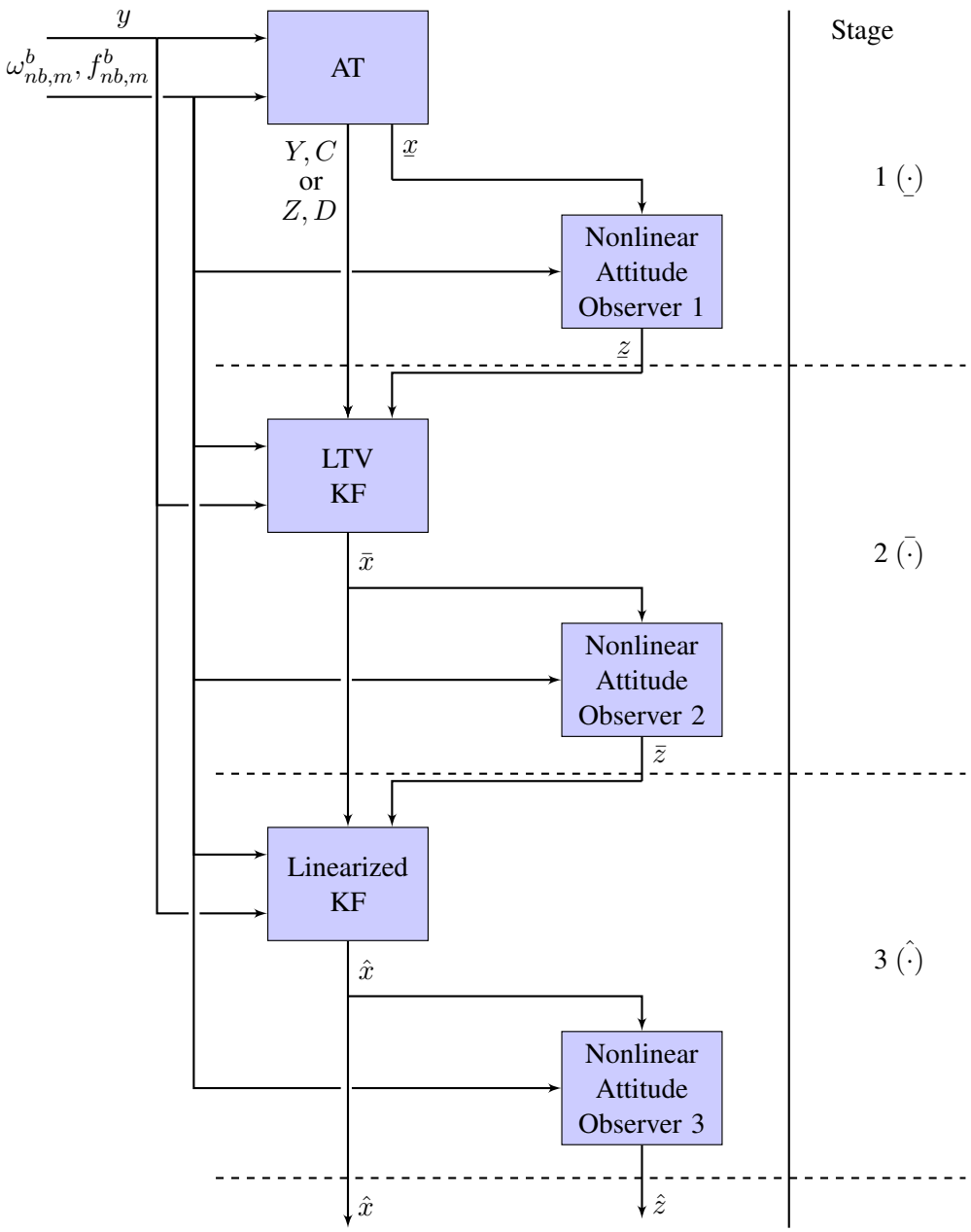

Figure 7.1: In this figure, the three different stages of the body-fixed 3SF are depicted. The stage number and the associated notation can be seen on the right-hand side.

An estimate of $p^b_{t_i b}$ to be used for attitude estimation is found as

$$\underline{p}^b_{t_i b} = r_{1,i} c_x + w_i, \tag{7.8}$$

where $c_x = C^{\dagger}_{xp} l_M$ and $w_i = C^{\dagger}_{xp} Y_{x,i}$, where $r_{1,i}$ is found by solving the ambiguity (6.9).

7.1.2 ≥ 4 Receivers

Similarly as above, the AT from transponder i to 4 or more receivers on the vehicle is identical to that described in Section 6.1.3. We generalize (6.14) for N transponders

$$Z = D(\underline{x})x + \bar{\varphi}(x - \underline{x}) + \epsilon_y, \tag{7.9}$$

where

$$Z = \begin{bmatrix} Z_{x,1} \\ \vdots \\ Z_{x,N} \end{bmatrix}, \; D(\underline{x}) = \begin{bmatrix} D'_{x,1} \\ H_{x,1M}(\underline{p}^b_{t_1 b}) \\ \vdots \\ D'_{x,N} \\ H_{x,NM}(\underline{p}^b_{t_N b}) \end{bmatrix}, \; \bar{\varphi}(x - \underline{x}) = \begin{bmatrix} \bar{\varphi}_x(p^b_{t_1 b} - \underline{p}^b_{t_1 b}) \\ \vdots \\ \bar{\varphi}_x(p^b_{t_N b} - \underline{p}^b_{t_N b}) \end{bmatrix}.$$

The linearization point is $\underline{x} = [{\underline{p}^b_{t_1 b}}^{\top}, ..., {\underline{p}^b_{t_N b}}^{\top}, 0, 0, 0]^{\top}$, where $\underline{p}^b_{t_i b} = {D'_{x,1}}^{\dagger} Z'_{x,i}$.

7.1.3 Attitude Estimator

Now, the attitude estimator in Section 4.2 with variables $\underline{R}^n_{\underline{b}}$, $\underline{b}^b_{ars}$, $\underline{\sigma}$, $\underline{k}_I$, and $\underline{K}_p$, and reference vector (7.5) with $\underline{p}^b_{t_i b}, i \in (1, N)$ is used to produce the attitude estimate $\underline{z} = (R^n_{\underline{b}}, \underline{b}^b_{ars})$, where $R^n_{\underline{b}}$ is the matrix $\underline{R}^n_{\underline{b}}$ projected onto SO(3). Its estimation error is denoted $\tilde{\underline{z}} = (R^n_b - R^n_{\underline{b}}, b^b_{ars} - \underline{b}^b_{ars})$ and its error dynamics is

$$\Sigma_{\underline{z}} : \; \dot{\tilde{\underline{z}}} = \dot{\tilde{\underline{z}}}^{\star} + \underline{\xi}_z(p^b_{t_1 b}, ..., p^b_{t_N b}, \underline{p}^b_{t_1 b}, ..., \underline{p}^b_{t_N b}) \tag{7.10}$$

where $\dot{\tilde{\underline{z}}}^{\star}$ is the error dynamics provided exact position estimates, i.e., $\underline{p}^b_{t_i b} = p^b_{t_i b}$ for $i \in (1, N)$, and $\underline{\xi}_z$ is the error caused by inexact position estimates. Naturally, $\underline{\xi}_z = 0$ when $\underline{p}^b_{t_i b} = p^b_{t_i b} \; \forall \; i \in (1, N)$.

7.2 Stage 2: Linear Time-Varying Kalman Filter

7.2.1 3 Receivers

The second stage estimator for three receivers is defined as

$$\dot{\bar{x}}_1 \triangleq A(t,\underline{z})\bar{x}_1 + B(\underline{z})u(t) + \bar{K}(t)(Y - C\bar{x}_1) \tag{7.11}$$

where $\bar{K}_1(t) = \bar{P}_1(t)C^\top \mathcal{R}_Y^{-1}$ and $\bar{P}_1(t)$ is the covariance estimate. The covariance estimate is updated by (1.3c) inserted $A(\underline{z},t)$, C, $G(\bar{x}_1)$, $\mathcal{Q}$ given by

$$\mathcal{Q} = \begin{bmatrix} \sigma_{ars}^2 I_{3N} & 0_{3N\times 3} \\ 0_{3\times 3N} & \sigma_{acc}^2 I_3 \end{bmatrix} \tag{7.12}$$

and $\mathcal{R}_Y$ given by

$$\mathcal{R}_Y = \begin{bmatrix} \mathcal{R}_{Y,1} & \cdots & 0_{M\times M} \\ \vdots & \ddots & \vdots \\ 0_{M\times M} & \cdots & \mathcal{R}_{Y,N} \end{bmatrix}, \tag{7.13}$$

where $\mathcal{R}_{Y,i}$ for each $i \in \{1, N\}$ equals (6.21). The initial covariance estimate is $\bar{P}_1(0) = \bar{P}_{10}$.

Define the estimation error $\tilde{\bar{x}}_1 \triangleq x - \bar{x}_1$. Subtracting (7.11) from (7.4), inserting (7.7), and neglecting noise yield the error dynamics

$$\bar{\Sigma}_{x1}: \ \dot{\tilde{\bar{x}}}_1 = (A(\underline{z},t) - \bar{K}_1(t)C)\tilde{\bar{x}}_1 + \bar{\xi}_1(z,\underline{z},x,t), \tag{7.14}$$

where $\bar{\xi}_1(z,\underline{z},x,t) = (A(z,t) - A(\underline{z},t))x + (B(z) - B(\underline{z}))u(t)$.

7.2.2 ≥ 4 Receivers

The second stage estimator for four or more receivers is defined as

$$\dot{\bar{x}}_2 \triangleq A(t,\underline{z})\bar{x}_2 + B(\underline{z})u(t) + \bar{K}(t)(Y - D(\underline{x})\bar{x}_2) \tag{7.15}$$

where $\bar{K}_2(t) = \bar{P}_2(t)D^\top(\underline{x})\mathcal{R}^{-1}$ and $\bar{P}_2(t)$ is the covariance estimate. The covariance estimate is updated by (1.3c) inserted $A(\underline{z},t)$, $D(\underline{x})$, $G(\bar{x}_2)$, $\mathcal{Q}$

$$\mathcal{R} = \begin{bmatrix} \mathcal{R}' & \cdots & 0_{M\times M} \\ \vdots & \ddots & \vdots \\ 0_{M\times M} & \cdots & \mathcal{R}' \end{bmatrix}, \tag{7.16}$$

and $\mathcal{R}'$ is given by (6.28). The initial covariance estimate is $\bar{P}_2(0) = \bar{P}_{20}$

Define the estimation error $\tilde{\bar{x}}_2 \triangleq x - \bar{x}_2$. Subtracting (7.15) from (7.4), inserting (7.7), and neglecting noise yield the error dynamics

$$\bar{\Sigma}_{x2}: \ \dot{\tilde{\bar{x}}}_2 = (A(\underline{z}, t) - \bar{K}_2(t)C)\tilde{\bar{x}}_2 + \bar{\xi}_2(z, \underline{z}, x, t), \tag{7.17}$$

where $\bar{\xi}_2(z, \underline{z}, x, t) = (A(z,t) - A(\underline{z}, t))x + (B(z) - B(\underline{z}))u(t) + \bar{K}_1(t)\bar{\varphi}(x - \underline{x})$.

7.2.3 Attitude Estimator

The attitude estimator in Section 4.2 with variables $\bar{R}^n_{\bar{b}}$, $\bar{b}^{\bar{b}}_{ars}$, $\bar{\sigma}$, $\bar{k}_I$, and $\bar{K}_p$, and reference vector (7.5) with $\bar{p}^b_{t_i b}, i \in (1, N)$ is used to produce the attitude estimate $\bar{z} = (R^n_{\bar{b}}, \bar{b}^{\bar{b}}_{ars})$, where $R^n_{\bar{b}}$ is the matrix $\bar{R}^n_{\bar{b}}$ projected onto $SO(3)$. Its estimation error is denoted $\tilde{\bar{z}} = (R^n_b - R^n_{\bar{b}}, b^b_{ars} - \bar{b}^{\bar{b}}_{ars})$ and its error dynamics is

$$\bar{\Sigma}_z: \ \dot{\tilde{\bar{z}}} = \dot{\tilde{\bar{z}}}^\star + \bar{\xi}_z(p^b_{t_1 b}, ..., p^b_{t_N b}, \bar{p}^b_{t_1 b}, ..., \bar{p}^b_{t_N b}) \tag{7.18}$$

where $\dot{\tilde{\bar{z}}}^\star$ is the error dynamics provided exact position estimates, i.e., $\bar{p}^b_{t_i b} = p^b_{t_i b}$ for $i \in (1, N)$, and $\bar{\xi}_z$ is the error caused by inexact position estimates. Naturally, $\bar{\xi}_z = 0$ when $\bar{p}^b_{t_i b} = p^b_{t_i b} \ \forall \ i \in (1, N)$. The estimates $\bar{p}^b_{t_i b}$ come from either $\bar{x}_1$ or $\bar{x}_2$.

7.3 Stage 3: Linearized Kalman Filter

The thirds stage is identical for both second stage estimators. Denote therefore $\bar{x} \in \{\bar{x}_1, \bar{x}_2\}$. Using the linearization of iSBL measurements from a single transponder (6.32), helps us find

$$h(x) = h(\bar{x}) + H(\bar{x})(x - \bar{x}) + \varphi(x - \bar{x}), \tag{7.19}$$

where $\varphi(x - \bar{x})$ are higher order terms, $\varphi(0) = 0$, and

$$H(x) = \begin{bmatrix} H_1(x) & \cdots & 0_{M\times 3} & 0_{M\times 3} \\ \vdots & \ddots & \vdots & \vdots \\ 0_{M\times 3} & \cdots & H_N(x) & 0_{M\times 3} \end{bmatrix}, \ H_i(x) = \begin{bmatrix} H_{i1}(x) \\ \vdots \\ H_{iM} \end{bmatrix}$$

$$H_{ij} = \left[\frac{(p^b_{t_i b} - p^b_{bc_j})^\top}{\|p^b_{t_i b} - p^b_{bc_j}\|_2} - \frac{(p^b_{t_i b} - p^b_{bc_M})^\top}{\|p^b_{t_i b} - p^b_{bc_M}\|_2} \right], \ j \in (1, M-1), \ H_{iM} = \left[\frac{(p^b_{t_i b} - p^b_{bc_M})^\top}{\|p^b_{t_i b} - p^b_{bc_M}\|_2} \right].$$

Now, the third stage estimator is defined by

$$\dot{\hat{x}} = A(t, \bar{z})\hat{x} + B(\bar{z})u(t) + \hat{K}(t)(y - h(\bar{x}) - H(\bar{x})(\hat{x} - \bar{x})), \tag{7.20}$$

where $\hat{K}(t) = \hat{P}(t)C^\top \mathcal{R}^{-1}$ and $\hat{P}(t)$ is the covariance estimate. The covariance estimate is updated by (1.3c) inserted $A_x(\check{z}, t)$, $H(\bar{x})$, $G_x(\bar{x})$, $\mathcal{Q}$ and $\mathcal{R}$ given by

$$\mathcal{R} = \begin{bmatrix} \mathcal{R}_1 & \cdots & 0_{M\times M} \\ \vdots & \ddots & \vdots \\ 0_{M\times M} & \cdots & \mathcal{R}_N \end{bmatrix}, \tag{7.21}$$

where $\mathcal{R}_i$ for each $i \in (1, N)$ is found by (6.28). The initial covariance estimate is $\hat{P}(0) = \hat{P}_0$.

Define the estimation error $\tilde{x} \triangleq x - \hat{x}$. Subtracting (7.20) from (7.4), inserting (7.19), and neglecting noise yield the error dynamics

$$\hat{\Sigma}_x : \ \dot{\tilde{x}} = (A(\bar{z}, t) - \hat{K}(t)H(\bar{x}))\tilde{x} + \hat{\xi}_x(x, z, \bar{x}, \bar{z}, t), \tag{7.22}$$

where

$$\hat{\xi}_x(x, z, \bar{x}, \bar{z}, t) = (A(z, t) - A(\bar{z}, t))x + (B(z) - B(\bar{z}))u(t) - \hat{K}(t)\varphi(\tilde{\bar{x}}).$$

The attitude estimator in Section 4.2 with variables $\hat{R}^n_{\hat{b}}$, $\hat{b}^{\hat{b}}_{ars}$, $\hat{\sigma}$, $\hat{k}_I$, and $\hat{K}_p$, and reference vector (7.5) with $\hat{p}^b_{t_i b}, i \in (1, N)$ is used to produce the attitude estimate $\hat{z} = (R^n_{\hat{b}}, \hat{b}^{\hat{b}}_{ars})$, where $R^n_{\hat{b}}$ is the matrix $\hat{R}^n_{\hat{b}}$ projected onto SO(3). Its estimation error is denoted $\tilde{z} = (R^n_b - R^n_{\hat{b}}, b^b_{ars} - \hat{b}^{\hat{b}}_{ars})$ and its error dynamics is

$$\hat{\Sigma}_z : \ \dot{\tilde{z}} = \dot{\tilde{z}}^\star + \hat{\xi}_z(p^b_{t_1 b}, ..., p^b_{t_N b}, \hat{p}^b_{t_1 b}, ..., \hat{p}^b_{t_M b}) \tag{7.23}$$

where $\dot{\tilde{z}}^\star$ is the error dynamics provided exact position estimates, i.e., $\hat{p}^b_{t_i b} = p^b_{t_i b}$ for $i \in (1, N)$, and $\hat{\xi}_z$ is the error caused by inexact position estimates. Naturally, $\hat{\xi}_z = 0$ when $\hat{p}^b_{t_i b} = p^b_{t_i b}\ \forall\ i \in (1, N)$.

7.4 Stability Analysis

The stability analysis of the body-fixed three-stage filter is conducted as follows. First, the stability of the estimation errors $\tilde{\underline{z}}$, $\tilde{\bar{z}}$, and $\tilde{z}$ are collectively analyzed provided exact transponder baseline estimates $\underline{p}^b_{t_i b}$, $\bar{p}^b_{t_i b}$, and $\hat{p}^b_{t_i b}$, respectively. Second, the LTV and linearized KFs are analyzed. Lastly, the stability of the entire cascade is analyzed. This is a deterministic analysis, meaning we analyze the stability without noise. Before the analysis, we need to state two assumptions:

Assumption 7.4.1. *There are at least $M \geq 3$ non-collinear transceivers on the vehicle.*

Assumption 7.4.2. *There are at least $M \geq 4$ non-coplanar transceivers on the vehicle.*

Assumption 7.4.3. *There are at least $N \geq 2$ transponders in the vehicle's surroundings, and the baseline between them is not parallel with the local gravitational field.*

Proposition 7.4.1. *Suppose for the attitude estimators in stage 1, 2, and 3 that K_p is symmetric and positive definite, $k_I > 0$, and $\sigma \geq 1$. Now, we have in the noise-free case that the equilibrium points $\tilde{\underline{z}} = 0$, $\tilde{\bar{z}} = 0$, and $\tilde{z} = 0$ of the error dynamics $\dot{\tilde{\underline{z}}}^\star$, $\dot{\tilde{\bar{z}}}^\star$, and $\dot{\tilde{z}}^\star$ are GES under Assumption 7.4.3.*

Proof. The proof follows directly from Grip et al. [52]. □

Proposition 7.4.2. *The systems $(A(t, \underline{z}), C, G(\bar{x}))$ and $(A(t, \bar{z}), H(\bar{x}), G(\bar{x}))$ are UCO and UCC under Assumption 7.4.1 and $(A(t, \underline{z}), D(\underline{x}), G(\bar{x}))$ is UCO and UCC under Assumption 7.4.2.*

Proof. The proof is similar to that of Proposition 6.4.1 in Appendix 6.B. □

Proposition 7.4.3. *Suppose the same as in Proposition* (7.4.1)*, that Assumption 7.4.3 is true, and that there is no noise. Now, we have that the equilibrium points $\tilde{\underline{z}} = 0$, $\tilde{\bar{x}}_k = 0$, $\tilde{\bar{z}} = 0$, $\tilde{x} = 0$, and $\tilde{z} = 0$ of the error dynamics cascade $\underline{\Sigma}_z$–$\bar{\Sigma}_{xk}$–$\bar{\Sigma}_z$–$\hat{\Sigma}_x$–$\hat{\Sigma}_z$ for $k \in \{1, 2\}$ are GES under Assumption 7.4.1 for $k = 1$ and 7.4.2 for $k = 2$.*

Proof. The proof is given in Appendix 7.A □

7.5 Results

Here, we denote the ATs in Section 7.1.1 and 7.1.2 by AT1 and AT2, respectively; the LTV KFs in Section 7.2.1 and 7.2.2 by LTV KF1 and LTV KF2, respectively; and the linearized KF with inputs from either LTV KF1 or LTV KF2 as Lin KF. A standard EKF based on the same model as the linearized KF is used as benchmark.

7.5.1 Simulations

In the simulations, $M = 4$ receivers and $N = 2$ transponders are assumed:

$$p^b_{bc_1} = \begin{bmatrix} 0.5 \\ 0.5 \\ -0.5 \end{bmatrix} m,\ p^b_{bc_2} = \begin{bmatrix} 0.5 \\ -0.5 \\ 0.5 \end{bmatrix} m,\ p^b_{bc_3} = \begin{bmatrix} -0.5 \\ 0.5 \\ 0.5 \end{bmatrix} m,\ p^b_{bc_4} = \begin{bmatrix} 0.5 \\ 0.5 \\ 0.5 \end{bmatrix} m,$$

$$p^n_{nt_1} = \begin{bmatrix} -50 \\ -50 \\ 0 \end{bmatrix} m,\ p^n_{nt_1} = \begin{bmatrix} 50 \\ 50 \\ 0 \end{bmatrix} m.$$

The initial conditions are

$$p^n_{nb}(0) = \begin{bmatrix} 0 \\ 0 \\ 0 \end{bmatrix},\ v^n_{nb}(0) = \begin{bmatrix} 0 \\ 0 \\ 0 \end{bmatrix},\ R^n_b(0) = I_3,$$

the ARS bias is $b^b_{ars} = [0.012, -0.021, 0.014]^\top$, and the noise standard deviations are

$$\sigma_{acc} = 0.01\frac{m}{s^2} \qquad \sigma_{ars} = 0.01\frac{rad}{2} \qquad \sigma_{mag} = 0.01$$
$$\sigma_y = 1m \qquad \sigma_\partial = 0.01m.$$

The initial state estimates are all found from the following values

$$\check{p}^n_{nb} = \begin{bmatrix} 0 \\ 0 \\ 0 \end{bmatrix},\ \check{v}^n_{nb} = \begin{bmatrix} 0 \\ 0 \\ 0 \end{bmatrix},\ \begin{bmatrix} \check{\phi} \\ \check{\theta} \\ \check{\psi} \end{bmatrix} = \begin{bmatrix} 0^\circ \\ 0^\circ \\ 0^\circ \end{bmatrix},\ \check{b}^{\check{b}}_{ars}(0) = \begin{bmatrix} 0 \\ 0 \\ 0 \end{bmatrix}^\top$$

from which the estimates of all estimators are derived. The initial covariance matrices of all KFs are $\check{P}(0) = I_9$. $\check{(\cdot)}$ is a placeholder for $\underline{(\cdot)}$, $\bar{(\cdot)}$, and $\hat{(\cdot)}$. Additionally, depth measurements modeled by (6.41) was added.

The KFs are implemented in discrete time.

The attitude estimator tuning parameters are chosen as $\underline{\sigma} = \bar{\sigma} = \hat{\sigma} = 1$, $\underline{K}_p = \text{diag}(1, 1, 10)$, $\bar{K}_p = \hat{K}_p = \text{diag}(1, 1, 1)$, $\underline{k}_I = .01 = \bar{k}_I = 0.001$. In order to speed up convergence, the tuning parameters K_p and k_I for all attitude estimators are set to $10I_3$ and 0.1 for the first 60 seconds, respectively.

Table 7.1: MAE of Euclidean distance between AT estimates and true trajectory from 50 simulations with 4 receivers.

Est.	XYZ [m]
AT1	2.735
AT2	1.039

Table 7.2: Horizontal and vertical MAE values from 50 simulations with 3 receivers. The linearized KF uses LTV KF1's state as linearization point.

Est.	XY [m]	Z [m]
AT1	1.838	1.407
LTV KF1	1.769	0.049
Lin KF	0.525	0.054
EKF	0.444	0.058

In the 500 seconds of simulation, the vehicle stands still for the first 100 seconds to let the estimators converge. Then, it descends and moves in a lawnmower pattern for 400 seconds.

NED position errors are used to compare the estimators, and are calculated from the mean of

$$\check{p}^n_{nb} = \sum_{i=1}^{2}(-p^n_{nt_i} + R^{n\top}_b \check{p}^b_{t_i b})/2,$$

where the true rotation matrix R^n_b was used. In Table 7.1, the MAE values of the two ATs over 50 simulations with 4 receivers is shown. Clearly, AT2 suffers less from noise than AT1. The ATs' MAE values in Table 7.1–7.3, reveal another difference between the ATs. The larger MAE of AT1 with 4 receivers ($2.735m$) than with 3 receivers ($\sqrt{1.838^2 + 1.407^2} = 2.31m$ is explained by the large variance induced by AT1's noise sensitive calculation. In contrast, AT2's MAEs in the two cases are almost identical ($1.039m$ vs. $\sqrt{0.881^2 + .553^2} = 1.040$), evidencing the low variance of AT2's calculation. From this, we conclude that AT2 is preferred over AT1 when 4 or more receivers are available. This was an expected result as the variance of AT1, (6.22), increases quadratically with distance, while the variance of AT2, (6.28), is constant. Furthermore, when only 3 receivers are available, solutions replacing the need for the last receiver by depth measurements should be sought for reliability of the estimators.

In Table 7.2, the MAE values from 50 simulations with 3 receivers are seen. Here,

Table 7.3: Horizontal and vertical MAE values from 50 simulations with 4 receivers. The linearized KF uses LTV KF2's state as linearization point.

Est.	XY [m]	Z [m]
AT2	0.881	0.553
LTV KF2	0.402	0.048
Lin KF	0.388	0.054
EKF	0.549	0.058

the iterative improvement in each step is apparent by the horizontal MAEs.

Table 7.3 shows a similar simulation but with 4 receivers. Here, no improvement in performance is seen in the third stage linearized KF and EKF relative to LTV KF2. This indicates that there is little benefit from adding the third stage KF when $M \geq 4$. This is due to LTV KF2 being almost identical to the linearized KF. Furthermore, the high performance of LTV KF2 allows for a significant reduction in computational cost by not implementing the third stage filter.

Since the there is little difference in the position estimation, one expects the attitude estimates based on the transponder baseline reference vectors to be similar as well. This is confirmed in Figure 7.2, where the yaw error in one of the simulations is shown. Only yaw is shown since there is virtually no difference between the roll and pitch estimates of the different estimators. This is because estimation of roll and pitch are largely based on accelerometer measurements, which are common for all estimators.

Interestingly, the body-fixed filters in this chapter performed well when using $G_x(\bar{x})$, and not $G_x(0)$ as was needed in Chapter 6. The reason for this is not exactly known, but it is speculated that using multiple transponders gives a less erroneous build up of the covariance matrix. Alternatively, the shorter distance to the transponder makes the difference. Since the build up in the covariance matrix is quadratic in $p^b_{t_i b}$ through the term $G\mathcal{Q}G^\top$ in (1.3c), this can explain the behavior. However, an improvement in performance was experienced also in the simulation with a shorter distance to transponder in Chapter 6. Lastly, it cannot be ruled out that it is caused by an implementation error, even though the code implementation of the filters in Chapter 6 and 7 are identical, differing only in the input values.

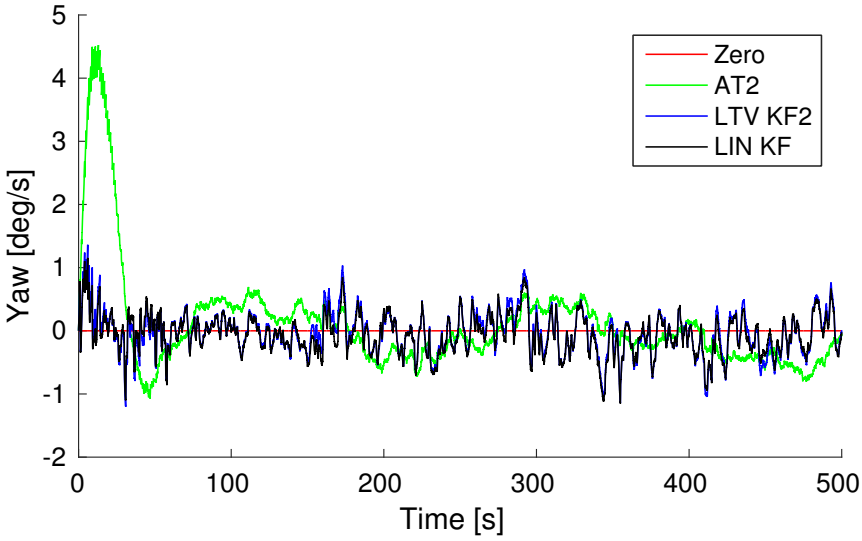

Figure 7.2: The yaw estimation errors in Euler angles in one of the 50 simulations. The legend describes the baseline estimates that are used in each estimator.

7.5.2 Experiments

The experimental set-up was identical to that in Section 6.5.2 with transponders at

$$p^n_{t_1 b} = \begin{bmatrix} -2.12 \\ 1.92 \\ -0.76 \end{bmatrix} m, \; p^n_{t_2 b} = \begin{bmatrix} 3.15 \\ 1.89 \\ -0.11 \end{bmatrix} m.$$

The true trajectory and estimates of $p^b_{t_1 b}$ from experimental data are shown in Figure 7.3. We see that AT2 is more noisy and seems to react more to outliers, which is expected. The similar performance of LTV KF2 and Lin KF from the simulations is supported by the experimental results as well. A slower convergence of the EKF than LTV KF2 and the linearized KF is evidenced. This may be improved somewhat by tuning, but faster convergence is a benefit of the 3SF nonetheless.

Figure 7.4 shows the true and estimated yaw trajectories, from which only small performance differences can be seen.

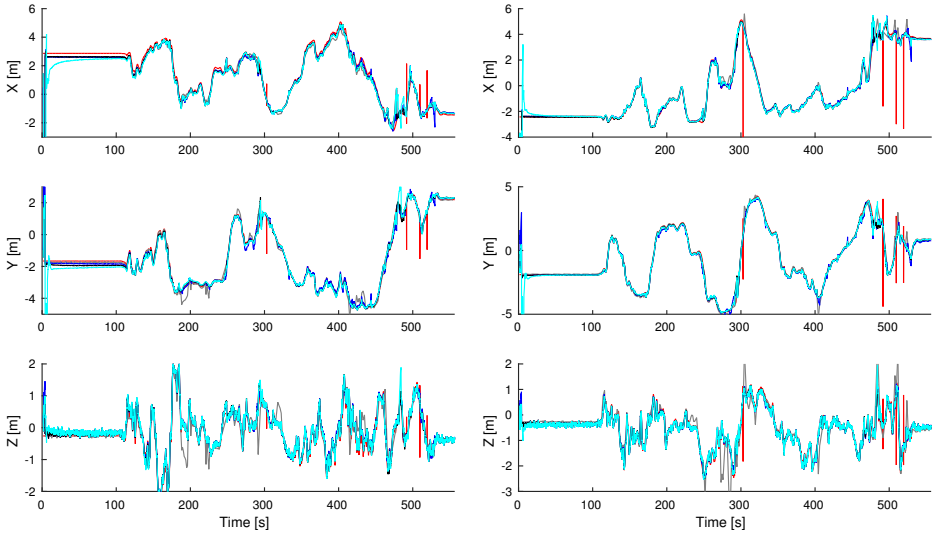

(a) $p^b_{t_1 b}$. **(b)** $p^b_{t_2 b}$.

Figure 7.3: The true trajectory in (red) and the AT (gray), LTV KF (blue), linearized KF (black), and EKF (cyan) estimates of it.

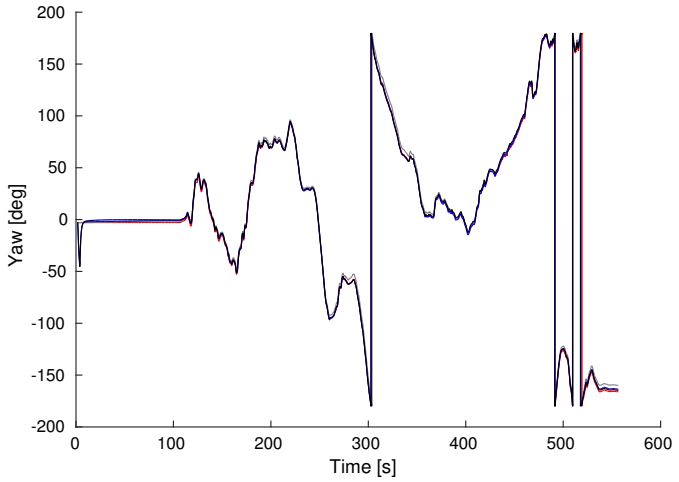

Figure 7.4: The true yaw trajectory (red) and its estimates based on reference vector from AT (gray), LTV KF (blue), linearized KF (black).

7.6 Conclusion

When a magnetometer no longer measures only Earth's magnetic field but also those produced by e.g. on-board motors or external infrastructure, it cannot be relied on for attitude estimation. Therefore, another reference vector is needed for yaw estimation. This chapter describes a method for yaw estimation using transponder baselines that are known in NED and estimated in the body-fixed coordinate frame. The transponders baselines are estimated by iSBL measurements with 3 or more receivers. First, crude calculation of the body-fixed positions of the vehicle relative the transponders are used to estimate a preliminary yaw estimate. Then, both position and attitude estimates are incrementally improved in two subsequent stages. The resulting 3SF for both position and attitude estimation is proven to be GES, and its performance is analyzed in a simulation study and using experimental data.

When 3 receivers are available, the crude calculation is highly sensitive to noise, and all three stages are needed in order to yield good position and attitude estimation. However, with 4 or more receivers, a less noise-sensitive calculation can be used and only two of the steps are needed. For higher reliability and the possibility for a significant computational cost reduction with 3 receivers, a solution should be looked into where the depth measurement replaces the need for the fourth receiver. This way, the calculation used for 4 or more receivers can be utilized, which has a constant variance w.r.t. distance to the transponder relative to the calculation used for 3 receivers which increases quadratically with distance.

The 3SF was shown in both cases to yield approximately the same performance as the EKF used as benchmark. Additionally, 3SF estimated the yaw of the vehicle with satisfying accuracy.

This chapter aimed at answering the research question "*Can the iSBL network with two transponders replace the need for the generally unreliable magnetic field measurements? Furthermore, can the XKF method be applied to this problem to give global stability of the solution?*". This chapter has shown that the iSBL can be used for attitude estimation with multiple transponders and attain GES estimation by using the XKF method.

Appendix

7.A Proof of Proposition 7.4.3

In the noise-free case, we have that the AT in Section 7.1 is exact, i.e., $\underline{p}^b_{t_i b} = p^b_{t_i b}\ \forall\ i \in (1, N)$ and consequently $\underline{\xi}_z = 0$. Therefore, Proposition 7.4.1 directly proves that the origin $\tilde{\underline{z}} = 0$ of $\underline{\Sigma}_z$ is GES.

The proof of Proposition 6.4.1 in Appendix 6.C can now be used to prove that the origin $\tilde{\underline{z}} = 0$ and $\tilde{\bar{x}}_k = 0$ of $\underline{\Sigma}_z$–$\bar{\Sigma}_{xk}$ is GES for $k = (1, 2)$.

Now, a similar argument as that of Appendix 6.C.1 proves that the origin $\tilde{\underline{z}} = 0$, $\tilde{\bar{x}}_k = 0$, and $\tilde{\bar{z}} = 0$ of $\underline{\Sigma}_z$–$\bar{\Sigma}_{xk}$–$\bar{\Sigma}_z$ is GES for $k = (1, 2)$.

A similar argument as that of Appendix 6.C.1 proves that the origin $\tilde{\underline{z}} = 0$, $\tilde{\bar{x}}_k = 0$, $\tilde{\bar{z}} = 0$, and $\tilde{x} = 0$ of $\underline{\Sigma}_z$–$\bar{\Sigma}_{xk}$–$\bar{\Sigma}_z$–$\hat{\Sigma}_x$ is GES for $k = (1, 2)$.

Finally, a similar argument as that of Appendix 6.C.1 proves that the origin $\tilde{\underline{z}} = 0$, $\tilde{\bar{x}}_k = 0$, $\tilde{\bar{z}} = 0$, $\tilde{x} = 0$, $\tilde{z} = 0$ of $\underline{\Sigma}_z$–$\bar{\Sigma}_{xk}$–$\bar{\Sigma}_z$–$\hat{\Sigma}_x$–$\hat{\Sigma}_z$ is GES for $k = (1, 2)$. This concludes the proof.

Part III

Concluding Remarks

Chapter 8

Conclusion and Future Work

Here, concluding remarks on the researched topics are given, along with a discussion related to the overarching research question posed in Section 1.6, and also to future research.

8.1 Conclusion

This thesis presented new theoretical results on aided inertial navigation (AIN) of underwater vehicles. The position and attitude estimation problems were considered, and estimators with global and exponential convergence were developed. Simulation and experimental studies showed by comparison of mean absolute error (MAE) values that the filters developed in this thesis achieved extended Kalman filter (EKF)-like performance, which along with the guaranteed stability consitute significant contributions.

In Chapter 4, the multiplicative exogenous Kalman filter (MXKF) was developed. It is to the best of the author's knowledge the first Kalman filter (KF)-based attitude estimator using a minimal state error representation and with proven global exponential stability (GES). Both in simulations and experimentally, it was shown to have identical steady-state performance as the multiplicative extended Kalman filter (MEKF) significantly better than the nonlinear observer about whose estimate the models were linearized. Furthermore, the MXKF was shown to have better transient performance than the MEKF when the nonlinear observer was tuned aggressively for fast convergence.

In Chapter 5, three-stage filters (3SFs) for position and wave speed estimation us-

ing a long baseline (LBL), depth, and inertial measurement unit (IMU) measurements were developed and shown to be GES. Along with the 3SF of Stovner et al. [68], a previously unpublished 3SF incorporating the depth measurement in the algebraic transformation (AT) was developed, showing a significant improvement in performance. This allowed a linearized model about an estimate calculated in the AT to be used in the second stage filter. The second stage filter was shown in a simulation study to yield EKF-like performance, meaning one can be saved the computational burden of a third stage filter.

Chapter 6 studied the position estimation of an underwater vehicle using the inverted short baseline (iSBL) network with the requirement of only one transponder on the sea floor. A GES attitude observer provided attitude and angular rate sensor (ARS) bias estimates using accelerometer and magnetometer measurements. A total of four 3SFs using either a north-east-down (NED) or body-fixed formulation were developed. A simulation study concluded that the NED formulation yielded more accurate estimation, due to the sensitivity to noisy attitude and ARS bias estimates when using the body-fixed formulation. Furthermore, one of the NED formulated filters was shown to yield similar performance in the second and third stages, meaning computational complexity can be lowered at a small performance cost.

The set-up studied in Chapter 7 was similar to that of Chapter 6, except it was assumed that the magnetometer providing heading information to the attitude estimator was compromised. To remedy this, two transponders on the sea floor was assumed, and it was shown how body-fixed estimates of the underwater vehicle's position relative to each of them could be used as reference vectors to the attitude estimators, thus replacing the magnetometer measurements. A 3SF that incrementally improved the accuracy of both attitude and position estimates was developed and shown to be GES. The 3SF of Stovner and Johansen [69] was improved by utilizing a formulation developed in Chapter 6, resulting in a previously unpublished 3SF. A simulation study showed a significant performance improvement, which was also experimentally verified.

In Section 1.6, an overarching research question was posed: "What are the theoretical and practical limitations of the exogeonus Kalman filter (XKF) and which implications do these have for AIN of underwater vehicles? Under which circumstances should other methods be preferred?". The XKF is theoretically limitated to differentiable systems of which an auxiliary state estimate is attainable. Specifically, an auxiliary estimate is needed only of the states that *appear nonlinearly*

in the dynamics or measurement equations. This is e.g. seen in the problems of chapters 5–7 where an auxiliary velocity estimate was not needed since it never appeared nonlinearly. However, non-unique or singular state representations may cause problems, evidenced by Chapter 4. There, a work-around was found such that GES of the MXKF could be shown, but it can not be concluded that this can be done for all such systems. A practical limitation of this is that the auxiliary estimate must be *good enough*, both w.r.t. stability properties and estimation accuracy. The former is important as it is not interesting to inherit poor stability properties. In that case, an EKF could be implemented instead and efforts saved. The latter is important for the estimation accuracy of the XKF. It has been shown in this thesis that the estimation accuracy of the XKF's linearization point does not need to be particularly good, especially seen in Example 1.3.2. However, a large error will cause the XKF to perform considerably worse than an EKF, which was seen in Chapter 5.

To show the relevance of the last question, one needs only look at Chapter 6, in which a linear measurement model was achieved through algebraic manipulation that gave performance similar to the one achieved through differentiation. Additionally, this solution allowed for the implementation of only the second stage KF, thus saving the computational cost of a third stage filter. Such solutions should especially be pursued as alternatives to the 3SF, which is computationally demanding. This was a special case, and hence, it cannot replace the more general applicability of the XKF. Chapter 5 presented another way of reducing the computational burden of the 3SF. There, it was shown that with an accurate enough linearization point calculated explicitly in the first stage, a linearized KF could be implemented directly, thus avoiding the need for two KFs.

8.2 Future Work

From the author's point of view, there are a range of interesting practical and theoretical research topics that would considerably improve the work presented in this thesis. Specific suggestions were given in each chapter, and here, more general topics are discussed.

Practical work that should be undertaken for the position estimation problem includes further experimental verification with greater distances to transponders. In this thesis, the pool experiments were limited by the size of the volume of the pool visible to the Qualisys Oqus Underwater camera system. This gives a limited experimental verification of the filters, which should be extended by sea trials with other position measurements for verification.

This thesis has not attempted to show instabilities occuring in the implemented EKFs. A study of the problems discussed in chapters 4–7 including circumstances that make an EKF diverge while observing the XKF's response could be of significant value.

Bibliography

[1] I. Schjølberg and I. B. Utne. “Towards autonomy in ROV operations”. In: *IFAC-PapersOnLine* 48.2 (Jan. 2015), pp. 183–188.

[2] I. Schjølberg et al. “Next Generation Subsea Inspection, Maintenance and Repair Operations”. In: *IFAC-PapersOnLine* 49.23 (Jan. 2016), pp. 434–439.

[3] T. H. Bryne et al. “Nonlinear Observers for Integrated INS\/GNSS Navigation: Implementation Aspects”. In: *IEEE Control Systems* 37.3 (June 2017), pp. 59–86.

[4] S. I. Roumeliotis, G. S. Sukhatme, and G. A. Bekey. “Circumventing dynamic modeling: evaluation of the error-state Kalman filter applied to mobile robot localization”. In: *Proceedings of the International Conference on Robotics and Automation*. Vol. 2. IEEE, 1999, pp. 1656–1663.

[5] R. E. Kalman and R. S. Bucy. “New results in linear filtering and prediction theory”. In: *Journal of Basic Engineering* 83.1 (1961), pp. 95–108.

[6] H. K. Khalil. *Nonlinear Systems*. 3rd ed. Prentice Hall, 2000.

[7] R. E. Kalman. “A New Approach to Linear Filtering and Prediction Problems”. In: *Journal of Basic Engineering* 82.Series D (1960), pp. 35–45.

[8] T. A. Johansen and T. I. Fossen. “The eXogenous Kalman Filter (XKF)”. In: *International Journal of Control* 90 (2017), pp. 161–167.

[9] M. N. Armenise et al. *Advances in Gyroscope Technologies*. Berlin, Heidelberg: Springer Berlin Heidelberg, 2011.

[10] S. M. Smith and D. Kronen. “Experimental results of an inexpensive short baseline acoustic positioning system for AUV navigation”. In: *Oceans ’97. MTS/IEEE Conference Proceedings*. Vol. 1. IEEE, 1997, pp. 714–720.

[11] B. B. Stovner, T. A. Johansen, and I. Schjølberg. “Globally Exponentially Stable Aided Inertial Navigation with Hydroacoustic Measurements from One Transponder”. In: *Proc. of the American Contr. Conf.* 37.1 (2017), pp. 1219–1226.

[12] K. Vickery. “Acoustic positioning systems. A practical overview of current systems”. In: *Proceedings of the 1998 Workshop on Autonomous Underwater Vehicles (Cat. No.98CH36290)* (1998), pp. 5–17.

[13] G. L. Smith, S. F. Schmidt, and L. A. McGee. *Application of statistical filter theory to the optimal estimation of position and velocity on board a circumlunar vehicle*. Washington, D. C. : 1962.

[14] S. F. Schmidt. “Applications of State Space Methods to Navigation Problems”. In: *in C. T. Leondes, Editor, Advanced Control Systems* 3 (1966), pp. 293–340.

[15] P. Kaminski, A. Bryson, and S. Schmidt. “Discrete square root filtering: A survey of current techniques”. In: *IEEE Transactions on Automatic Control* 16.6 (Dec. 1971), pp. 727–736.

[16] F. Gustafsson. *Statistical sensor fusion*. Studentlitteratur, 2012.

[17] S. J. Julier, J. K. Uhlmann, and H. F. Durrant-Whyte. “A new approach for filtering nonlinear systems”. In: *Proc. of American Control Conference*. Vol. 3. American Autom Control Council, 1995, pp. 1628–1632.

[18] T. A. Johansen and T. I. Fossen. “Nonlinear Observer for Tightly Coupled Integration of Pseudorange and Inertial Measurements”. In: *IEEE Transactions on Control Systems Technology* 24 (2016), pp. 2199–2206.

[19] T. A. Johansen, T. I. Fossen, and G. C. Goodwin. “Three-stage filter for position estimation using pseudo-range measurements”. In: *IEEE Transactions on Aerospace and Electronic Systems* 52 (2016), pp. 1631–1643.

[20] J. Stuelpnagel. “On the Parametrization of the Three-Dimensional Rotation Group”. In: *SIAM Review* 6.4 (Oct. 1964), pp. 422–430.

[21] Alfred C. Robinson. *On the Use of Quaternions in Simulation of Rigid-Body Motion*. Tech. rep. 1958, pp. 1–100.

[22] T. I. Fossen. *Handbook of Marine Craft Hydrodynamics and Motion Control*. 2011.

[23] M. D. Shuster. *A Survey of Attitude Representations*. Vol. 41. 1993, pp. 439–517.

[24] F. L. Markley. “Attitude Error Representations for Kalman Filtering”. In: *Journal of Guidance, Control, and Dynamics* 26.2 (2003), pp. 311–317.

[25] H. D. Black. “A passive system for determining the attitude of a satellite”. In: *AIAA Journal* 2.7 (1964), pp. 1350–1351.

[26] F Landis Markley and John L Crassidis. *Fundamentals of Spacecraft Attitude Determination and Control*. 2014.

[27] I. Y. Bar-Itzhack and R. R. Harman. “Optimized TRIAD Algorithm for Attitude Determination”. In: *Journal of Guidance, Control, and Dynamics* 20.1 (1997), pp. 208–211.

[28] G. Wahba. “A Least Squares Estimate of Satellite Attitude”. In: *SIAM Review* 7.3 (1965), p. 409.

[29] M. D. Shuster and S. D. Oh. “Three-axis attitude determination from vector observations”. In: *Journal of Guidance and Control* 4.1 (1981), pp. 70–77.

[30] F. L. Markley and D. Mortari. “How to estimate attitude from vector observations”. In: *Advances in the Astronautical Sciences* 103.PART III (1999), pp. 1979–1996.

[31] D. C. Paulson, D. B. Jackson, and C. D. Brown. “Spars algorithms and simulation results”. In: *Proceedings of the Symposium on Spacecraft Attitude Determination*. Vol. 1. 1969, pp. 293–316.

[32] S. Kau, K. P. Kumar, and G. Granley. “Attitude Determination Via Nonlinear Filtering”. In: *IEEE Transactions on Aerospace and Electronic Systems* AES-5.6 (Nov. 1969), pp. 906–911.

[33] J. L. Farrell. “Attitude determination by kalman filtering”. In: *Automatica* 6.3 (May 1970), pp. 419–430.

[34] N. F. Toda, J. L. Heiss, and F. H. Schlee. “SPARS: The System, Algorithms, and Test Results”. In: *Aerospace Corp. Rept. TR-0066 (5306)-12* (1969), pp. 361–370.

[35] E. Lefferts, F. Markley, and M. Shuster. “Kalman filtering for spacecraft attitude estimation”. In: *Journal of Guidance, Control, and ...* 5.5 (1982), pp. 417–429.

[36] I. Y. Bar-Itzhack and Y. Oshman. “Attitude Determination from Vector Observations: Quaternion Estimation”. In: *IEEE Transactions on Aerospace and Electronic Systems* AES-21.1 (Jan. 1985), pp. 128–136.

[37] M. D. Shuster. “Constraint in Attitude Estimation Part II: Unconstrained Estimation”. In: *The Journal of the Astronautical Sciences* 51.1 (2003), pp. 75–101.

[38] V. A. Ferraresi. “Utilizacão conjunta de sensores inerciais e não-inerciais em determinação de attitude de satélites via filtre de Kalman”. In: *Technical Report INPE-4313-TDL/280, São José dos Campos, SP, Brazil,* (1987).

[39] M. D. Shuster. “The Quaternion in Kalman Filtering”. In: *Advances in the Astronautical Sciences* 85.pt 1 (1993), pp. 25–37.

[40] Renato Zanetti and Robert H Bishop. “Quaternion estimation and norm constrained Kalman filtering”. In: *AIAA/AAS Astrodynamics Specialist Conference and Exhibit* August (2006), pp. 1–15.

[41] Renato Zanetti et al. “Norm-Constrained Kalman Filtering”. In: *Journal of Guidance, Control, and Dynamics* 32.5 (2009), pp. 1458–1465.

[42] S. Bonnabel, P. Martin, and E. Salaun. “Invariant Extended Kalman Filter: theory and application to a velocity-aided attitude estimation problem”. In: *Proceedings of the 48th IEEE Conference on Decision and Control, 2009*. Vol. 6. 2009, pp. 1297–1304.

[43] M. S. Andrle and J. L. Crassidis. “Attitude Estimation Employing Common Frame Error Representations”. In: *Journal of Guidance, Control, and Dynamics* 38.9 (2015), pp. 1614–1624.

[44] S. Salcudean. “A Globally Convergent Angular Velocity Observer for Rigid Body Motion”. In: *IEEE Transactions on Automatic Control* 36.12 (1991), pp. 1493–1497.

[45] J. Thienel and R. M. Sanner. “A Coupled Nonlinear Spacecraft Attitude Controller and Observer with an Unknown Constant Gyro Bias and Gyro Noise”. In: *IEEE Transactions on Automatic Control* 48.11 (2003), pp. 2011–2014.

[46] Robert Mahony, Tarek Hamel, and Jean Michel Pflimlin. “Nonlinear complementary filters on the special orthogonal group”. In: *IEEE Transactions on Automatic Control* 53.5 (2008), pp. 1203–1218.

[47] P. Batista, C. Silvestre, and P. Oliveira. “GES Attitude Observers – Part I: Multiple General Vector Observations”. In: *IFAC Proceedings Volumes* 44.1 (Jan. 2011), pp. 2985–2990.

[48] P. Batista, C. Silvestre, and P. Oliveira. “GES Attitude Observers – Part II: Single Vector Observations”. In: *IFAC Proceedings Volumes* 44.1 (Jan. 2011), pp. 2991–2996.

[49] P. Batista, C. Silvestre, and P. Oliveira. “A GES attitude observer with single vector observations”. In: *Automatica* 48.2 (2012), pp. 339–388.

[50] M. D. Hua. “Attitude estimation for accelerated vehicles using GPS/INS measurements”. In: *Control Engineering Practice* 18.7 (2010), pp. 723–732.

[51] H. F. Grip et al. “Attitude Estimation Using Biased Gyro and Vector Measurements With Time-Varying Reference Vectors”. In: *IEEE Transactions on Automatic Control* 57.5 (2012), pp. 1332–1338.

[52] H. F. Grip et al. “Globally exponentially stable attitude and gyro bias estimation with application to GNSS/INS integration”. In: *Automatica* 51.June (2015), pp. 158–166.

[53] P. Martin and E. Salaün. “An Invariant Observer for Earth-Velocity-Aided Attitude Heading Reference Systems”. In: *IFAC Proceedings Volumes* 41.2 (Jan. 2008), pp. 9857–9864.

[54] H. F. Grip et al. “A nonlinear observer for integration of GNSS and IMU measurements with gyro bias estimation”. In: *Proc. of the American Contr. Conf.* (2012), pp. 4607–4612.

[55] P. Batista, C. Silvestre, and P. Oliveira. “GES integrated LBL/USBL navigation system for underwater vehicles”. In: *Proceedings of the IEEE Conference on Decision and Control* (2012), pp. 6609–6614.

[56] E. K. Jørgensen and I. Schjølberg. “Attitude and Gyro bias estimation using range-difference and IMU measurements”. In: *2016 IEEE/OES Autonomous Underwater Vehicles (AUV)*. IEEE, Nov. 2016, pp. 124–130.

[57] S. Bancroft. “An Algebraic Solution of the GPS Equations”. In: *IEEE Transactions on Aerospace and Electronic Systems* AES-21.1 (1985), pp. 56–59.

[58] J. Chaffee and J. Abel. “On the exact solutions of pseudorange equations”. In: *IEEE Transactions on Aerospace and Electronic Systems* 30.4 (1994), pp. 1021–1030.

[59] M. S. Grewal, L. R. Weill, and A. P. Andrews. *Global Positioning Systems, Inertial Navigation, and Integration, Second Edition*. Wiley, 2006.

[60] J. L. Farrell. *Aided navigation: GPS with high rate sensors*. McGraw-Hill, 2008.

[61] B. Vik and T. I. Fossen. “A nonlinear observer for GPS and INS integration”. In: *Proceedings of the 40th IEEE Conference on Decision and Control (Cat. No.01CH37228)* 3.December (2001), pp. 2956–2961.

[62] T. A. Johansen and T. I. Fossen. “Nonlinear observer for inertial navigation aided by pseudo-range and range-rate measurements”. In: *2015 European Control Conference, ECC 2015*. 2015, pp. 1673–1680.

[63] P. Batista. “GES long baseline navigation with unknown sound velocity and discrete-time range measurements”. In: *IEEE Conference on Decision and Control*. 2013, pp. 6176–6181.

[64] P. Batista, C. Silvestre, and P. Oliveira. “Single beacon navigation: Observability analysis and filter design”. In: *American Control Conference (ACC), 2010* (2010), pp. 6191–6196.

[65] M Morgado et al. “Position and Velocity USBL / IMU Sensor-based Navigation Filter”. In: *18th IFAC World Congress* (2011), pp. 13642–13647.

[66] B. N. Stovner et al. “Attitude Estimation by Multiplicative eXogenous Kalman Filter”. In: *Automatica* Provisionally Accepted (2018).

[67] B. N. Stovner, T. A. Johansen, and I. Schjølberg. “Globally Exponentially Stable Filters for Underwater Position Estimation Using A Single Hydroacoustic Transponder”. In: *Ocean Engineering* Accepted (2018).

[68] Bård B Stovner et al. “Three-stage Filter for Position and Velocity Estimation from Long Baseline Measurements with Unknown Wave Speed”. In: *Proc. of the American Contr. Conf.* 2016, pp. 4532–4538.

[69] B. B. Stovner and T. A Johansen. “Hydroacoustically Aided Inertial Navigation for Joint Position and Attitude Estimation in Absence of Magnetic Field Measurements”. In: *Proc. of the American Contr. Conf.* 37.1 (2017), pp. 1211–1218.

[70] E. K. Jørgensen, B. B. Stovner, and I. Schjølberg. “Experimental validation of three-stage position filter based on long baseline measurements with unknown wave speed”. In: *Proc. of Conference on Control Technology and Applications*. IEEE, Aug. 2017, pp. 680–686.

[71] J. L. Crassidis and F. L. Markley. *Attitude Estimation Using Modified Rodrigues Parameters*. 1996.

[72] C. Karlgaard and H. Schaub. “Nonsingular attitude filtering using Modified Rodrigues Parameters”. In: *The Journal of the Astronautical Sciences* 57 (2010), pp. 777–791.

[73] F. Khan. *LTE for 4G Mobile Broadband: Air Interface Technologies and Performance*. 1st. Cambridge University Press, 2009.

[74] T. A. Johansen and T. I. Fossen. "Nonlinear Filtering with eXogenous Kalman Filter and Double Kalman Filter". In: *Proceedings of European Control Conference*. 2016.

[75] X. Xu. "Generalization of the Sherman-Morrison-Woodbury formula involving the Schur complement". In: *Applied Mathematics and Computations* 309 (2017), pp. 183–191.

[76] C. Chen. *Linear System Theory and Design*. 3rd. Oxford University Press, Inc., 1998.

[77] C. D. Meyer. "Generalized Inverses and Ranks of Block Matrices". In: *SIAM Review* 25.4 (1973), pp. 597–602.

[78] E. K. Jørgensen, T. A. Johansen, and I. Schjølberg. "Enhanced Hydroacoustic Range Robustness of Three-Stage Position Filter based on Long Baseline Measurements with Unknown Wave Speed". In: *Conference on Control Applications in Marine Systems*. 2016.

[79] B. D. O Anderson. "Stability Properties of Kalman-Bucy Filters". In: *Journal of the Franklin Institute* 291.2 (1971), pp. 137–144.

[80] A. Loria and E. Panteley. "Cascaded nonlinear time-varying systems : analysis and design". In: *Advanced Topics in Control Systems Theory*. Springer, 2005. Chap. 2, pp. 23–64.

Previous PhD theses published at the Departement of Marine Technology (earlier: Faculty of Marine Technology) NORWEGIAN UNIVERSITY OF SCIENCE AND TECHNOLOGY

Report No.	Author	Title
	Kavlie, Dag	Optimization of Plane Elastic Grillages, 1967
	Hansen, Hans R.	Man-Machine Communication and Data-Storage Methods in Ship Structural Design, 1971
	Gisvold, Kaare M.	A Method for non-linear mixed -integer programming and its Application to Design Problems, 1971
	Lund, Sverre	Tanker Frame Optimalization by means of SUMT-Transformation and Behaviour Models, 1971
	Vinje, Tor	On Vibration of Spherical Shells Interacting with Fluid, 1972
	Lorentz, Jan D.	Tank Arrangement for Crude Oil Carriers in Accordance with the new Anti-Pollution Regulations, 1975
	Carlsen, Carl A.	Computer-Aided Design of Tanker Structures, 1975
	Larsen, Carl M.	Static and Dynamic Analysis of Offshore Pipelines during Installation, 1976
UR-79-01	Brigt Hatlestad, MK	The finite element method used in a fatigue evaluation of fixed offshore platforms. (Dr.Ing. Thesis)
UR-79-02	Erik Pettersen, MK	Analysis and design of cellular structures. (Dr.Ing. Thesis)
UR-79-03	Sverre Valsgård, MK	Finite difference and finite element methods applied to nonlinear analysis of plated structures. (Dr.Ing. Thesis)
UR-79-04	Nils T. Nordsve, MK	Finite element collapse analysis of structural members considering imperfections and stresses due to fabrication. (Dr.Ing. Thesis)
UR-79-05	Ivar J. Fylling, MK	Analysis of towline forces in ocean towing systems. (Dr.Ing. Thesis)
UR-80-06	Nils Sandsmark, MM	Analysis of Stationary and Transient Heat Conduction by the Use of the Finite Element Method. (Dr.Ing. Thesis)
UR-80-09	Sverre Haver, MK	Analysis of uncertainties related to the stochastic modeling of ocean waves. (Dr.Ing. Thesis)
UR-81-15	Odland, Jonas	On the Strength of welded Ring stiffened cylindrical Shells primarily subjected to axial Compression
UR-82-17	Engesvik, Knut	Analysis of Uncertainties in the fatigue Capacity of

		Welded Joints
UR-82-18	Rye, Henrik	Ocean wave groups
UR-83-30	Eide, Oddvar Inge	On Cumulative Fatigue Damage in Steel Welded Joints
UR-83-33	Mo, Olav	Stochastic Time Domain Analysis of Slender Offshore Structures
UR-83-34	Amdahl, Jørgen	Energy absorption in Ship-platform impacts
UR-84-37	Mørch, Morten	Motions and mooring forces of semi submersibles as determined by full-scale measurements and theoretical analysis
UR-84-38	Soares, C. Guedes	Probabilistic models for load effects in ship structures
UR-84-39	Aarsnes, Jan V.	Current forces on ships
UR-84-40	Czujko, Jerzy	Collapse Analysis of Plates subjected to Biaxial Compression and Lateral Load
UR-85-46	Alf G. Engseth, MK	Finite element collapse analysis of tubular steel offshore structures. (Dr.Ing. Thesis)
UR-86-47	Dengody Sheshappa, MP	A Computer Design Model for Optimizing Fishing Vessel Designs Based on Techno-Economic Analysis. (Dr.Ing. Thesis)
UR-86-48	Vidar Aanesland, MH	A Theoretical and Numerical Study of Ship Wave Resistance. (Dr.Ing. Thesis)
UR-86-49	Heinz-Joachim Wessel, MK	Fracture Mechanics Analysis of Crack Growth in Plate Girders. (Dr.Ing. Thesis)
UR-86-50	Jon Taby, MK	Ultimate and Post-ultimate Strength of Dented Tubular Members. (Dr.Ing. Thesis)
UR-86-51	Walter Lian, MH	A Numerical Study of Two-Dimensional Separated Flow Past Bluff Bodies at Moderate KC-Numbers. (Dr.Ing. Thesis)
UR-86-52	Bjørn Sortland, MH	Force Measurements in Oscillating Flow on Ship Sections and Circular Cylinders in a U-Tube Water Tank. (Dr.Ing. Thesis)
UR-86-53	Kurt Strand, MM	A System Dynamic Approach to One-dimensional Fluid Flow. (Dr.Ing. Thesis)
UR-86-54	Arne Edvin Løken, MH	Three Dimensional Second Order Hydrodynamic Effects on Ocean Structures in Waves. (Dr.Ing. Thesis)
UR-86-55	Sigurd Falch, MH	A Numerical Study of Slamming of Two-Dimensional Bodies. (Dr.Ing. Thesis)
UR-87-56	Arne Braathen, MH	Application of a Vortex Tracking Method to the Prediction of Roll Damping of a Two-Dimension Floating Body. (Dr.Ing. Thesis)

UR-87-57	Bernt Leira, MK	Gaussian Vector Processes for Reliability Analysis involving Wave-Induced Load Effects. (Dr.Ing. Thesis)
UR-87-58	Magnus Småvik, MM	Thermal Load and Process Characteristics in a Two-Stroke Diesel Engine with Thermal Barriers (in Norwegian). (Dr.Ing. Thesis)
MTA-88-59	Bernt Arild Bremdal, MP	An Investigation of Marine Installation Processes – A Knowledge - Based Planning Approach. (Dr.Ing. Thesis)
MTA-88-60	Xu Jun, MK	Non-linear Dynamic Analysis of Space-framed Offshore Structures. (Dr.Ing. Thesis)
MTA-89-61	Gang Miao, MH	Hydrodynamic Forces and Dynamic Responses of Circular Cylinders in Wave Zones. (Dr.Ing. Thesis)
MTA-89-62	Martin Greenhow, MH	Linear and Non-Linear Studies of Waves and Floating Bodies. Part I and Part II. (Dr.Techn. Thesis)
MTA-89-63	Chang Li, MH	Force Coefficients of Spheres and Cubes in Oscillatory Flow with and without Current. (Dr.Ing. Thesis
MTA-89-64	Hu Ying, MP	A Study of Marketing and Design in Development of Marine Transport Systems. (Dr.Ing. Thesis)
MTA-89-65	Arild Jæger, MH	Seakeeping, Dynamic Stability and Performance of a Wedge Shaped Planing Hull. (Dr.Ing. Thesis)
MTA-89-66	Chan Siu Hung, MM	The dynamic characteristics of tilting-pad bearings
MTA-89-67	Kim Wikstrøm, MP	Analysis av projekteringen for ett offshore projekt. (Licenciat-avhandling)
MTA-89-68	Jiao Guoyang, MK	Reliability Analysis of Crack Growth under Random Loading, considering Model Updating. (Dr.Ing. Thesis)
MTA-89-69	Arnt Olufsen, MK	Uncertainty and Reliability Analysis of Fixed Offshore Structures. (Dr.Ing. Thesis)
MTA-89-70	Wu Yu-Lin, MR	System Reliability Analyses of Offshore Structures using improved Truss and Beam Models. (Dr.Ing. Thesis)
MTA-90-71	Jan Roger Hoff, MH	Three-dimensional Green function of a vessel with forward speed in waves. (Dr.Ing. Thesis)
MTA-90-72	Rong Zhao, MH	Slow-Drift Motions of a Moored Two-Dimensional Body in Irregular Waves. (Dr.Ing. Thesis)
MTA-90-73	Atle Minsaas, MP	Economical Risk Analysis. (Dr.Ing. Thesis)
MTA-90-74	Knut-Aril Farnes, MK	Long-term Statistics of Response in Non-linear Marine Structures. (Dr.Ing. Thesis)
MTA-90-75	Torbjørn Sotberg, MK	Application of Reliability Methods for Safety Assessment of Submarine Pipelines. (Dr.Ing.

		Thesis)
MTA-90-76	Zeuthen, Steffen, MP	SEAMAID. A computational model of the design process in a constraint-based logic programming environment. An example from the offshore domain. (Dr.Ing. Thesis)
MTA-91-77	Haagensen, Sven, MM	Fuel Dependant Cyclic Variability in a Spark Ignition Engine - An Optical Approach. (Dr.Ing. Thesis)
MTA-91-78	Løland, Geir, MH	Current forces on and flow through fish farms. (Dr.Ing. Thesis)
MTA-91-79	Hoen, Christopher, MK	System Identification of Structures Excited by Stochastic Load Processes. (Dr.Ing. Thesis)
MTA-91-80	Haugen, Stein, MK	Probabilistic Evaluation of Frequency of Collision between Ships and Offshore Platforms. (Dr.Ing. Thesis)
MTA-91-81	Sødahl, Nils, MK	Methods for Design and Analysis of Flexible Risers. (Dr.Ing. Thesis)
MTA-91-82	Ormberg, Harald, MK	Non-linear Response Analysis of Floating Fish Farm Systems. (Dr.Ing. Thesis)
MTA-91-83	Marley, Mark J., MK	Time Variant Reliability under Fatigue Degradation. (Dr.Ing. Thesis)
MTA-91-84	Krokstad, Jørgen R., MH	Second-order Loads in Multidirectional Seas. (Dr.Ing. Thesis)
MTA-91-85	Molteberg, Gunnar A., MM	The Application of System Identification Techniques to Performance Monitoring of Four Stroke Turbocharged Diesel Engines. (Dr.Ing. Thesis)
MTA-92-86	Mørch, Hans Jørgen Bjelke, MH	Aspects of Hydrofoil Design: with Emphasis on Hydrofoil Interaction in Calm Water. (Dr.Ing. Thesis)
MTA-92-87	Chan Siu Hung, MM	Nonlinear Analysis of Rotordynamic Instabilities in Highspeed Turbomachinery. (Dr.Ing. Thesis)
MTA-92-88	Bessason, Bjarni, MK	Assessment of Earthquake Loading and Response of Seismically Isolated Bridges. (Dr.Ing. Thesis)
MTA-92-89	Langli, Geir, MP	Improving Operational Safety through exploitation of Design Knowledge - an investigation of offshore platform safety. (Dr.Ing. Thesis)
MTA-92-90	Sævik, Svein, MK	On Stresses and Fatigue in Flexible Pipes. (Dr.Ing. Thesis)
MTA-92-91	Ask, Tor Ø., MM	Ignition and Flame Growth in Lean Gas-Air Mixtures. An Experimental Study with a Schlieren System. (Dr.Ing. Thesis)
MTA-86-92	Hessen, Gunnar, MK	Fracture Mechanics Analysis of Stiffened Tubular Members. (Dr.Ing. Thesis)

MTA-93-93	Steinebach, Christian, MM	Knowledge Based Systems for Diagnosis of Rotating Machinery. (Dr.Ing. Thesis)
MTA-93-94	Dalane, Jan Inge, MK	System Reliability in Design and Maintenance of Fixed Offshore Structures. (Dr.Ing. Thesis)
MTA-93-95	Steen, Sverre, MH	Cobblestone Effect on SES. (Dr.Ing. Thesis)
MTA-93-96	Karunakaran, Daniel, MK	Nonlinear Dynamic Response and Reliability Analysis of Drag-dominated Offshore Platforms. (Dr.Ing. Thesis)
MTA-93-97	Hagen, Arnulf, MP	The Framework of a Design Process Language. (Dr.Ing. Thesis)
MTA-93-98	Nordrik, Rune, MM	Investigation of Spark Ignition and Autoignition in Methane and Air Using Computational Fluid Dynamics and Chemical Reaction Kinetics. A Numerical Study of Ignition Processes in Internal Combustion Engines. (Dr.Ing. Thesis)
MTA-94-99	Passano, Elizabeth, MK	Efficient Analysis of Nonlinear Slender Marine Structures. (Dr.Ing. Thesis)
MTA-94-100	Kvålsvold, Jan, MH	Hydroelastic Modelling of Wetdeck Slamming on Multihull Vessels. (Dr.Ing. Thesis)
MTA-94-102	Bech, Sidsel M., MK	Experimental and Numerical Determination of Stiffness and Strength of GRP/PVC Sandwich Structures. (Dr.Ing. Thesis)
MTA-95-103	Paulsen, Hallvard, MM	A Study of Transient Jet and Spray using a Schlieren Method and Digital Image Processing. (Dr.Ing. Thesis)
MTA-95-104	Hovde, Geir Olav, MK	Fatigue and Overload Reliability of Offshore Structural Systems, Considering the Effect of Inspection and Repair. (Dr.Ing. Thesis)
MTA-95-105	Wang, Xiaozhi, MK	Reliability Analysis of Production Ships with Emphasis on Load Combination and Ultimate Strength. (Dr.Ing. Thesis)
MTA-95-106	Ulstein, Tore, MH	Nonlinear Effects of a Flexible Stern Seal Bag on Cobblestone Oscillations of an SES. (Dr.Ing. Thesis)
MTA-95-107	Solaas, Frøydis, MH	Analytical and Numerical Studies of Sloshing in Tanks. (Dr.Ing. Thesis)
MTA-95-108	Hellan, Øyvind, MK	Nonlinear Pushover and Cyclic Analyses in Ultimate Limit State Design and Reassessment of Tubular Steel Offshore Structures. (Dr.Ing. Thesis)
MTA-95-109	Hermundstad, Ole A., MK	Theoretical and Experimental Hydroelastic Analysis of High Speed Vessels. (Dr.Ing. Thesis)
MTA-96-110	Bratland, Anne K., MH	Wave-Current Interaction Effects on Large-Volume Bodies in Water of Finite Depth. (Dr.Ing. Thesis)

MTA-96-111	Herfjord, Kjell, MH	A Study of Two-dimensional Separated Flow by a Combination of the Finite Element Method and Navier-Stokes Equations. (Dr.Ing. Thesis)
MTA-96-112	Æsøy, Vilmar, MM	Hot Surface Assisted Compression Ignition in a Direct Injection Natural Gas Engine. (Dr.Ing. Thesis)
MTA-96-113	Eknes, Monika L., MK	Escalation Scenarios Initiated by Gas Explosions on Offshore Installations. (Dr.Ing. Thesis)
MTA-96-114	Erikstad, Stein O., MP	A Decision Support Model for Preliminary Ship Design. (Dr.Ing. Thesis)
MTA-96-115	Pedersen, Egil, MH	A Nautical Study of Towed Marine Seismic Streamer Cable Configurations. (Dr.Ing. Thesis)
MTA-97-116	Moksnes, Paul O., MM	Modelling Two-Phase Thermo-Fluid Systems Using Bond Graphs. (Dr.Ing. Thesis)
MTA-97-117	Halse, Karl H., MK	On Vortex Shedding and Prediction of Vortex-Induced Vibrations of Circular Cylinders. (Dr.Ing. Thesis)
MTA-97-118	Igland, Ragnar T., MK	Reliability Analysis of Pipelines during Laying, considering Ultimate Strength under Combined Loads. (Dr.Ing. Thesis)
MTA-97-119	Pedersen, Hans-P., MP	Levendefiskteknologi for fiskefartøy. (Dr.Ing. Thesis)
MTA-98-120	Vikestad, Kyrre, MK	Multi-Frequency Response of a Cylinder Subjected to Vortex Shedding and Support Motions. (Dr.Ing. Thesis)
MTA-98-121	Azadi, Mohammad R. E., MK	Analysis of Static and Dynamic Pile-Soil-Jacket Behaviour. (Dr.Ing. Thesis)
MTA-98-122	Ulltang, Terje, MP	A Communication Model for Product Information. (Dr.Ing. Thesis)
MTA-98-123	Torbergsen, Erik, MM	Impeller/Diffuser Interaction Forces in Centrifugal Pumps. (Dr.Ing. Thesis)
MTA-98-124	Hansen, Edmond, MH	A Discrete Element Model to Study Marginal Ice Zone Dynamics and the Behaviour of Vessels Moored in Broken Ice. (Dr.Ing. Thesis)
MTA-98-125	Videiro, Paulo M., MK	Reliability Based Design of Marine Structures. (Dr.Ing. Thesis)
MTA-99-126	Mainçon, Philippe, MK	Fatigue Reliability of Long Welds Application to Titanium Risers. (Dr.Ing. Thesis)
MTA-99-127	Haugen, Elin M., MH	Hydroelastic Analysis of Slamming on Stiffened Plates with Application to Catamaran Wetdecks. (Dr.Ing. Thesis)
MTA-99-128	Langhelle, Nina K., MK	Experimental Validation and Calibration of Nonlinear Finite Element Models for Use in Design of Aluminium Structures Exposed to Fire. (Dr.Ing.

		Thesis)
MTA-99-129	Berstad, Are J., MK	Calculation of Fatigue Damage in Ship Structures. (Dr.Ing. Thesis)
MTA-99-130	Andersen, Trond M., MM	Short Term Maintenance Planning. (Dr.Ing. Thesis)
MTA-99-131	Tveiten, Bård Wathne, MK	Fatigue Assessment of Welded Aluminium Ship Details. (Dr.Ing. Thesis)
MTA-99-132	Søreide, Fredrik, MP	Applications of underwater technology in deep water archaeology. Principles and practice. (Dr.Ing. Thesis)
MTA-99-133	Tønnessen, Rune, MH	A Finite Element Method Applied to Unsteady Viscous Flow Around 2D Blunt Bodies With Sharp Corners. (Dr.Ing. Thesis)
MTA-99-134	Elvekrok, Dag R., MP	Engineering Integration in Field Development Projects in the Norwegian Oil and Gas Industry. The Supplier Management of Norne. (Dr.Ing. Thesis)
MTA-99-135	Fagerholt, Kjetil, MP	Optimeringsbaserte Metoder for Ruteplanlegging innen skipsfart. (Dr.Ing. Thesis)
MTA-99-136	Bysveen, Marie, MM	Visualization in Two Directions on a Dynamic Combustion Rig for Studies of Fuel Quality. (Dr.Ing. Thesis)
MTA-2000-137	Storteig, Eskild, MM	Dynamic characteristics and leakage performance of liquid annular seals in centrifugal pumps. (Dr.Ing. Thesis)
MTA-2000-138	Sagli, Gro, MK	Model uncertainty and simplified estimates of long term extremes of hull girder loads in ships. (Dr.Ing. Thesis)
MTA-2000-139	Tronstad, Harald, MK	Nonlinear analysis and design of cable net structures like fishing gear based on the finite element method. (Dr.Ing. Thesis)
MTA-2000-140	Kroneberg, André, MP	Innovation in shipping by using scenarios. (Dr.Ing. Thesis)
MTA-2000-141	Haslum, Herbjørn Alf, MH	Simplified methods applied to nonlinear motion of spar platforms. (Dr.Ing. Thesis)
MTA-2001-142	Samdal, Ole Johan, MM	Modelling of Degradation Mechanisms and Stressor Interaction on Static Mechanical Equipment Residual Lifetime. (Dr.Ing. Thesis)
MTA-2001-143	Baarholm, Rolf Jarle, MH	Theoretical and experimental studies of wave impact underneath decks of offshore platforms. (Dr.Ing. Thesis)
MTA-2001-144	Wang, Lihua, MK	Probabilistic Analysis of Nonlinear Wave-induced Loads on Ships. (Dr.Ing. Thesis)
MTA-2001-145	Kristensen, Odd H. Holt, MK	Ultimate Capacity of Aluminium Plates under Multiple Loads, Considering HAZ Properties.

		(Dr.Ing. Thesis)
MTA-2001-146	Greco, Marilena, MH	A Two-Dimensional Study of Green-Water Loading. (Dr.Ing. Thesis)
MTA-2001-147	Heggelund, Svein E., MK	Calculation of Global Design Loads and Load Effects in Large High Speed Catamarans. (Dr.Ing. Thesis)
MTA-2001-148	Babalola, Olusegun T., MK	Fatigue Strength of Titanium Risers – Defect Sensitivity. (Dr.Ing. Thesis)
MTA-2001-149	Mohammed, Abuu K., MK	Nonlinear Shell Finite Elements for Ultimate Strength and Collapse Analysis of Ship Structures. (Dr.Ing. Thesis)
MTA-2002-150	Holmedal, Lars E., MH	Wave-current interactions in the vicinity of the sea bed. (Dr.Ing. Thesis)
MTA-2002-151	Rognebakke, Olav F., MH	Sloshing in rectangular tanks and interaction with ship motions. (Dr.Ing. Thesis)
MTA-2002-152	Lader, Pål Furset, MH	Geometry and Kinematics of Breaking Waves. (Dr.Ing. Thesis)
MTA-2002-153	Yang, Qinzheng, MH	Wash and wave resistance of ships in finite water depth. (Dr.Ing. Thesis)
MTA-2002-154	Melhus, Øyvin, MM	Utilization of VOC in Diesel Engines. Ignition and combustion of VOC released by crude oil tankers. (Dr.Ing. Thesis)
MTA-2002-155	Ronæss, Marit, MH	Wave Induced Motions of Two Ships Advancing on Parallel Course. (Dr.Ing. Thesis)
MTA-2002-156	Økland, Ole D., MK	Numerical and experimental investigation of whipping in twin hull vessels exposed to severe wet deck slamming. (Dr.Ing. Thesis)
MTA-2002-157	Ge, Chunhua, MK	Global Hydroelastic Response of Catamarans due to Wet Deck Slamming. (Dr.Ing. Thesis)
MTA-2002-158	Byklum, Eirik, MK	Nonlinear Shell Finite Elements for Ultimate Strength and Collapse Analysis of Ship Structures. (Dr.Ing. Thesis)
IMT-2003-1	Chen, Haibo, MK	Probabilistic Evaluation of FPSO-Tanker Collision in Tandem Offloading Operation. (Dr.Ing. Thesis)
IMT-2003-2	Skaugset, Kjetil Bjørn, MK	On the Suppression of Vortex Induced Vibrations of Circular Cylinders by Radial Water Jets. (Dr.Ing. Thesis)
IMT-2003-3	Chezhian, Muthu	Three-Dimensional Analysis of Slamming. (Dr.Ing. Thesis)
IMT-2003-4	Buhaug, Øyvind	Deposit Formation on Cylinder Liner Surfaces in Medium Speed Engines. (Dr.Ing. Thesis)
IMT-2003-5	Tregde, Vidar	Aspects of Ship Design: Optimization of Aft Hull with Inverse Geometry Design. (Dr.Ing. Thesis)

IMT-2003-6	Wist, Hanne Therese	Statistical Properties of Successive Ocean Wave Parameters. (Dr.Ing. Thesis)
IMT-2004-7	Ransau, Samuel	Numerical Methods for Flows with Evolving Interfaces. (Dr.Ing. Thesis)
IMT-2004-8	Soma, Torkel	Blue-Chip or Sub-Standard. A data interrogation approach of identity safety characteristics of shipping organization. (Dr.Ing. Thesis)
IMT-2004-9	Ersdal, Svein	An experimental study of hydrodynamic forces on cylinders and cables in near axial flow. (Dr.Ing. Thesis)
IMT-2005-10	Brodtkorb, Per Andreas	The Probability of Occurrence of Dangerous Wave Situations at Sea. (Dr.Ing. Thesis)
IMT-2005-11	Yttervik, Rune	Ocean current variability in relation to offshore engineering. (Dr.Ing. Thesis)
IMT-2005-12	Fredheim, Arne	Current Forces on Net-Structures. (Dr.Ing. Thesis)
IMT-2005-13	Heggernes, Kjetil	Flow around marine structures. (Dr.Ing. Thesis
IMT-2005-14	Fouques, Sebastien	Lagrangian Modelling of Ocean Surface Waves and Synthetic Aperture Radar Wave Measurements. (Dr.Ing. Thesis)
IMT-2006-15	Holm, Håvard	Numerical calculation of viscous free surface flow around marine structures. (Dr.Ing. Thesis)
IMT-2006-16	Bjørheim, Lars G.	Failure Assessment of Long Through Thickness Fatigue Cracks in Ship Hulls. (Dr.Ing. Thesis)
IMT-2006-17	Hansson, Lisbeth	Safety Management for Prevention of Occupational Accidents. (Dr.Ing. Thesis)
IMT-2006-18	Zhu, Xinying	Application of the CIP Method to Strongly Nonlinear Wave-Body Interaction Problems. (Dr.Ing. Thesis)
IMT-2006-19	Reite, Karl Johan	Modelling and Control of Trawl Systems. (Dr.Ing. Thesis)
IMT-2006-20	Smogeli, Øyvind Notland	Control of Marine Propellers. From Normal to Extreme Conditions. (Dr.Ing. Thesis)
IMT-2007-21	Storhaug, Gaute	Experimental Investigation of Wave Induced Vibrations and Their Effect on the Fatigue Loading of Ships. (Dr.Ing. Thesis)
IMT-2007-22	Sun, Hui	A Boundary Element Method Applied to Strongly Nonlinear Wave-Body Interaction Problems. (PhD Thesis, CeSOS)
IMT-2007-23	Rustad, Anne Marthine	Modelling and Control of Top Tensioned Risers. (PhD Thesis, CeSOS)
IMT-2007-24	Johansen, Vegar	Modelling flexible slender system for real-time

		simulations and control applications
IMT-2007-25	Wroldsen, Anders Sunde	Modelling and control of tensegrity structures. (PhD Thesis, CeSOS)
IMT-2007-26	Aronsen, Kristoffer Høye	An experimental investigation of in-line and combined inline and cross flow vortex induced vibrations. (Dr. avhandling, IMT)
IMT-2007-27	Gao, Zhen	Stochastic Response Analysis of Mooring Systems with Emphasis on Frequency-domain Analysis of Fatigue due to Wide-band Response Processes (PhD Thesis, CeSOS)
IMT-2007-28	Thorstensen, Tom Anders	Lifetime Profit Modelling of Ageing Systems Utilizing Information about Technical Condition. (Dr.ing. thesis, IMT)
IMT-2008-29	Refsnes, Jon Erling Gorset	Nonlinear Model-Based Control of Slender Body AUVs (PhD Thesis, IMT)
IMT-2008-30	Berntsen, Per Ivar B.	Structural Reliability Based Position Mooring. (PhD-Thesis, IMT)
IMT-2008-31	Ye, Naiquan	Fatigue Assessment of Aluminium Welded Box-stiffener Joints in Ships (Dr.ing. thesis, IMT)
IMT-2008-32	Radan, Damir	Integrated Control of Marine Electrical Power Systems. (PhD-Thesis, IMT)
IMT-2008-33	Thomassen, Paul	Methods for Dynamic Response Analysis and Fatigue Life Estimation of Floating Fish Cages. (Dr.ing. thesis, IMT)
IMT-2008-34	Pákozdi, Csaba	A Smoothed Particle Hydrodynamics Study of Two-dimensional Nonlinear Sloshing in Rectangular Tanks. (Dr.ing.thesis, IMT/ CeSOS)
IMT-2007-35	Grytøyr, Guttorm	A Higher-Order Boundary Element Method and Applications to Marine Hydrodynamics. (Dr.ing.thesis, IMT)
IMT-2008-36	Drummen, Ingo	Experimental and Numerical Investigation of Nonlinear Wave-Induced Load Effects in Containerships considering Hydroelasticity. (PhD thesis, CeSOS)
IMT-2008-37	Skejic, Renato	Maneuvering and Seakeeping of a Singel Ship and of Two Ships in Interaction. (PhD-Thesis, CeSOS)
IMT-2008-38	Harlem, Alf	An Age-Based Replacement Model for Repairable Systems with Attention to High-Speed Marine Diesel Engines. (PhD-Thesis, IMT)
IMT-2008-39	Alsos, Hagbart S.	Ship Grounding. Analysis of Ductile Fracture, Bottom Damage and Hull Girder Response. (PhD-thesis, IMT)
IMT-2008-40	Graczyk, Mateusz	Experimental Investigation of Sloshing Loading and Load Effects in Membrane LNG Tanks Subjected to Random Excitation. (PhD-thesis, CeSOS)

IMT-2008-41	Taghipour, Reza	Efficient Prediction of Dynamic Response for Flexible amd Multi-body Marine Structures. (PhD-thesis, CeSOS)
IMT-2008-42	Ruth, Eivind	Propulsion control and thrust allocation on marine vessels. (PhD thesis, CeSOS)
IMT-2008-43	Nystad, Bent Helge	Technical Condition Indexes and Remaining Useful Life of Aggregated Systems. PhD thesis, IMT
IMT-2008-44	Soni, Prashant Kumar	Hydrodynamic Coefficients for Vortex Induced Vibrations of Flexible Beams, PhD thesis, CeSOS
IMT-2009-45	Amlashi, Hadi K.K.	Ultimate Strength and Reliability-based Design of Ship Hulls with Emphasis on Combined Global and Local Loads. PhD Thesis, IMT
IMT-2009-46	Pedersen, Tom Arne	Bond Graph Modelling of Marine Power Systems. PhD Thesis, IMT
IMT-2009-47	Kristiansen, Trygve	Two-Dimensional Numerical and Experimental Studies of Piston-Mode Resonance. PhD-Thesis, CeSOS
IMT-2009-48	Ong, Muk Chen	Applications of a Standard High Reynolds Number Model and a Stochastic Scour Prediction Model for Marine Structures. PhD-thesis, IMT
IMT-2009-49	Hong, Lin	Simplified Analysis and Design of Ships subjected to Collision and Grounding. PhD-thesis, IMT
IMT-2009-50	Koushan, Kamran	Vortex Induced Vibrations of Free Span Pipelines, PhD thesis, IMT
IMT-2009-51	Korsvik, Jarl Eirik	Heuristic Methods for Ship Routing and Scheduling. PhD-thesis, IMT
IMT-2009-52	Lee, Jihoon	Experimental Investigation and Numerical in Analyzing the Ocean Current Displacement of Longlines. Ph.d.-Thesis, IMT.
IMT-2009-53	Vestbøstad, Tone Gran	A Numerical Study of Wave-in-Deck Impact usin a Two-Dimensional Constrained Interpolation Profile Method, Ph.d.thesis, CeSOS.
IMT-2009-54	Bruun, Kristine	Bond Graph Modelling of Fuel Cells for Marine Power Plants. Ph.d.-thesis, IMT
IMT 2009-55	Holstad, Anders	Numerical Investigation of Turbulence in a Sekwed Three-Dimensional Channel Flow, Ph.d.-thesis, IMT.
IMT 2009-56	Ayala-Uraga, Efren	Reliability-Based Assessment of Deteriorating Ship-shaped Offshore Structures, Ph.d.-thesis, IMT
IMT 2009-57	Kong, Xiangjun	A Numerical Study of a Damaged Ship in Beam Sea Waves. Ph.d.-thesis, IMT/CeSOS.
IMT 2010-58	Kristiansen, David	Wave Induced Effects on Floaters of Aquaculture Plants, Ph.d.-thesis, CeSOS.

IMT 2010-59	Ludvigsen, Martin	An ROV-Toolbox for Optical and Acoustic Scientific Seabed Investigation. Ph.d.-thesis IMT.
IMT 2010-60	Hals, Jørgen	Modelling and Phase Control of Wave-Energy Converters. Ph.d.thesis, CeSOS.
IMT 2010- 61	Shu, Zhi	Uncertainty Assessment of Wave Loads and Ultimate Strength of Tankers and Bulk Carriers in a Reliability Framework. Ph.d. Thesis, IMT/ CeSOS
IMT 2010-62	Shao, Yanlin	Numerical Potential-Flow Studies on Weakly-Nonlinear Wave-Body Interactions with/without Small Forward Speed, Ph.d.thesis,CeSOS.
IMT 2010-63	Califano, Andrea	Dynamic Loads on Marine Propellers due to Intermittent Ventilation. Ph.d.thesis, IMT.
IMT 2010-64	El Khoury, George	Numerical Simulations of Massively Separated Turbulent Flows, Ph.d.-thesis, IMT
IMT 2010-65	Seim, Knut Sponheim	Mixing Process in Dense Overflows with Emphasis on the Faroe Bank Channel Overflow. Ph.d.thesis, IMT
IMT 2010-66	Jia, Huirong	Structural Analysis of Intect and Damaged Ships in a Collission Risk Analysis Perspective. Ph.d.thesis CeSoS.
IMT 2010-67	Jiao, Linlin	Wave-Induced Effects on a Pontoon-type Very Large Floating Structures (VLFS). Ph.D.-thesis, CeSOS.
IMT 2010-68	Abrahamsen, Bjørn Christian	Sloshing Induced Tank Roof with Entrapped Air Pocket. Ph.d.thesis, CeSOS.
IMT 2011-69	Karimirad, Madjid	Stochastic Dynamic Response Analysis of Spar-Type Wind Turbines with Catenary or Taut Mooring Systems. Ph.d.-thesis, CeSOS.
IMT - 2011-70	Erlend Meland	Condition Monitoring of Safety Critical Valves. Ph.d.-thesis, IMT.
IMT – 2011-71	Yang, Limin	Stochastic Dynamic System Analysis of Wave Energy Converter with Hydraulic Power Take-Off, with Particular Reference to Wear Damage Analysis, Ph.d. Thesis, CeSOS.
IMT – 2011-72	Visscher, Jan	Application of Particla Image Velocimetry on Turbulent Marine Flows, Ph.d.Thesis, IMT.
IMT – 2011-73	Su, Biao	Numerical Predictions of Global and Local Ice Loads on Ships. Ph.d.Thesis, CeSOS.
IMT – 2011-74	Liu, Zhenhui	Analytical and Numerical Analysis of Iceberg Collision with Ship Structures. Ph.d.Thesis, IMT.
IMT – 2011-75	Aarsæther, Karl Gunnar	Modeling and Analysis of Ship Traffic by Observation and Numerical Simulation. Ph.d.Thesis, IMT.
Imt – 2011-76	Wu, Jie	Hydrodynamic Force Identification from Stochastic Vortex Induced Vibration Experiments with

		Slender Beams. Ph.d.Thesis, IMT.
Imt – 2011-77	Amini, Hamid	Azimuth Propulsors in Off-design Conditions. Ph.d.Thesis, IMT.
IMT – 2011-78	Nguyen, Tan-Hoi	Toward a System of Real-Time Prediction and Monitoring of Bottom Damage Conditions During Ship Grounding. Ph.d.thesis, IMT.
IMT- 2011-79	Tavakoli, Mohammad T.	Assessment of Oil Spill in Ship Collision and Grounding, Ph.d.thesis, IMT.
IMT- 2011-80	Guo, Bingjie	Numerical and Experimental Investigation of Added Resistance in Waves. Ph.d.Thesis, IMT.
IMT- 2011-81	Chen, Qiaofeng	Ultimate Strength of Aluminium Panels, considering HAZ Effects, IMT
IMT- 2012-82	Kota, Ravikiran S.	Wave Loads on Decks of Offshore Structures in Random Seas, CeSOS.
IMT- 2012-83	Sten, Ronny	Dynamic Simulation of Deep Water Drilling Risers with Heave Compensating System, IMT.
IMT- 2012-84	Berle, Øyvind	Risk and resilience in global maritime supply chains, IMT.
IMT- 2012-85	Fang, Shaoji	Fault Tolerant Position Mooring Control Based on Structural Reliability, CeSOS.
IMT- 2012-86	You, Jikun	Numerical studies on wave forces and moored ship motions in intermediate and shallow water, CeSOS.
IMT- 2012-87	Xiang ,Xu	Maneuvering of two interacting ships in waves, CeSOS
IMT- 2012-88	Dong, Wenbin	Time-domain fatigue response and reliability analysis of offshore wind turbines with emphasis on welded tubular joints and gear components, CeSOS
IMT- 2012-89	Zhu, Suji	Investigation of Wave-Induced Nonlinear Load Effects in Open Ships considering Hull Girder Vibrations in Bending and Torsion, CeSOS
IMT- 2012-90	Zhou, Li	Numerical and Experimental Investigation of Station-keeping in Level Ice, CeSOS
IMT- 2012-91	Ushakov, Sergey	Particulate matter emission characteristics from diesel enignes operating on conventional and alternative marine fuels, IMT
IMT- 2013-1	Yin, Decao	Experimental and Numerical Analysis of Combined In-line and Cross-flow Vortex Induced Vibrations, CeSOS
IMT- 2013-2	Kurniawan, Adi	Modelling and geometry optimisation of wave energy converters, CeSOS

IMT-2013-3	Al Ryati, Nabil	Technical condition indexes doe auxiliary marine diesel engines, IMT
IMT-2013-4	Firoozkoohi, Reza	Experimental, numerical and analytical investigation of the effect of screens on sloshing, CeSOS
IMT-2013-5	Ommani, Babak	Potential-Flow Predictions of a Semi-Displacement Vessel Including Applications to Calm Water Broaching, CeSOS
IMT-2013-6	Xing, Yihan	Modelling and analysis of the gearbox in a floating spar-type wind turbine, CeSOS
IMT-7-2013	Balland, Océane	Optimization models for reducing air emissions from ships, IMT
IMT-8-2013	Yang, Dan	Transitional wake flow behind an inclined flat plate-----Computation and analysis, IMT
IMT-9-2013	Abdillah, Suyuthi	Prediction of Extreme Loads and Fatigue Damage for a Ship Hull due to Ice Action, IMT
IMT-10-2013	Ramìrez, Pedro Agustìn Pèrez	Ageing management and life extension of technical systems- Concepts and methods applied to oil and gas facilities, IMT
IMT-11-2013	Chuang, Zhenju	Experimental and Numerical Investigation of Speed Loss due to Seakeeping and Maneuvering. IMT
IMT-12-2013	Etemaddar, Mahmoud	Load and Response Analysis of Wind Turbines under Atmospheric Icing and Controller System Faults with Emphasis on Spar Type Floating Wind Turbines, IMT
IMT-13-2013	Lindstad, Haakon	Strategies and measures for reducing maritime CO2 emissons, IMT
IMT-14-2013	Haris, Sabril	Damage interaction analysis of ship collisions, IMT
IMT-15-2013	Shainee, Mohamed	Conceptual Design, Numerical and Experimental Investigation of a SPM Cage Concept for Offshore Mariculture, IMT
IMT-16-2013	Gansel, Lars	Flow past porous cylinders and effects of biofouling and fish behavior on the flow in and around Atlantic salmon net cages, IMT
IMT-17-2013	Gaspar, Henrique	Handling Aspects of Complexity in Conceptual Ship Design, IMT
IMT-18-2013	Thys, Maxime	Theoretical and Experimental Investigation of a Free Running Fishing Vessel at Small Frequency of Encounter, CeSOS
IMT-19-2013	Aglen, Ida	VIV in Free Spanning Pipelines, CeSOS
IMT-1-2014	Song, An	Theoretical and experimental studies of wave diffraction and radiation loads on a horizontally submerged perforated plate, CeSOS

IMT-2-2014	Rogne, Øyvind Ygre	Numerical and Experimental Investigation of a Hinged 5-body Wave Energy Converter, CeSOS
IMT-3-2014	Dai, Lijuan	Safe and efficient operation and maintenance of offshore wind farms ,IMT
IMT-4-2014	Bachynski, Erin Elizabeth	Design and Dynamic Analysis of Tension Leg Platform Wind Turbines, CeSOS
IMT-5-2014	Wang, Jingbo	Water Entry of Freefall Wedged – Wedge motions and Cavity Dynamics, CeSOS
IMT-6-2014	Kim, Ekaterina	Experimental and numerical studies related to the coupled behavior of ice mass and steel structures during accidental collisions, IMT
IMT-7-2014	Tan, Xiang	Numerical investigation of ship's continuous- mode icebreaking in leverl ice, CeSOS
IMT-8-2014	Muliawan, Made Jaya	Design and Analysis of Combined Floating Wave and Wind Power Facilities, with Emphasis on Extreme Load Effects of the Mooring System, CeSOS
IMT-9-2014	Jiang, Zhiyu	Long-term response analysis of wind turbines with an emphasis on fault and shutdown conditions, IMT
IMT-10-2014	Dukan, Fredrik	ROV Motion Control Systems, IMT
IMT-11-2014	Grimsmo, Nils I.	Dynamic simulations of hydraulic cylinder for heave compensation of deep water drilling risers, IMT
IMT-12-2014	Kvittem, Marit I.	Modelling and response analysis for fatigue design of a semisubmersible wind turbine, CeSOS
IMT-13-2014	Akhtar, Juned	The Effects of Human Fatigue on Risk at Sea, IMT
IMT-14-2014	Syahroni, Nur	Fatigue Assessment of Welded Joints Taking into Account Effects of Residual Stress, IMT
IMT-1-2015	Bøckmann, Eirik	Wave Propulsion of ships, IMT
IMT-2-2015	Wang, Kai	Modelling and dynamic analysis of a semi-submersible floating vertical axis wind turbine, CeSOS
IMT-3-2015	Fredriksen, Arnt Gunvald	A numerical and experimental study of a two-dimensional body with moonpool in waves and current, CeSOS
IMT-4-2015	Jose Patricio Gallardo Canabes	Numerical studies of viscous flow around bluff bodies, IMT
IMT-5-2015	Vegard Longva	Formulation and application of finite element techniques for slender marine structures subjected to contact interactions, IMT
IMT-6-2015	Jacobus De Vaal	Aerodynamic modelling of floating wind turbines, CeSOS

IMT-7-2015	Fachri Nasution	Fatigue Performance of Copper Power Conductors, IMT
IMT-8-2015	Oleh I Karpa	Development of bivariate extreme value distributions for applications in marine technology,CeSOS
IMT-9-2015	Daniel de Almeida Fernandes	An output feedback motion control system for ROVs, AMOS
IMT-10-2015	Bo Zhao	Particle Filter for Fault Diagnosis: Application to Dynamic Positioning Vessel and Underwater Robotics, CeSOS
IMT-11-2015	Wenting Zhu	Impact of emission allocation in maritime transportation, IMT
IMT-12-2015	Amir Rasekhi Nejad	Dynamic Analysis and Design of Gearboxes in Offshore Wind Turbines in a Structural Reliability Perspective, CeSOS
IMT-13-2015	Arturo Jesùs Ortega Malca	Dynamic Response of Flexibles Risers due to Unsteady Slug Flow, CeSOS
IMT-14-2015	Dagfinn Husjord	Guidance and decision-support system for safe navigation of ships operating in close proximity, IMT
IMT-15-2015	Anirban Bhattacharyya	Ducted Propellers: Behaviour in Waves and Scale Effects, IMT
IMT-16-2015	Qin Zhang	Image Processing for Ice Parameter Identification in Ice Management, IMT
IMT-1-2016	Vincentius Rumawas	Human Factors in Ship Design and Operation: An Experiential Learning, IMT
IMT-2-2016	Martin Storheim	Structural response in ship-platform and ship-ice collisions, IMT
IMT-3-2016	Mia Abrahamsen Prsic	Numerical Simulations of the Flow around single and Tandem Circular Cylinders Close to a Plane Wall, IMT
IMT-4-2016	Tufan Arslan	Large-eddy simulations of cross-flow around ship sections, IMT
IMT-5-2016	Pierre Yves-Henry	Parametrisation of aquatic vegetation in hydraulic and coastal research,IMT
IMT-6-2016	Lin Li	Dynamic Analysis of the Instalation of Monopiles for Offshore Wind Turbines, CeSOS
IMT-7-2016	Øivind Kåre Kjerstad	Dynamic Positioning of Marine Vessels in Ice, IMT

IMT-8-2016	Xiaopeng Wu	Numerical Analysis of Anchor Handling and Fish Trawling Operations in a Safety Perspective, CeSOS
IMT-9-2016	Zhengshun Cheng	Integrated Dynamic Analysis of Floating Vertical Axis Wind Turbines, CeSOS
IMT-10-2016	Ling Wan	Experimental and Numerical Study of a Combined Offshore Wind and Wave Energy Converter Concept
IMT-11-2016	Wei Chai	Stochastic dynamic analysis and reliability evaluation of the roll motion for ships in random seas, CeSOS
IMT-12-2016	Øyvind Selnes Patricksson	Decision support for conceptual ship design with focus on a changing life cycle and future uncertainty, IMT
IMT-13-2016	Mats Jørgen Thorsen	Time domain analysis of vortex-induced vibrations, IMT
IMT-14-2016	Edgar McGuinness	Safety in the Norwegian Fishing Fleet – Analysis and measures for improvement, IMT
IMT-15-2016	Sepideh Jafarzadeh	Energy effiency and emission abatement in the fishing fleet, IMT
IMT-16-2016	Wilson Ivan Guachamin Acero	Assessment of marine operations for offshore wind turbine installation with emphasis on response-based operational limits, IMT
IMT-17-2016	Mauro Candeloro	Tools and Methods for Autonomous Operations on Seabed and Water Coumn using Underwater Vehicles, IMT
IMT-18-2016	Valentin Chabaud	Real-Time Hybrid Model Testing of Floating Wind Tubines, IMT
IMT-1-2017	Mohammad Saud Afzal	Three-dimensional streaming in a sea bed boundary layer
IMT-2-2017	Peng Li	A Theoretical and Experimental Study of Wave-induced Hydroelastic Response of a Circular Floating Collar
IMT-3-2017	Martin Bergström	A simulation-based design method for arctic maritime transport systems
IMT-4-2017	Bhushan Taskar	The effect of waves on marine propellers and propulsion
IMT-5-2017	Mohsen Bardestani	A two-dimensional numerical and experimental study of a floater with net and sinker tube in waves and current
IMT-6-2017	Fatemeh Hoseini Dadmarzi	Direct Numerical Simualtion of turbulent wakes behind different plate configurations

IMT-7-2017	Michel R. Miyazaki	Modeling and control of hybrid marine power plants
IMT-8-2017	Giri Rajasekhar Gunnu	Safety and effiency enhancement of anchor handling operations with particular emphasis on the stability of anchor handling vessels
IMT-9-2017	Kevin Koosup Yum	Transient Performance and Emissions of a Turbocharged Diesel Engine for Marine Power Plants
IMT-10-2017	Zhaolong Yu	Hydrodynamic and structural aspects of ship collisions
IMT-11-2017	Martin Hassel	Risk Analysis and Modelling of Allisions between Passing Vessels and Offshore Installations
IMT-12-2017	Astrid H. Brodtkorb	Hybrid Control of Marine Vessels – Dynamic Positioning in Varying Conditions
IMT-13-2017	Kjersti Bruserud	Simultaneous stochastic model of waves and current for prediction of structural design loads
IMT-14-2017	Finn-Idar Grøtta Giske	Long-Term Extreme Response Analysis of Marine Structures Using Inverse Reliability Methods
IMT-15-2017	Stian Skjong	Modeling and Simulation of Maritime Systems and Operations for Virtual Prototyping using co-Simulations
IMT-1-2018	Yingguang Chu	Virtual Prototyping for Marine Crane Design and Operations
IMT-2-2018	Sergey Gavrilin	Validation of ship manoeuvring simulation models
IMT-3-2018	Jeevith Hegde	Tools and methods to manage risk in autonomous subsea inspection,maintenance and repair operations
IMT-4-2018	Ida M. Strand	Sea Loads on Closed Flexible Fish Cages
IMT-5-2018	Erlend Kvinge Jørgensen	Navigation and Control of Underwater Robotic Vehicles
IMT-6-2018	Bård Stovner	Aided Intertial Navigation of Underwater Vehicles